Topological Spin Structures in Ferrimagnetic Thin Film Alloys

Boris Seng

UNIVERSITÉ DE LORRAINE

Ecole Doctorale C2PM
Laboratoire IJL

JOHANNES GUTENBERG UNIVERSITÄT

Thèse

Présentée et soutenue publiquement pour l'obtention du titre de

DOCTEUR DE l'UNIVERSITE DE LORRAINE

Mention : PHYSIQUE

par **Boris SENG**

Sous la direction de STÉPHANE MANGIN et MATHIAS KLÄUI

Structures Topologiques de Spin dans des Couches Minces d'Alliages Ferrimagnétiques

8 décembre 2022

Membres du jury :

Directeurs de thèse :	**M. Stéphane MANGIN**	**Professeur des universités, IJL, Nancy, France**
	M. Mathias KLÄUI	**Professeur des universités, JGU, Mainz, Deutschland**
Président de jury :	**M. Michel HEHN**	**Professeur des universités, IJL, Nancy, France**
Rapporteurs :	**M. Jeffrey MCCORD**	**Professeur des universités, CAU, Kiel, Deutschland**
	Mme Liza HERRERA DIEZ	**Docteur, C2N, Paris, France**
Examinateurs :	**M. Dafiné RAVÉLOSONA**	**Professeur des universités, C2N, Paris, France**
	M. Martin JOURDAN	**Professeur des universités, JGU, Mainz, Deutschland**

Chiral spin structures in ferrimagnetic alloys

Thesis submitted for the degree of

Doctor of Natural Sciences in Physics

of the Johannes Gutenberg University and the University of Lorraine

on 8^{th} December 2022

Boris Seng

President of the jury:	Prof. Dr. Michel Hehn	IJL, France
Rapporteurs:	Prof. Dr. Jeffrey McCord	CAU, Deutschland
	Dr. Liza Herrera Diez	C2N, France
Examiners:	Dr. Dafiné Ravélosona	C2N, France
	Prof. Dr. Martin Jourdan	JGU Mainz, Deutschland
Supervisors:	Prof. Dr. Mathias Kläui	JGU Mainz, Deutschland
	Prof. Dr. Stéphane Mangin	IJL, France

I assure you that I have written this doctoral thesis myself.

Albertville, the 12^{th} October 2022

Boris Seng
sengboris@gmail.com

Institut für Physik
Johannes Gutenberg-Universität Mainz
Staudingerweg 7
55128 Mainz (Deutschland)
bseng@uni-mainz.de

Institut Jean Lamour
Université de Lorraine
2, allée André Guinier
54011 Nancy (France)
boris.seng@univ-lorraine.fr

À ma mère

Acknowledgments

I would like to acknowledge and give my warmest thanks to my supervisors Mathias Kläui and Stéphane Mangin who made this work possible. Their guidance as well as their empathy helped me to go through all the stages of this thesis. I would also like to thank Michel Hehn for the support he provided me. His tenacity gave me confidence to work hardly for this thesis. Clearly, you three made this thesis went to the end.

I would like to thank very much my committee members for letting my defense be an astonishing good time for me. Also, I thank you for your comments and suggestions to make the manuscript better.

For helping me during this thesis, thank you to all my colleagues from Mainz and Nancy. A special thanks to Daniel Schönke, my SEMPA expert, a very nice person that I really enjoyed having time with. Also, thank you to the skyrmion team that helped me to understand as much as possible the complexity of the study, especially Nico Kerber, Fabian Kammerbauer, Takaaki Dohi and Klaus Raab for all the discussions we had. Thank you to Daniel Lacour that helped a lot to post-process the data we got particularly in beamtime. I would also like to thank Jun-Young Kim, Kyujoon Lee and Robert Reeve, the postdocs that helped me daily in Mainz. Finally, a sincere thanks to the beamtime team for all the time spent in Berlin and Villigen. Something that I will almost miss.

More personnally, I would like to thank my friends, thank you all, in particular François Béchet, Adélaïde Dreux, Anthony Auzerais, Anne-Lise Marty, Fanny Anfrye, David Barillet, Loic Pidou, Julie Gatinet and Léa Chaumeil. All of you were present from the beginning till the end, as always. Thank you also to the friends met during this particular time and especially Koko, Jean-Loïs, Quentin, Anna, Maryam and Maxime.

Also, I would like to thank Tiziana Schöfer for supporting me all these years. No words could really express my sincere thanks and how indebted I am feeling with you. I will never forget what she did.

Thank you to all my family for their support. Especially, I would like to thank my mother more than everyone. This thesis could also be considered as yours.

Finally, I would like to thank Aurore Anfrye for her love and her presence with all my

heart. Times spent with her were always beautiful moments that helped me to think about other things that this manuscript. Thank you also to her children, Lily and Shaun.

Abstract

In these times of ecological concerns, the impact of our lifestyles on our environment is essential to analyze. Since energy consumption is the main source of greenhouse gas emissions in the world, it is necessary to look for other ways to reduce our consumption.
One of the major sources of energy consumption is data storage, with storage increasing significantly each year. A new technological solution has been proposed allowing the storage of these data at a lower energy cost and in a more efficient way by using magnetic skyrmions instead of magnetic domains. A magnetic skyrmion is a quasi-particle of size that can goes down to few atoms while a magnetic domain is of the order of a micrometer. Therefore, it is possible to imagine a data storage system based on the absence or the presence of this quasi-particle, representing the "0" or the "1" of a data bit. Thus, this thesis will focus on the nucleation and manipulation of magnetic skyrmions.
These quasi-particles have been stabilized in various materials at room temperature, a condition for the use by all. The ability to nucleate, annihilate, and even move them using electric currents has also been shown. Nevertheless, the displacement of these magnetic structures generates several problems. Firstly, these structures seem to be particularly affected by structural defects in matter, the so-called "pinning". Indeed, magnetic skyrmions are so small that they can be trapped or even destroyed when passing through a defect in the material from which they come. Secondly, it appeared that the skyrmions did not move in linearly with the applied current but possess a perpendicular component causing them to deviate from the path of the electrons, an effect known as the "skyrmion Hall angle". This can be a problem as they may encounter the wall of a lithographed structure causing the non-homogeneity of the dynamics and implying a possible loss of the stored information. The use of a ferrimagnetic material has been proposed to solve partially these problems. Theoretically, it is possible to annihilate this "skyrmion Hall angle" in a ferrimagnetic material having a very weak magnetization at a very precise temperature. Thus, the experiments carried out in this thesis aim to nucleate magnetic skyrmions in ferrimagnetic materials while studying their dynamics.
In this thesis, the nucleation of spin structures in ferrimagnetic materials based on GdFeCo has been reported. The structures were mapped using a "SEMPA" microscope where the in-plane magnetic configuration was revealed indicating the chiral character of the quasi-particles. The precise measurement of the domain walls, domain that separates two opposite magnetic domains in direction, also made it possible to deduct the value of the exchange constant, an important parameter in the physics of condensed matter but difficult to measure. Finally, the dynamics of magnetic

skyrmions using current has been studied in CoDy ferrimagnetic materials. This dynamics has been determined to be deterministic showing a homochiral character of the spin textures. Furthermore, the skyrmion speed as a function of the injected current density at different temperatures has also been studied.

Zusammenfassung

In diesen Zeiten von ökologischen Bedenken, ist es sehr wichtig die Auswirkungen unseres Lebensstils auf unsere Umwelt zu analysieren. Da Energie verbrauch die Hauptquelle von Treibhausgasemissionen in der Welt ist, ist es notwendig, nach Wegen zu suchen, um unseren Verbrauch zu reduzieren.
Eine der Hauptquellen des Energieverbrauchs ist die Datenspeicherung, wobei die Speicherung jedes Jahr erheblich zunimmt. Es wurde eine neue technologische Lösung vorgeschlagen, die die Speicherung dieser Daten zu niedrigeren Energiekosten und auf effizientere Weise ermöglicht, indem magnetische Skyrmionen anstelle von magnetischen Domänen verwendet werden. Ein magnetisches Skyrmion ist ein magnetisches Quasiteilchen, dessen Größe auf wenige Atome reduziert werden kann, während eine magnetische Domäne häufig in der Größenordnung von einem Mikrometer liegt. Es ist daher möglich, sich ein Informationsspeichersystem vorzustellen, das auf dem Fehlen oder Vorhandensein dieses Quasiteilchens basiert, das die Werte "0" oder die "1" eines Datenbits darstellt. Daher konzentriert sich diese Arbeit auf die Nukleation und Manipulation magnetischer Skyrmionen.
Diese Quasi-Partikel wurden kürzlich in verschiedenen Materialien bei Raumtemperatur stabilisiert, eine unabdingbare Voraussetzung für die Verwendung durch alle. Die Fähigkeit, sie mit Hilfe von elektrischem Strom zu nukleieren, zu vernichten und sogar zu bewegen, wurde ebenfalls gezeigt. Trotzdem wirft die Verschiebung dieser magnetischen Strukturen zum heutigen Zeitpunkt ein Problem auf. Erstens scheinen diese Strukturen besonders von strukturellen Defekten in der Materie, dem sogenannten "Pinning", betroffen zu sein. Tatsächlich sind magnetische Skyrmionen so klein, dass sie eingefangen oder sogar zerstört werden können, wenn sie einen Defekt in dem Material passieren, aus dem sie stammen. Zweitens schien es, dass sich die Skyrmionen nicht linear mit dem angelegten Strom bewegten, sondern eine senkrechte Komponente aufwiesen, die dazu führte, dass sie vom Weg der Elektronen abweichen, ein Effekt, der als "Skyrmion-Hall-Winkel" bekannt ist. Dies kann ein Problem sein, da sie auf die Wand einer lithographierten Struktur treffen können, was zu einer Inhomogenität der Dynamik und einem möglichen Verlust der gespeicherten Informationen führen kann. Um diese Probleme zumindest teilweise zu beheben, wurde die Verwendung eines ferrimagnetischen Materials vorgeschlagen. Theoretisch ist es möglich, diesen "Skyrmion-Hall-Winkel" in einem ferrimagnetischen Material mit einer sehr schwachen Magnetisierung bei einer sehr genauen Temperatur zu unterdrücken. Daher zielen die in dieser Dissertation durchgeführten Experimente darauf ab, magnetische Skyrmionen in ferrimagnetischen Materialien zu nukleieren und gleichzeitig ihre Dynamik zu untersuchen.
In dieser Arbeit wurde über die Keimbildung von Spinstrukturen in ferrimagnetis-

chen Materialien auf Basis von GdFeCo berichtet. Die Strukturen wurden unter Verwendung eines "SEMPA"-Mikroskops abgebildet, wobei die magnetische Konfiguration in der Ebene aufgedeckt wurde, was den chiralen Charakter der Quasiteilchen anzeigt. Die genaue Messung der Domänenwände, die zwei entgegengesetzte magnetische Domänen in Richtung trennen, ermöglichte auch die Ableitung des Wertes der Austauschkonstante, ein wichtiger Parameter in der Physik der kondensierten Materie, aber schwer zu messen. Schließlich wurde die Dynamik magnetischer Skyrmionen durch elektrischen Strom in ferrimagnetischen Legierungen auf CoDy-Basis untersucht. Diese Dynamik erwies sich als deterministisch, was den homochiralen Charakter dieser Spinstrukturen unterstreicht. Darüber hinaus erstreckte sich diese Studie auf die Geschwindigkeit dieser Skyrmionen als Funktion der bei verschiedenen Temperaturen injizierten Stromdichte.

Résumé

En ces temps de préoccupations écologiques, l'impact de nos modes de vie sur notre environnement est essentiel à analyser. L'énergie étant la principale source d'émissions de gaz à effet de serre dans le monde, il est nécessaire de chercher des moyens pour réduire notre consommation.
Une des sources importantes de consommation d'énergie est le stockage des données, stockage augmentant chaque année de manière significative. Il a été proposé une nouvelle solution technologique permettant le stockage de ces données à moindre coût énergétique et de manières plus efficace en utilisant des skyrmions magnétiques en lieu et place des domaines magnétiques. Un skyrmion magnétique est une quasi-particule magnétique de taille pouvant être réduite à quelques atomes alors qu'un domaine magnétique est de l'ordre du micromètre. Il est donc possible d'imaginer un système de stockage de l'information reposant sur l'absence ou la présence de cette quasi-particule, représentant le "0" ou le "1" d'un bit de donnée. Ainsi, cette thèse se focalisera sur la nucléation et la manipulation de skyrmions magnétiques.
Ces quasi-particules ont récemment été stabilisé dans divers matériaux à température ambiante, condition sine qua non à une utilisation par tous. Il a également été montré la possibilité de les nucléer, de les annihiler et même de les déplacer à l'aide de courants électriques. Néanmoins, le déplacement de ces structures magnétiques, à l'heure d'aujourd'hui, pose problème. Premièrement, ces structures semblent être particulièrement affectées par les défauts structurels de la matière, ce qu'on appelle le "pinning". En effet, les skyrmions magnétiques sont si petits qu'ils peuvent être piégés voir détruits au passage d'un défaut dans le matériau d'où ils proviennent. Deuxièmement, il est apparu que les skyrmions ne se déplaçaient pas de manières linéaires avec le courant appliqué mais possédaient une composante perpendiculaire les faisant dévier du chemin des électrons, effet connu sous le nom de "skyrmion Hall angle". Ceci peut être un problème dans la mesure où ils peuvent rencontrer la paroi d'une structure lithographiée provoquant la non-homogénéité de la dynamique et impliquer une possible perte de l'information stockée. Pour remédier au moins en partie à ces problèmes, l'utilisation d'un matériau ferrimagnétique a été proposé. Théoriquement, il est possible d'annihiler ce "skyrmion Hall angle" dans un matériau ferrimagnétique possédant une très faible aimantation à une température bien précise. Ainsi, les expériences menées dans cette thèse ont pour but de nucléer des skyrmions magnétiques dans des matériaux ferrimagnétiques tout en étudiant leur dynamique.
Dans cette thèse, la nucléation de structures de spin dans des matériaux ferrimagnétiques à base de GdFeCo a été relaté. Les structures ont été cartographié à l'aide d'un microscope "SEMPA" où la configuration magnétique dans le plan a été révélé, indiquant le caractère chiral des quasi-particules. La mesure précise des parois

de domaines séparant deux domaines magnétiques opposés en direction a également permis de déduire la valeur de la constante d'échange, paramètre important dans la physique de la matière condensée mais souvent difficile à mesurer. Enfin, la dynamique de skyrmions magnétiques par courant électriques a été étudié dans des alliages ferrimagnétiques à base de CoDy. Cette dynamique s'est révélé déterministique mettant ainsi en évidence la caractère homochiral de ces structures de spin. De plus, cette étude s'est étendu sur la vitesse de ces skyrmions en fonction de la densité de courant injecté à différentes température.

Contents

Introduction

To our present knowledge, gravitational, electromagnetic, weak nuclear and strong nuclear are the four fundamental interactions that exist in the universe. The play between them is essential for the life as we know it. It stabilizes the matter at an elementary level, gives rise to the stars and governs the cosmos. Among them, electromagnetism is probably the most famous one, known to every single human being for millennia. A manifestion of this phenomenon is magnetism. An old legend relates that a greek shepherd was suddenly stucked to the ground. He noticed that the iron nails present in his shoes were attracted by a lodestone which is now known as magnetite. From that so-called day, a significant part of the humans in the world have tried to understand this curiosity. Unfortunately to them, this was an impossible task without significant mathematical progresses, an atomic description of the matter and its quantum properties. Four thousands years later with the emergence of quantum mechanics, an exhaustive description of the magnetism have been made possible and the role of the electron and its spin has been made clear. This opened the path of using the spin of the electrons, i.e. an intrinsic angular momentum of the associated particle, in electronic devices that generate new fields of study: nanomagnetism and spintronic.

My PhD work is part of these fields. Nanomagnetism concerns the study of magnetism at the nanometer scale which is close to typical length scale such as exchange length, dmain wall length. In nanomagnetism, research topics conern the nucleation, the detection and the manipulation of nano-objects such as magnetic domains, domain walls and skyrmions using various stimuli such as manetic field, electric field, light or heat. In spin electronic or spintronic, one considers that the electron not only has a mass and a charge but also a spin. Spin dependent electronic transport in heterostructures and the influence of spin polarised current on magnetization are studied.

This thesis is divided into two parts as following:

- Part I. Background
  - Chapter 1: Theory of topological spin structures
  - Chapter 2: Experimental methods
  - Chapter 3: State of the art
- Part II. Experimental results
  - Chapter 4: Direct observation of pure Néel-type spin structures in GdFeCo-based ferrimagnet

- Chapter 5: Current-induced dynamics of magnetic skyrmions in ferrimagnets

Part I focuses on the theory of topological spin structures, gives an overview of the main experimental setup used in this thesis and present the important results that have been obtained in this field of study. In the chapter 1, a description of the different magnetic interactions is presented as well as a precised definition of what we call chiral objects with their different properties. In the chapter 2, the main experimental setup used for this thesis are described. The chapter 3, last chapter of part I, presents the progresses and discoveries that have been made over the last decades in the area of chiral spin structures. This first part gives the necessary background to understand the different studies presented in the experimental results in part II.
Part II focuses on the experimentals results that have been acquired during this thesis. Chapter 4 reports on the direct observation of homochiral spin structures in GdFeCo-based ferrimagnetic material. Finally, chapter 5, it focuses on the current-driven dynamics of magnetic skyrmions in CoDy-based ferrimagnetic material, results that have been obtained using synchrotron facilities.

Part I.

Background

1. Theory of chiral spin structures

Magnetism is a broad and complicated area of research. Therefore, this chapter will only focus on some key points that are relevant to understand the complexity of chiral spin structures. First of all, we will briefly introduce the origin of magnetism and describe the differents energy terms that arise in magnetic materials. Especially, the Dzyaloshinskii-Moriya interaction (DMI), source of chirality, will be discussed. Afterwards, we will discuss on the chiral character of magnetic objects and their interesting properties.

1.1. Origin of the magnetism

Manifestions of magnetism can be visible at the macroscopic scale such as the interaction between two magnets. However, its origin is purely a quantum effect due to the presence and the displacement of fermions. In the case of magnetic materials, the particle responsible for magnetism is the electron in a solid. An electron is an elementary particle where its state is fully described by a set of quantum numbers: n, l, m_l and m_s that obey Hund's rules. It possesses two angular momenta: the orbital angular momentum $\boldsymbol{L}$ represented by the azimuthal quantum number l where its projection along a specified axis is defined by the magnetic quantum number m_l and the intrinsic spin angular momentum $\boldsymbol{S}$ where its projection along a specified axis is defined by the spin quantum number m_s.

- Orbital angular momentum

The displacement of electric charges, i.e an electric current, creates a magnetic flux density $\boldsymbol{B}$ that was well describes in the works of Biot and Savart in the beginning of the 19^{th} century. Therefore, electrons can be considered as magnets due to their displacement in magnetic materials. To caracterize this magnet, we introduce the notion of magnetic moment that represents the strength and the orientation of the magnet. The relation between the orbital angular momentum $\boldsymbol{L}$ and the orbital magnetic moment $\boldsymbol{\mu}_L$ is given by:

$$\boldsymbol{\mu}_L = -g_l \frac{e}{2m_e} \boldsymbol{L} \tag{1.1}$$

$$= -g_l \frac{\mu_B}{\hbar} \boldsymbol{L} \tag{1.2}$$

where $g_l = 1$ is the Landé g-factor, e is the elementary charge, m_e the electron mass, $\hbar$ the reduced Planck constant and $\mu_B = \frac{e\hbar}{2m_e}$ the Bohr magneton. We can express the

magnitude of the orbital angular momentum $|\boldsymbol{L}|$ and its component along the arbitrary z-direction L_z as a function of quantum numbers through the following relations:

$$|\boldsymbol{L}| = \sqrt{l(l+1)}\hbar \tag{1.3}$$

$$L_z = m_l\hbar \tag{1.4}$$

As a first consequence, s-subshell electrons where $l = 0$ possess no orbital angular momentum which explains their spherical symmetry. Furthermore, atoms with half- or full-filled subshell will also have no orbital angular momentum ($l_{tot} = 0$) following Hund's rules.

- Spin angular momentum

The spin angular momentum $\boldsymbol{S}$ is an intrinsic property of elementary particles. Analogously to orbital angular momentum, this property gives rise to a magnetic moment of electrons, the spin magnetic moment $\boldsymbol{\mu}_S$, such as:

$$\boldsymbol{\mu}_S = -g_e\frac{e}{2m_e}\boldsymbol{S} \tag{1.5}$$

$$= -g_e\frac{\mu_B}{\hbar}\boldsymbol{S} \tag{1.6}$$

where $g_e \approx 2.0023$ is the g-factor of the electron. We can express the magnitude of the spin angular momentum $|\boldsymbol{S}|$ and its component along the arbitrary z-direction S_z as a function of quantum numbers through the following relations:

$$|\boldsymbol{S}| = \sqrt{s(s+1)}\hbar \tag{1.7}$$

$$S_z = m_s\hbar \tag{1.8}$$

Therefore, atoms with full-filled subshell will have no spin angular momentum ($s_{tot} = 0$) following Hund's rules.

As a consequence, only unfully filled subshells will play a role in the magnetic properties of an atom and therefore only valence electrons are taking into account where their total magnetic moment $\boldsymbol{\mu}$ is then:

$$\boldsymbol{\mu} = \boldsymbol{\mu}_L + \boldsymbol{\mu}_S \tag{1.9}$$

$$= -\frac{\mu_B}{\hbar}(g_l\boldsymbol{L} + g_e\boldsymbol{S}) \tag{1.10}$$

To describe the notion of magnetic moments in magnetic materials, it is interesting to take into account the spatial distribution of the magnetic moments. Therefore, the magnetization $\boldsymbol{M}$ is here introduced which represents the density of magnetic moments $\boldsymbol{\mu}$ in a magnetic material such as:

$$\boldsymbol{\mu} = \iiint dV\boldsymbol{M} \tag{1.11}$$

1.2. Energy terms in magnetic thin films

There are several interactions that act on a magnetic moment. In the following sections, we will describe the most important ones. For a reasonable comprehension of the phenomenon, it is always important to understand the reasons behind it. Therefore, a detailed but non-exhaustive description of each interaction is proposed.

1.2.1. Heisenberg exchange interaction

The exchange interaction is a pure quantum effect with no classical counterpart. In the case of fermions, the Pauli exclusion principle states that no commutable fermions can have the exact same quantum state which as for consequence of an antisymmetric wave function of the system.
As a first step, we will start with the two-electron model. The wave function ψ of the system consists in the product of the spatial ψ_{spat} and spin ψ_{spin} wave functions. Following the Pauli exclusion principle, one of this function has to be symmetric while the other should be antisymmetric in order to keep an antisymmetric product such as:

$$\psi_{S,T} = \begin{cases} \psi_{spat;S}(\boldsymbol{r}_1, \boldsymbol{r}_2)\psi_{spin;A}(\boldsymbol{\sigma}_1, \boldsymbol{\sigma}_2) \\ \psi_{spat;A}(\boldsymbol{r}_1, \boldsymbol{r}_2)\psi_{spin;S}(\boldsymbol{\sigma}_1, \boldsymbol{\sigma}_2) \end{cases} \tag{1.12}$$

where $\psi_{S,T}$ represent the singlet and triplet states. The two electrons are in states that can be represented by single-electron spatial ($\phi_1(\boldsymbol{r})$, $\phi_2(\boldsymbol{r})$) and spin ($\chi_1(\boldsymbol{\sigma})$, $\chi_2(\boldsymbol{\sigma})$) wavefunctions whose represent their initial wave functions without considering any mutual interaction.
Here, we firstly consider the normalized symmetric and antisymmetric spatial wave functions of the two-electrons model:

$$\psi_{spat;S,A}(\boldsymbol{r}_1, \boldsymbol{r}_2) = \frac{1}{\sqrt{2}}(\phi_a(\boldsymbol{r}_1)\phi_b(\boldsymbol{r}_2) \pm \phi_a(\boldsymbol{r}_2)\phi_b(\boldsymbol{r}_1)) \tag{1.13}$$

where $\psi_{spat;S}$ and $\psi_{spat;A}$ are the spatial parts of the wave function of the system representing the spin singlet (S=0 with the two spins antiparallel to each other) and spin triplet (S=1 with the two spins parallel to each other) states. The normalized symmetric and antisymmetric spin wave functions can be written as:

$$\psi_{spin;A} = \frac{1}{\sqrt{2}}(\chi_1(\boldsymbol{\sigma}_1)\chi_2(\boldsymbol{\sigma}_2) - \chi_1(\boldsymbol{\sigma}_2)\chi_2(\boldsymbol{\sigma}_1)) \tag{1.14}$$

$$\psi_{spin;S} = \begin{cases} \chi_1(\boldsymbol{\sigma}_1)\chi_2(\boldsymbol{\sigma}_1) \\ \frac{1}{\sqrt{2}}(\chi_1(\boldsymbol{\sigma}_1)\chi_2(\boldsymbol{\sigma}_2) + \chi_1(\boldsymbol{\sigma}_2)\chi_2(\boldsymbol{\sigma}_1)) \\ \chi_1(\boldsymbol{\sigma}_2)\chi_2(\boldsymbol{\sigma}_2) \end{cases} \tag{1.15}$$

where the singlet and triplet states are now obvious.
The respective energy of the singlet and triplet is:

$$E_S = \int d^3\boldsymbol{r}_1 \int d^3\boldsymbol{r}_2 \; \psi_S^* \hat{H} \psi_S \tag{1.16}$$

$$E_T = \int d^3\boldsymbol{r}_1 \int d^3\boldsymbol{r}_2 \; \psi_T^* \hat{H} \psi_T \tag{1.17}$$

where $\hat{H} = \sum_{i<j} \frac{e^2}{|\boldsymbol{r}_1 - \boldsymbol{r}_2|}$ is the Hamiltonian of the Coulomb potential, i.e. the electron-electron potential interacting between charged particles.
One can define the exchange constant (or exchange integral) J_{ab} that defines the strength of the interaction between two neighboring charged particles. This exchange constant is defined following the following relation:

$$J_{ab} = \frac{E_s - E_T}{2} = \int d^3\boldsymbol{r}_1 \int d^3\boldsymbol{r}_2 \; \phi_a^*(\boldsymbol{r}_1)\phi_b^*(\boldsymbol{r}_2)\frac{e^2}{|\boldsymbol{r}_1 - \boldsymbol{r}_2|}\phi_a(\boldsymbol{r}_2)\phi_b(\boldsymbol{r}_1) \tag{1.18}$$

When $J_{ab} > 0$, E_T is then favored which means an alignment of the two spins, this is called a ferromagnetic state. Respectively, when $J_{ab} < 0$, E_S is favored which leads to an antialignment of the two spins, this is called an antiferromagnetic state. Dirac showed that the difference between the singlet and triplet state can be parametrized with $\boldsymbol{S}_a.\boldsymbol{S}_b$ and an effective Hamiltonian of the exchange interaction in a spinor basis of the two-electron model can be written as:

$$\hat{H} = -2J_{ab}\boldsymbol{S}_a.\boldsymbol{S}_b \tag{1.19}$$

By generalizing the Hamiltonian in equation 1.19 to a n-spins model, the energy of the exchange interaction is defined as :

$$E_{exch} = -J_{ab}\sum_{i<j} \boldsymbol{S}_i.\boldsymbol{S}_j \tag{1.20}$$

considering the sum of adjacents spins only.
Generally, one uses another quantity to define the strength of the exchange interaction related to the exchange integral J_{ab} in order to take into account the crystal structure, the so-called exchange stiffness constant A. For a simple cubic lattice with a lattice parameter a, the exchange stiffness A_{sc} is such as:

$$A_{sc} = \frac{J_{ex}\langle S^2 \rangle}{a} \tag{1.21}$$

1.2.2. Zeeman interaction

When a magnetic field is present, it couples with the matter in two different ways through the minimal coupling and the spin. Let us first condider the first case. The minimal coupling involves only the charge distribution. The momentum is modified according to $\boldsymbol{p} \rightarrow \boldsymbol{p} - q\boldsymbol{A}$ where the vector potential $\boldsymbol{A}$ is given by: $\boldsymbol{B} = \boldsymbol{\nabla} \times \boldsymbol{A}$. In an uniform magnetic induction $\boldsymbol{B} = B\boldsymbol{u}_z$, the vector potential is chosen as: $\boldsymbol{A} =$

$\frac{1}{2}\boldsymbol{B} \wedge \boldsymbol{r} = \frac{B}{2}(-y\boldsymbol{u}_x + x\boldsymbol{u}_y)$. This leads to a change in the kinetic energy Hamiltonian of an electron such as:

$$\hat{H} = \frac{(\boldsymbol{p} - q\boldsymbol{A})^2}{2m_e} \tag{1.22}$$

$$= \frac{(\boldsymbol{p}^2 - 2q\boldsymbol{p}.\boldsymbol{A} + q^2\boldsymbol{A}^2)}{2m_e} \tag{1.23}$$

$$= \frac{\boldsymbol{p}^2}{2m_e} + \frac{e}{2m_e}(\boldsymbol{r} \wedge \boldsymbol{p}).\boldsymbol{B} + \frac{e^2B^2}{8m_e}(x^2 + y^2) \tag{1.24}$$

$$= \frac{\boldsymbol{p}^2}{2m_e} - \boldsymbol{\mu}_L.\boldsymbol{B} + \frac{e^2B^2}{8m_e}(x^2 + y^2) \tag{1.25}$$

Analogously to the orbital magnetic moment $\boldsymbol{\mu}_L$, the magnetic induction $\boldsymbol{B}$ couples with the spin magnetic moment such as $-\boldsymbol{\mu}_s.\boldsymbol{B}$. Therefore, the modified Hamiltonian due to the presence of the magnetic field is:

$$\hat{H} = \frac{\boldsymbol{p}^2}{2m_e} - \boldsymbol{\mu}.\boldsymbol{B} + \frac{e^2B^2}{8m_e}(x^2 + y^2) \tag{1.26}$$

$$= \hat{T} + \hat{H}_{Zee} + \hat{H}_{dia} \tag{1.27}$$

where $\hat{T}$ represents the kinetic energy of a free particle, $\hat{H}_{Zee}$ the Zeeman effect which can be seen as the paramagnetism and $\hat{H}_{dia}$ the diamagnetism. The latter one induced a magnetic moment antiparallel to the applied field since $\boldsymbol{m} = -\frac{\partial \boldsymbol{H}}{\partial B} = -\frac{e^2}{4m_e}B(x^2 + y^2)\boldsymbol{u}_z$. Concerning the Zeeman term, a magnetic moment $\boldsymbol{\mu}$ located in an external magnetic field $\boldsymbol{H}_{ext}$ will tend to align with it. The energy representing this interaction is:

$$E_{Zee} = -\mu_0\ \boldsymbol{\mu}.\boldsymbol{H}_{ext} \tag{1.28}$$

In the case of magnetized materials of local magnetization $\boldsymbol{M}$, the Zeeman energy is defined as:

$$E_{Zee} = \mu_0 \iiint dV\, \boldsymbol{M}.\boldsymbol{H}_{ext} \tag{1.29}$$

A sufficient magnetic field strength will force the magnetic moments to align with it. Therefore, in the case of non-uniform stable spin textures, the magnetic field favours the part of the spin textures where $\boldsymbol{M}$ is aligned with $\boldsymbol{H}_{ext}$ which lead to a size control of the different magnetic configurations depending on the strength of the magnetic field.

1.2.3. Magnetic anisotropy energy

Anisotropy is a fundamental property of magnetic materials. The magnetic anisotropy energy (MAE) represents the energy of a system which directly depends on the direction of the magnetization. Although this energy is rather small, in the order of few

µeV/atom, it is probably the most important one since it will favor a direction of the magnetization which could be either in-plane (IP) or out-of-plane compared to the sample plane or else a combination of both. They are two distincts origins of MAE: the dipolar interaction and the spin-orbit coupling.

- The dipolar interaction

In the section 1.2.2, we described how a magnetic material behaves in the presence of a magnetic field. However, we did not include the magnetic field created by the material itself: the stray field $\boldsymbol{H}_{stray}$. It represents the field arising from all the magnetic moments around a local position. This stray field is defined as:

$$\boldsymbol{H}_{stray} = -\frac{1}{4\pi}\boldsymbol{\nabla}\left[\iiint_V d^3\boldsymbol{r'}\frac{-\boldsymbol{\nabla}\boldsymbol{M}(\boldsymbol{r'})}{|\boldsymbol{r}-\boldsymbol{r'}|} + \iint_S d^2\boldsymbol{r'}\frac{\boldsymbol{M}(\boldsymbol{r'})\boldsymbol{n}(\boldsymbol{r'})}{|\boldsymbol{r}-\boldsymbol{r'}|}\right] \tag{1.30}$$

where $\boldsymbol{n}(\boldsymbol{r'})$ being the normal vector at the surface at the coordinates $\boldsymbol{r'}$. The first term in the equation 1.30 represent the stray field arising from the magnetic charges within the volume while the second one represent the magnetic charges on its surface. In the case of ultrathin films with uniform magnetized material, the energy corresponding from the presence of the stray field is:

$$E_{stray}(\boldsymbol{r}) = -\frac{\mu_0}{2}\int dV\,\boldsymbol{M}.\boldsymbol{H}_{stray} \tag{1.31}$$

The dipolar interaction is a long-range interaction. This is the source of shape anisotropy which senses the outer shape of the sample.

- The spin-orbit coupling

The electron spatial distribution and its movement creates a magnetic flux density $\boldsymbol{B}$ that was well described in section 1.1. This magnetic induction arising from an electron interacts with its own spin, this is called the spin-orbit-coupling (SOC) and is defined as the interaction between the spin of a particle and its movement in a potential. This leads to the Hamitonian $\hat{H}_{SOC}$ of the spin-orbit coupling:

$$\hat{H}_{SOC} = -\frac{e}{2m_e^2c^2}\left(\frac{1}{r}\frac{dV}{dr}\right)\boldsymbol{L}_j.\boldsymbol{S}_i \tag{1.32}$$

Therefore, the environment of the electron has an effect on the electron wave function which is especially true in crystallographic ordered materials. This finally changes the distribution of the particle density that can cause a more favorable energy state in a specific direction, i.e. an easy axis of the magnetization direction contrary to a hard axis for the most unfavorable energy state. This type of anisotropy is called magnetocrystalline anisotropy and can have several denominations such as uniaxial anisotropy, cubic anisotropy or tetragonal anisotropy depending on the symmetry of the studied crystal. Here, we will focused on the uniaxial anisotroy describing a low symmetry system where an easy axis is present. The energy of this anisotropy is equal to:

$$E_{uni} = K_1 sin^2(\theta) + K_2 sin^4(\theta) \tag{1.33}$$

where higher terms have been neglected. K_1 is often represented as as the uniaxial anisotropy K_u. The angle θ is defined between the easy axis and the direction of the magnetization.

1.2.4. Dzyaloshinskii-Moriya interaction

The Dzyaloshinskii-Moriya interaction (DMI) is an antisymmetric exchange interaction that arises between two neighboring spins $\boldsymbol{S_i}$ and $\boldsymbol{S_j}$ mediated by an adjacent atom. This indirect exchange interaction is only possible in systems with a broken inversion symmetry where the adjacent atom will interact with the two spins separately through the SOC. Therefore, this effect is especially seen in the presence of large SOC materials such as heavy metals (HM). The Hamiltonian of this interaction can be defined as:

$$\hat{H}_{DMI} = -\boldsymbol{D_{ij}}.(\boldsymbol{S_i} \times \boldsymbol{S_j}) \tag{1.34}$$

where $\boldsymbol{D_{ij}}$ is the DMI vector reflecting the strength of the interaction where the mimimum of energy is reached when the two adjacent spins are orthogonals.
The classification of DMI is generally divided into two classes: the bulk DMI and the interfactial DMI where the latter one will be more extended due to its importance for our work.

- Bulk DMI

The bulk DMI arises in low symmetry crystals where a broken inversion symmetry is present. This type of crystals such as those belonging to the B20 group has been used to experimentally observed the DMI for the first time. Generally, the position of the atom responsible for the strong SOC effect is between two ferromagnetic atoms which causes the DMI vector to be directed from one ferromagnetic atom to the other one (see image 1.1). Also, a "bulk" DMI is present in anisotropic composition alloys such as GdFeCo ferrimagnetic alloy that we are studying in this manuscript [1]. This interaction, rather low compared to interfacial DMI, is supposed to come from the non-homogeneity of the alloy stoichiometry accross the thickness.

- Interfacial DMI

As its name suggests it, the interfacial DMI arises at the interface between two materials. Since this interaction comes from a SOC effect, this interaction is especially present at the interface between a heavy metal and a ferromagnetic material (HM/FM) due to the strength of the SOC presents in HM materials [2] [3]. Contrary to the bulk DMI, the direction of the DMI vector is here perpendicular to the line connecting the two FM atoms (see image 1.1) due to the position of the HM atoms

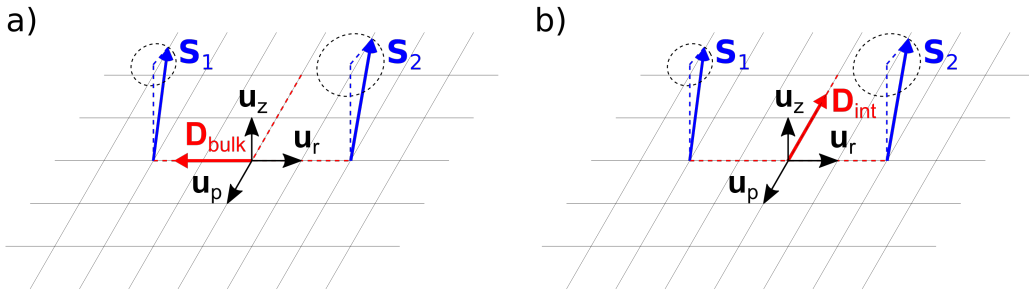

Figure 1.1.: Sketch of a two-spin model (blue) for (a) bulk and (b) interfacial DMI with corresponding DMI vectors (red). (Adapted from [4])

compared to the FM ones.

The DMI favors a rotation of the spins such as $\leftarrow\uparrow\rightarrow$ or $\leftarrow\downarrow\rightarrow$ in the tangential (Bloch) or radial (Néel) plane depending on the classification and the sign of the DMI. The DMI strength can be estimated theoretically or measured experimentally through different methods such as Brilloin light scattering (BLS) or asymmetric bubble expansion (ABE). In figure 1.2, a summary is present of the most common value of the DMI between 3d (TM) and 5d electrons (HM) that have been calculated using relativistic first-principles calculations [5].

1.2.5. Effect of the energy terms

In figure 1.3, we illustrate the effect of the main energy terms on the spins or the magnetic moments by showing a lowest energy configuration. In figure 1.3.a, the exchange constant A has been chosen positive leading to a ferromagnetic state where the spins (black arrows) are lying in the plane arbitrary. In figure 1.3.b, the magnetic moments are following the magnetic flux density $\boldsymbol{B}$. In figure 1.3.c, we illustrate an uniaxial in-plane anisotropy (double-arrow) where the spins are arbitrary choosing one of the two directions of the axis. From an energy point of view and only by considering the magnetic anisotropy energy, the two directions are equivalent following equation 1.33. Finally, the stray field energy present in figure 1.3.d is showing a formation of domains, especially a closure of domains in order to reduce the stray field energy (dipolar interaction).

1.3. Chirality

By taking into account all the energies described in section 1.2, the formation of stable or metastable non-collinear spin textures is possible by minimizing the sum of te energy. As an example, while we have seen in section 1.2.1 that the Heisenberg exchange

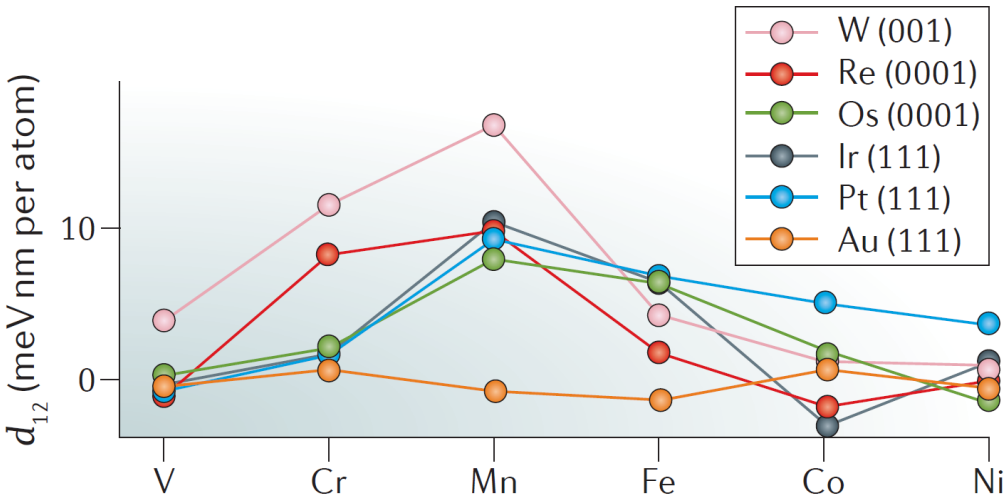

Figure 1.2.: Strength and sign of the Dzyaloshinskii-Moriya interaction D_{tot} in 3d TM monolayers on 5d substrates calculated around their magnetic ground state combining the relativistic SOC effect with spin spirals. A positive sign of D^{tot} indicates a left-rotational sense or "left chirality". (Extracted from [5])

interaction favors two neighboring spins to align together, the DMI favors their perpendicular alignment. This interaction is generally at least two orders of magntitude smaller than the Heisenberg exchange one and therefore can not counterbalance the alignment between neighboring spins. However, this can slighly tilt aligned neighboring spins in order to form domain walls (DW), i.e. the regions separating two magnetic domains with opposite direction of the magnetization. In this section, we will describe the stabilization of topological spin textures as well as their DW.

1.3.1. Domain walls and domain wall width

It exists different types of DW depending on how the magnetization varies inside them. In this work, we only studied out-of-plane (OOP) magnetic systems and therefore will especially discuss this case. The two extreme cases that exist are the Bloch- and Néel-type DW. These can be stabilized by different type of interactions where the play between them can also lead to an intermediate state. It is frequently admitted that the DW profile (along the x direction) in OOP systems (with z direction along the anisotropy axis) is such that:

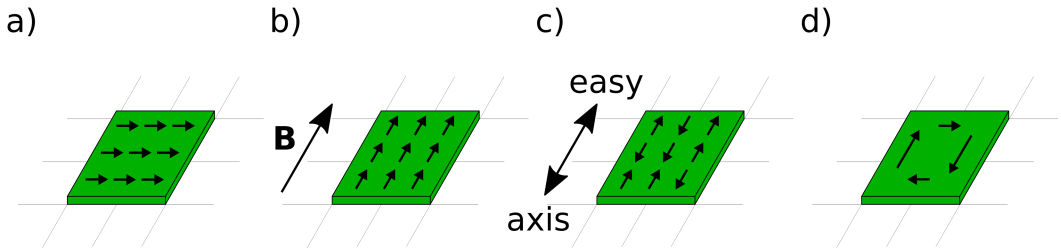

Figure 1.3.: Sketch of the magnetic configurations favored by the following energy terms: (a) the exchange Heisenberg energy, (b) the Zeeman energy, (c) the uniaxial anisotropy energy and (d) the stray field energy.

$$m_x(x) = sin(\psi)cosh^{-1}(\frac{x}{\Delta}) \tag{1.35}$$

$$m_y(x) = cos(\psi)cosh^{-1}(\frac{x}{\Delta}) \tag{1.36}$$

$$m_z(x) = tanh(\frac{x}{\Delta}) \tag{1.37}$$

where $\mathbf{m} = (m_x, m_y, m_z)$ is the normalized magnetization vector, Δ the Bloch parameter and ψ the DW angle defined between the DW tangente and the direction of the magnetization in the xy-plane. The value of ψ defined the type of DW where $|sin(\psi)| = 0$ leads to Bloch-type DW while $|cos(\psi)| = 0$ conducts to Néel-type DW where the different cases are display in figure 1.4.
The DW forms a continious transition between two opposite magnetic domains and therefore it exists several formulas for the DW width depending on the definition used [7]. Thus, one has to be careful before comparing different values of the DW width. In our case, we used lilley's definition based on the slope of the DW angle ψ where the DW width δ is related to the Bloch parameter Δ such as [8]:

$$\delta = \pi\Delta \tag{1.38}$$

I. Lemesh *et al.* showed by analytical considerations that an isolated DW with a Bloch parameter Δ in the limit of small and large thicknesses d of the magnetic materials is equal to [9]:

$$\lim_{d\to 0} \Delta = \Delta_0 - \frac{\mu_0 M_s^2}{4\pi K_{eff}} d \tag{1.39}$$

$$\lim_{d\to +\infty} \Delta = \Delta_\infty = \sqrt{\frac{A}{K_u + \frac{\mu_0 M_s^2}{2} sin^2(\psi)}} \tag{1.40}$$

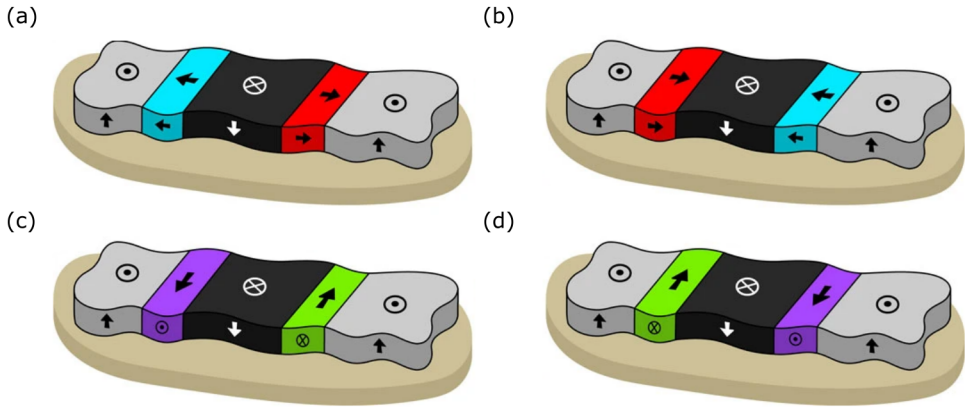

Figure 1.4.: Schematic chiral domains with (a) Néel-type counterclockwise and (b) clockwise DW and (c) Bloch-type clockwise and (d) counterclockwise DW extrated from [6].

where $K_{eff} = K_u - \frac{\mu_0 M_s^2}{2}$ and $\Delta_0 = \sqrt{\frac{A}{K_{eff}}}$ with A being the exchange stiffness of the magnetic material. Since the resulting Bloch parameter Δ is a linear function of the thickness d in the limit of ultrathin magnetic film while independent of this thickness for ultrathick magnetic film, it is then mathematically possible to extrapolate an approximated Bloch parameter Δ in the intermediate thickness range such as [9]:

$$\Delta(d,\psi) = \Delta_0 - \frac{1}{\frac{2\pi(Q-1)}{d} + \frac{1}{\Delta_0 - \Delta_\infty(\psi)}} \tag{1.41}$$

where $Q = \frac{2K_u}{\mu_0 M_s^2}$ is defined as the quality factor. Here, we note that the Bloch parameter $\Delta(d,\psi)$ depends directly on the DMI value through the angle ψ where [9]:

$$sin(\psi) = \begin{cases} -\frac{D}{D_{thr}}, & |D| < D_{thr} \\ -sgn(D), & |D| \geq D_{thr} \end{cases} \tag{1.42}$$

$$D_{thr}(d) = \frac{2\mu_0 M_s^2}{\frac{\pi^2}{d\,ln(2)} + \pi\sqrt{\frac{K_u + \frac{\mu_0 M_s^2}{2}}{A}}} \tag{1.43}$$

where D is the interfacial DMI strength and D_{thr} the threshold value of the interfacial DMI necessary to force DW to be purely Néel. The sign of the DMI is defined by convention where a positive DMI leads to a counterclockwise chirality.

1.3.2. Homochirality

The type of chirality of spin textures (Bloch or Néel) can be favored with different parameters such as the thickness of the magnetic material d or the exchange stiffness A by adjusting the strength of D_{thr} as seen in equation 1.42 and 1.42. However, the defined configuration stabilized by the susmentionned parameters will have no-prefered sens of rotation (clockwise or counterclockwise) since D_{thr} will always be positive. This leads to a material stabilizing chiral spin structures with different helicities conducting to non-homogeneous dynamics behaviors. In order to force the system to stabilize the same type of spin textures, i.e. a homochiral character, the presence of a "chiral" interaction such as the interfacial DMI is necessary. Indeed, the interfacial DMI D leads to a deterministic sens of rotation through the sign of this interaction, positive or negative (see equation 1.42).

1.3.3. Topology

The topology is a branch of mathematics that study the properties of geometric objects under continious deformation. One of the most important notion is the Euler characteristic, topological invariant classifying geometrical objects in different classes where two objects of the same class are homomorphic. On a similar way and in a discrete approximation, one can classify magnetic spin textures through the topological charge Q (also known as the winding number) such as [10] [11]:

$$Q = \frac{1}{4\pi} \iint dx\, dy\ \mathbf{m} \,.\, (\frac{\partial \mathbf{m}}{\partial x} \times \frac{\partial \mathbf{m}}{\partial y}) \tag{1.44}$$

where $\mathbf{m}$ is the normalized magnetization vector. Here, Q defined how many times the normalized magnetisation can be wrapped around the three-dimensional unit sphere.

1.3.4. Topological non-trivial spin textures

- Magnetic skyrmion

Magnetic skyrmions are 2-dimensional circular and local whirling spin textures with a continious pattern along the third dimension possessing a topological charge $Q = \pm 1$ depending on the helicity [10] [12]. These can be constructed by a stereographic projection of a three-dimensional spherical spin textures. From the different types of chiral DW previously discussed in section 1.3.1, it exists two extreme cases for magnetic skyrmions: the Bloch-type and the Néel-type (see figure 1.5) where an intermediate state is also possible as seen in 1.6.b.

- Other spin textures

Beyond magnetic skyrmions, one can imagine unlimited types of non-trivial spin textures. In figure 1.6, B. Göbel *et al.* reviewed the main important ones [12]. Especially, the skyrmionium and the ferrimagnetic skyrmion which can be seen in 1.6.f-g

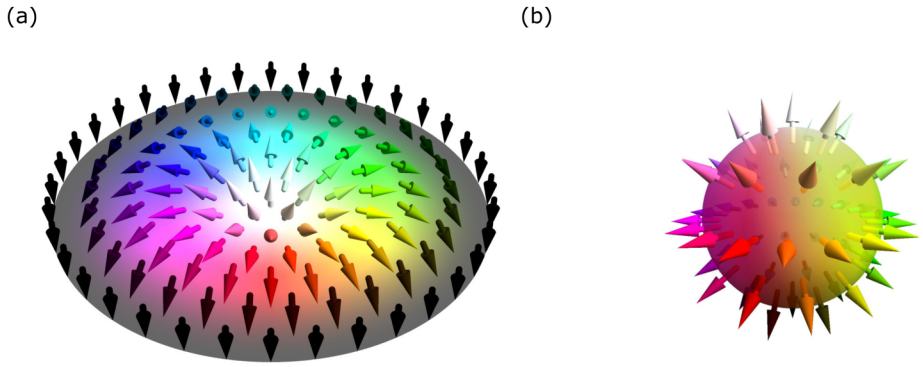

Figure 1.5.: (a) A two-dimensional Néel-type magnetic skyrmion constructed from (b) a three-dimensional hedgehog spin textures (where all moments on the sphere point along the radial direction) by a stereographic projection. Figure adapted from [12].

have been observed during this thesis (see Part II) where their remarkable properties will be detailed in section 1.5. A skyrmionium is formed from a magnetic skyrmion surrounded by another one with the same chirality leading to a topological charge $Q = 1 - 1 = 0$. Concerning the ferrimagnetic skyrmion, it is a superposition of two opposite skyrmions at the same position arising from two opposite magnetic sublattices such as in ferrimagnetic alloys with a topological charge $Q = 0$ (see section 1.5).

- Topological stability

Contrary to the saturated magnetization state possessing a trivial topological charge $Q = 0$, chiral spin textures such as magnetic skyrmions are non-trivial topological charges with $Q \neq 0$. Therefore, by topological considerations, non-trivial spin textures should be perfectly stable in uniaxial anisotropy materials due to their impossibility of being transform continiously into an aligned magnetization state. This is also true for non-trivial spin textures with $Q = 0$. Indeed, this type of spin textures possesses a zero topological charge but their construction arises from topological geometric structures such as a skyrmionium forming from two skyrmions with $Q = 1 - 1 = 0$. However, defects present in materials modify this perfect stability into a metastable state where an energy barrier has to be overcome in order to pass from one state to another. The stability of topological spin textures makes possible the study of their dynamics.

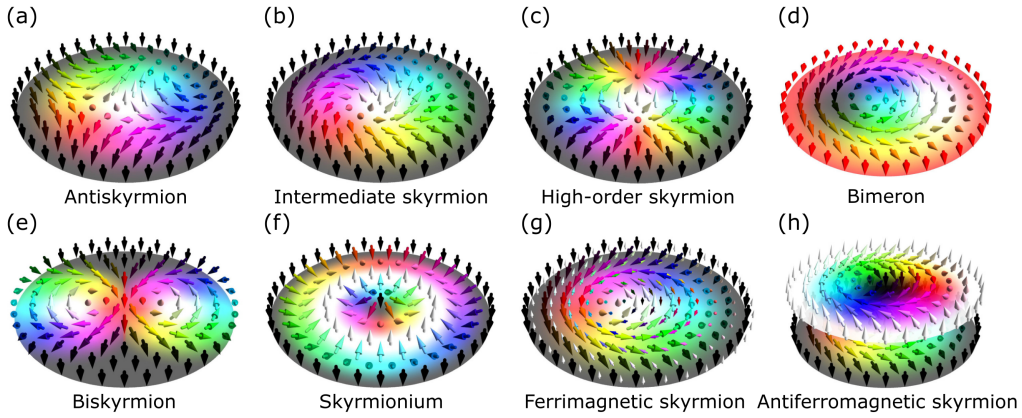

Figure 1.6.: Overview of different types of topologically non-trivial spin textures. The three first schemes are different types of skyrmions such as: (a) an antiskyrmion, (b) a skyrmion with an intermediate DW state between Bloch and Néel where $\psi = \frac{\pi}{4}$ and (c) a higher-order skyrmion with $Q = 2$. (d) shows a magnetic bimeron consisting of two merons. The middle row shows combinations of two skyrmions: (e) the biskyrmion with $Q = 2$, (f) a skyrmionium with $Q = 0$ and (g,h) ferrimagnetic and synthetic antiferromagnetic skyrmions for which the topological charges of the two skyrmions in each sublattice compensate each other. Figure adapted from [12].

1.4. Current-induced dynamics of spin textures

1.4.1. Landau-Lifschitz-Gilbert-Slonczewski equation

To understand the dynamics of spin textures, one has to study how the magnetization $\mathbf{M}$ change in time. This is modeled by the Landay-Lifschitz-Gilbert-Slonczewski equation such as [13] [14] [15]:

$$\frac{d\mathbf{M}}{dt} = \underbrace{-\gamma_0\, \mathbf{M} \times \mathbf{H}_{eff}}_{precession} + \underbrace{\frac{\alpha}{M_s}\, \mathbf{M} \times \frac{d\mathbf{M}}{dt}}_{damping} + \underbrace{\boldsymbol{\tau}}_{additional torques} \tag{1.45}$$

where γ is the gyromamnetic ratio, α the Gilbert damping parameter, $\mathbf{H}_{eff}$ the effective magnetic field and $\boldsymbol{\tau}$ the additional torques exerted on the magnetization $\mathbf{M}$. In the equation 1.45, the first term describes the precession of the magnetic moments due to the different interactions while the second one represents the damping. The last term is representative of the action of the spin currents on the magnetic moments and is described in the following sections 1.4.2 and 1.4.4. The effective magnetic field takes into account all the interactions described in section 1.2 such as:

$$\mathbf{H}_{eff} = -\frac{1}{\mu_0}\frac{\partial \Xi}{\partial \mathbf{M}} \tag{1.46}$$

where Ξ is the local total magnetic energy.

1.4.2. Spin-transfer torque

Due to the unbalanced density of states of conduction electrons in magnetic materials, a current flowing through it will be divided into two channels with one majority and one minority depending on the direction of its spin leading to a spin-polarized current. This spin-polarized current flowing through the magnetic material will reoriente its spin to align with the local magnetization due to the exchange interaction. To respect the conservation of the total angular momentum of the system, the transfer of the spin from the electrons to the material leads to a sizable torque on the magnetization of the magnetic material. The spin-transfer torque (STT) is a possible way of moving the DW [16] since the electrons passing through the DW induce a torque which can drag the DW along the electron flow direction. [17] [18] [19]. The STT possesses two terms, the adiabatic STT and the non-adiabatic STT such as:

$$\boldsymbol{\tau}_{STT} = \underbrace{-\frac{b_j}{\mu_0 M_s^2}\,\mathbf{M}\times[\mathbf{M}\times(\mathbf{j}_e\,.\,\boldsymbol{\nabla})\mathbf{M}]}_{adiabatic} \underbrace{-\frac{c_j}{\mu_0 M_s}\,\mathbf{M}\times(\mathbf{j}_e\,.\,\boldsymbol{\nabla})\mathbf{M}}_{non-adiabatic} \tag{1.47}$$

with the pre-factors $b_j = \frac{P\mu_B}{eM_s(1+\xi^2)}$ and $c_j = \frac{P\mu_B\xi}{eM_s(1+\xi^2)}$, the charge current $\mathbf{j}_e$ and the spin polarization $\mathbf{P}$, $\xi = \frac{\tau_{ex}}{\tau_{sf}} \approx 10^{-2}$ where τ_{ex} is the exchange relaxation time and τ_{sf} the spin-flip relaxation time.

1.4.3. Spin Hall effect

The SOC defined the interaction between a spin with the local potential which is especially strong in HM. This leads to a deflection of the electrical charge depending on the direction of its spin following equation 1.32. Thus, when a current is going through a HM, the electrons are following two opposite and perpendicular paths leading to spin accumulations at the interfaces of the HM, the spin Hall effect (SHE). This conducts to a pure transverse spin current $\mathbf{j}_s$ such that:

$$\mathbf{j}_s = \frac{\hbar}{2e}\,\Theta_{SH}\,\mathbf{j}_c \times \boldsymbol{\sigma} \tag{1.48}$$

where $\mathbf{j}_s$ and $\mathbf{j}_c$ are respectively the spin and charge currents, Θ_{SH} is the spin Hall angle and $\boldsymbol{\sigma}$ the polarization of the spin current. The spin Hall angle defined the efficiency of the conversion of the charge currents to pure spin currents.

1.4.4. Spin-orbit torque

When a HM and FM are juxtaposed, the spin accumulation at the HM/FM interface due to the SHE in the HM material gives rise to a spin torque effect named spin-orbit torque (SOT) [20] [21] [22]. These torques are similar to the STT studied previously and are decomposed into a field-like and a damping-like components given by:

$$\boldsymbol{\tau}_{SOT} = -\underbrace{\gamma_0\, a_j\, \mathbf{M} \times [\mathbf{M} \times (\mathbf{e}_z \times \mathbf{j})]}_{damping-like} - \underbrace{\gamma_0\, b_j\, \mathbf{M} \times (\mathbf{e}_z \times \boldsymbol{j})}_{field-like} \tag{1.49}$$

where SOT pre-factors $a_j = \frac{\hbar \Theta_{SH}}{2eM_s d\mu_0}$ and $b_j = \frac{\hbar \Theta_{SH} \xi}{2eM_s d\mu_0}$. The thickness of the magnetic material d scales down with the torque applied. This implies that the magnetic material thickness can be reduced in order to improve the efficiency of the SOT. Similarly to the STT, SOT can displace DW through the progressive realignment of the DW spin orientation.

1.4.5. Skyrmion Hall effect

Comparable to the Hall effect that describes the transverse motion of charged particles due to local magnetic fields, the skyrmion Hall effect depicts the transverse motion of skyrmions compared to the direction of the applied current via SOT [23] [24] [25]. To quantize the effect, one can use the Thiele formalism to determine the motion of the skyrmion center such as:

$$\mathbf{G} \times \mathbf{v}_d - \alpha \mathbf{D}.\mathbf{v}_d + 4\pi \mathbf{B}.\mathbf{J}_{HM} = 0 \tag{1.50}$$

where $G = C\mathbf{u}_z$ is related to the topological charge C, $\mathbf{v}_d = (v_{dx}, v_{dy})$ is the in-plane drift velocity of the skyrmion center, α represents the Gilbert damping parameter, $\mathbf{D}$ is the dissipative force tensor, $\mathbf{B}$ quantifies the efficiency of the spin Hall spin torque and $\mathbf{J}_{HM}$ is the current in the HM adjacent layers. The transverse motion is represented by the first term in equation 1.51 which is known as the Magnus force comparable to the Lorentz force in classical Hall effect for electrical charges. Therefore, non-trivial spin textures with a 0 topological charge display no transverse motion and should be perfectly parallel with the applied current.

From the Thiele equation, one can extract the angle that forms the motion of the skyrmion center with the applied current, namely the skyrmion Hall angle Θ_{SkH} where:

$$\Theta_{SkH} = tan^{-1}(\frac{-C}{\alpha D}) \tag{1.51}$$

1.5. Ferrimagnetic alloys and ferrimagnetic spin textures properties

In this thesis, alloys composed with transition metal (TM) and heavy rare earth (RE) are used. The magnetism arises from the electrons of the 3d subshell in TM elements and from the electrons of the 5f subshell in heavy RE elements. The magnetic moments of these elements are known to be antiferromagnetic coupled through a cascade of direct and indirect exchange [26] leading to ferrimagnetic materials.

- Magnetization compensation temperature

In TM-RE ferrimagnetic alloys, the overall magnetization is the sum of the two opposite sublattices. Therefore, it is possible to control the total magnetization by tuning the stoichiometry of the alloy. Since the temperature dependence of the magnetization is different for the two sublattices where the heavy RE magnetization increases faster than the TM one at low temperature, one can get ferrimagnetic samples where the dominant sublattice change with temperature passing from heavy RE dominant to TM dominant by increasing the temperature. The magnetization compensation temperature is the temperature where the zero net magnetization is reached due by compensation of the two sublattices.

- Angular momentum compensation temperature

Faster dynamics of spin textures has been demonstrated when the total angular momentum is egual to zero [27]. Due to the different Landé factors of the atoms of the ferrimagnetic materials, the temperature necessary to achieve zero angular momentum is different from the temperature annihilating the total net magnetization but should be closed to.

- Properties of ferrimagnetic spin textures

Ferrimagnetic materials are especially interesting to use for the study of skyrmion dynamics since one can tune easily different parameters such as the net magnetization, the dominant sublattice or the different anisotropies by changing the temperature. From a theoretical point of view, ferrimagnetic spin textures should display no skyrmion Hall angle as well as a high velocity in the vicinity of the angular momentum compensation temperature due to the vanishing of the net spin density. Also, the shift of the magnetization compensation temperature with the angular momentum compensation temperature makes the angular momentum compensation temperature suitable for spin textures manipulation due to a sizable net magnetization.

2. Experimental methods

In this chapter, the main experimental methods used within this work are described, while the results are presented in Part II. We first describe the sample deposition technique in section 2.1, i.e. the magnetron sputtering. In section 2.2, the electron beam lithography (EBL) is introduced, technique that was used to pattern our samples. Finally, section 2.3 focuses on different techniques of magnetometry and magnetic imaging. Since the results of chapters 4 and 5 have been acquired with the help of a scanning electron microscope with polarisation analysis (SEMPA) and a scanning transmission X-ray microscope (STXM), then these imaging techniques will be particularly viewed in-depth in sub-sections 2.3.5 and 2.3.6.

2.1. Magnetron sputtering

All the multilayers have been deposited using magnetron sputtering which is a physical vapor deposition (PVD) technique, i.e. a high-rate vacuum deposition technique with ultra high vacuum (UHV) base pressure that allows the deposition of many types of materials and particularly single metals and metallic alloys. In this work, a magnetron sputtering system "ATC-Orion 8" by AJA International Inc. has been used. PVD technic allows a very good control of the purity and composition of the deposited material by the use of confocal deposition using up to 8 targets, a control of the thicknesses of each layer of a multilayer and their cristallographic texture. The working principle can be seen in figure 2.1.
A substrate (generally Si_3N_4 in our case) placed on a sample holder is introduced in the UHV chamber via a load lock chamber. This load lock has a small volume to reduce the pumping time in comparison to the deposition chamber. After transfer, an inert gaz (Ar in our case) is introduced into the chamber and a high DC voltage is applied to the target (the target is at negative voltage). The free electrons present in the chamber will be accelerated and will enter in collision with the atoms of the inert gaz creating a plasma with Ar+ and e-. The Ar+ will be accelerated and attracted towards the target made of the material to deposit. If the kinetic energy of Ar+ is enough, the ejection of group of target atoms will be efficient and atoms will be deposited in all direction of space. The PVD deposition is not directive. The substrate, on top of the target at a distance of roughly 15cm, will also get some atoms and the layer will progressively grow.
The sputtering yield is low but the deposition rate can be increased by adding permanent magnets close to the target. The stray field of the magnet configuration causes the free and secondary electrons to be trapped and spiral in the vicinity of the target. This increases ionization events and increase the sputtering rate. This magnetic field

also allows to stabilize plasma at lower Ar pressure such that varying the Ar pressure allows to change the grain size and material cristallinity.
In this work, the alloy thin films have been obtained using cosputtering of two targets and the concentration of the alloy has been tuned by changing the deposition power of the two targets. Prior to material deposition, the deposition rate have been checked as a function of power and Ar pressure. In each multilayer, a buffer layer and a capping layer have been used. The buffer layer is used to promote interfacial DMI while the capping layer is used to prevent oxidation.

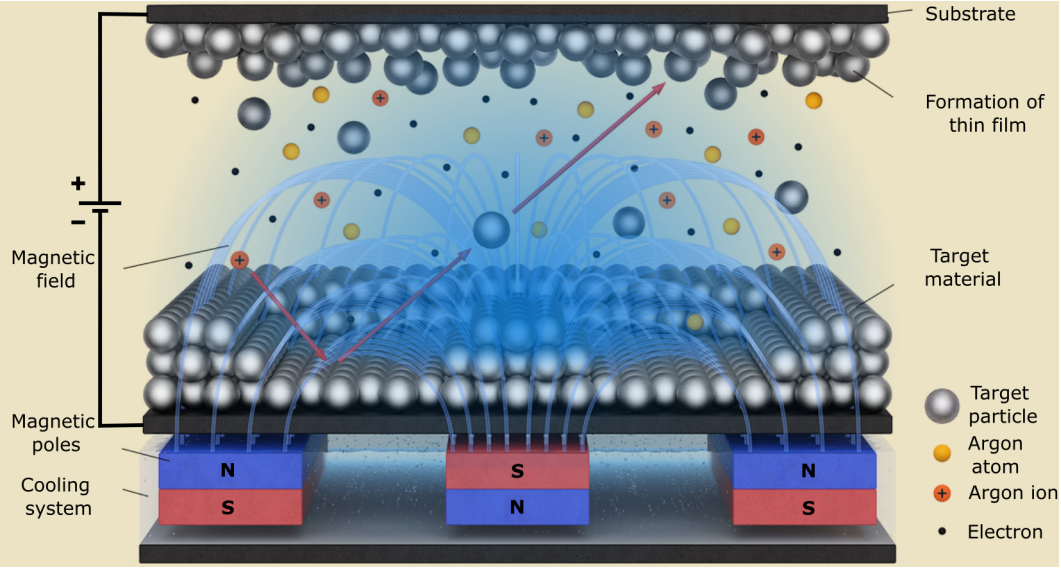

Figure 2.1.: Illustration of the magnetron sputtering process adapted from [28]. Ar ions are generated by collision with electrons presents in the UHV chamber where their density closed to the target is increased using magnetic fields (blue lines). By mean of electrical attraction, Ar ions are directed towards the target material and provoke an ejection of atoms that will be deposited onto the substrate (orange arrows).

2.2. Electron beam lithography

To investigate skyrmion dynamics via SOT (see chapter 5), the magnetic thin film has to be patterned into long wires. In order to inject current pulses, Au contact pads are deposited as seen in figure 2.2. The EBL technique is based on a focused electron beam that scanned a sample where a pre-coated electron-sensitive resist layer is present allowing to design structures down to 100 nm. After exposition of the resist, the sample is immersed in a solvent where the patterned (positive resist) or non-patterned (negative resist) part of the resist is dissolved. As seen experimentaly in Appendix A, ferrimagnetic materials are particularly sensitive to heat. Therefore,

positive resist with a lift-off process is favoured to deposite magnetic thin films where the details of the recipe will be presented in Appendix B. This make possible to sputter the material directly into a desired geometrical form such as wires or contact pads and avoid etching processes where heating effects are particularly visible.

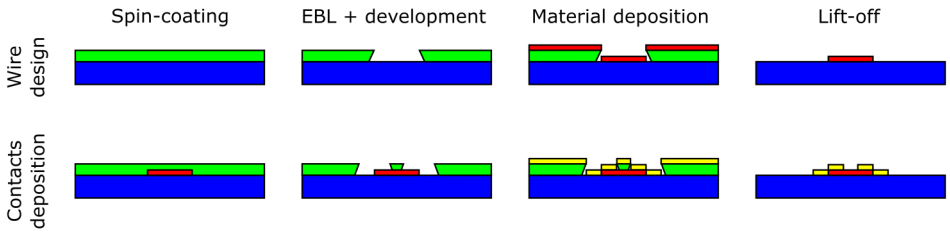

Figure 2.2.: Sketch of the lithography process with positive resist for current-driven dynamics of spin structures. The first row shows the different steps for materials deposition (red) while the second one focuses on the process of contact pads deposition (yellow).

2.3. Magnetometry and magnetic imaging

2.3.1. Superconducting quantum interference device

For a quantitative description of magnetic systems, it is important to extract with precision sample parameters such as the saturation magnetisation and the different anisotropies. For this purpose, a direct current superconducting quantum interference device (DC SQUID) is used which is a high sensitive magnetometer [29] based on Josephson junctions [30] [31] able to measure small magnetic moments at different temperatures and magnetic fields. During this thesis, we used a "Quantum design MPMS SQUID" where the working principle is based on two Josephson junctions. These are connected in parallel forming a superconducting ring where a bias current is applied leading to a detectable voltage. The current is formed from Cooper pairs of electrons tunneling equally in each junction. When a magnetic field is applied, an additionnal screening current is added to the loop which have for consequence of putting a phase difference between the two junctions. Following the laws of quantum mechanics, the magnetic flux enclosed by the superconducting ring is quantized in integrer of the magnetic flux quanta ϕ_0. When the flux administred to the SQUID exceeds half of the magnetic flux quanta, it is more favorable for the system to increase the penetrating flux till ϕ_0 by reversing the screening current. By increasing more and more the magnetic flux, the flux crossing the SQUID adds again screening currents into the loop till another supplementary half magnetic flux quanta is reached where the screening current is reversed again. This makes a ϕ_0-periodic system where one periode is counted as one unit of the magnetometer.

2.3.2. Magneto-optical Kerr effect laser

Due to their time and Helium consumption, SQUID is not an ideal technique for quick and cheap check of usual magnetic parameters such as the direction of the magnetization, the saturation and coercitive magnetic fields or the dominant sub-lattice in a ferrimagnetic materials. For these purposes, a magneto-optical Kerr effect (MOKE) laser is prefered.
The key principle of this type of magnetometers is the change of a polarized incident light in direction, intensity or even nature after reflection on magnetic materials. A linear polarization is equivalent to the sum of two circularly polarized components with equal amplitude but opposite helicities. According to the theory, the spin-orbit interaction leads to different index of refraction for left and right circular polarized lights [32] [33] which causes the two circular polarization lights to propagate discordantly after reflection. The sum of them becomes an elliptical polarization light that can be defined by the Kerr ellipticity angle ϵ_K (change of amplitude) and the Kerr rotation angle θ_K (change of phase) following the two equations:

$$\epsilon_K = \frac{I(f)}{4J_1(\delta_0).I(0)} \tag{2.1}$$

$$\theta_K = \frac{I(2f)}{4J_2(\delta_0).I(0)} \tag{2.2}$$

where J_n are the Bessel functions of order n. In our case, we are interested in θ_K since it is sensitive to the unidirectional direction of the TM magnetization vector allowing us to diferrenciate TM/RE-dominant ferrimagnet. Therefore, the second harmonic signal will be measured.

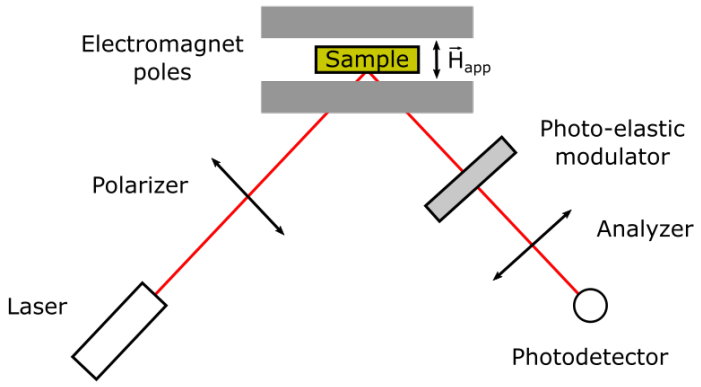

Figure 2.3.: Schematic of the Kerr laser in polar geometry.

For the Kerr laser setup (see figure 2.3), a He-Ne laser is used to determine the magnetic state of the sample where its wavelength is chosen at 633 µm to mainly probe

the TM sublattice of the TM-RE ferrimagnet [34]. This makes MOKE laser a powerfull tool to measure samples closed or even at the compensation temperature where the overall magnetization vanishes. Before its reflection on a magnetic sample, the beam is s-polarized using a polarizer with its axis of polarization placed perpendicularly to the beam and parallel to the optic table. After reflection, the polarisation is modulated using a photo-elastic modulator (PEM) at 50 kHz with $\delta_0 = 3.05$ rad which maximizes the Bessel function of order 2 that makes $I(2f)$ maximizes as well. After the PEM, the beam is going though a second polarizer (analyzer) placed at 45° compared to the PEM axis and finally reaches a photodiode. The signal is measured by a lock-in amplifier where its reference is taking with the PEM. For polar geometry (mainly used in this thesis), an OOP magnetic field is used to change the magnetic state of the sample. Any change of the magnetic state will then provoke a difference in the intensity detected in the photodiode which makes possible to perform hysteresis loops.

2.3.3. Kerr microscope

While the MOKE laser determines macroscopically the magnetic properties of thin films, the effects responsible of this come from their magnetic microstructure as seen in the subsection 1.2.5. Therefore, a closer look at magnetic domains and their magnetic field-response is essential to understand the different mechanisms causing these magnetic behaviours. Within this thesis, we used an "Evico magneto-optical Kerr microscope" to observe micrometric sizes spin structures such as magnetic domains or magnetic bubbles. Our setup is used to visualize the OOP contrast at different magnetic fields while current pulses can be applied through patterned structures allowing us to observe the current-driven dynamics of spin structures. A cryostat has also been available for temperature dependence measurements making finally Kerr microscope a fulfilling laboratory-based imaging technique.

The Kerr microscope technique (see figure 2.4) consists in LED white light sources that are focused at the aperture using a collector. The slits of the aperture are present to adjust the sensitivity direction of the magnetization by selecting the angle of incoming light. A converging lens is placed at the focal distance with respect to the aperture aligning the central beams of the light. A field diaphragm is placed after the lens to select the center part of the light. Afterwards, the light is reflected on a reflector, polarized through a polarizer and is directed through the objective used to change the magnification and focus on the surface of the sample. After reflection of the linearly polarized light, the light becomes elliptical and a compensator is placed on the beam trajectory to polarize the light linearly again. At the end, an analyzer will be placed almost perpendicularly with respect to the polarizer to extinguish more or less the light and observe the component that has been created after reflection. The light will finally reached the CCD camera where the intensity is analyzed to determine the magnetic configuration.

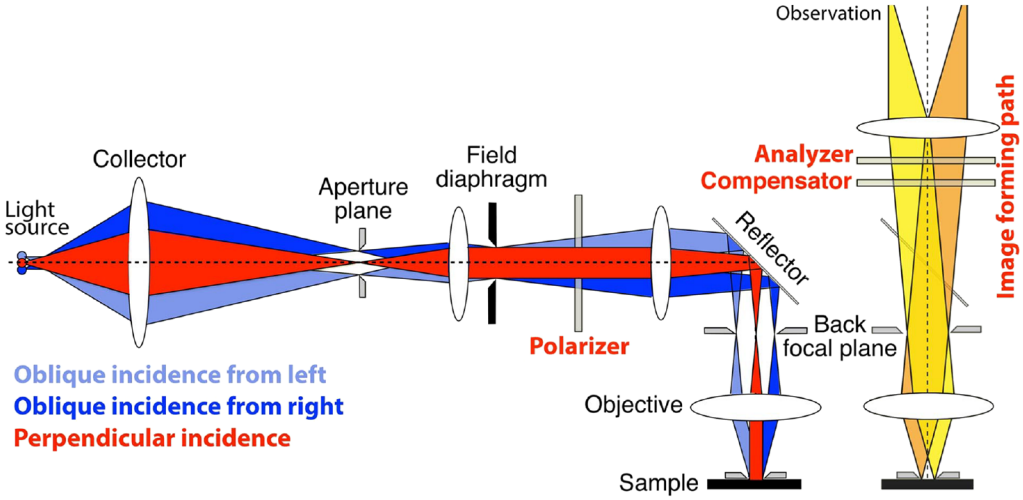

Figure 2.4.: Sketch of the Kerr microscope extracted from [35].

2.3.4. Magnetic force microscopy

When nanostructures have lateral dimensions below several 100 nm, Kerr microscopy reaches its resolution limit due to the wavelength of the light used. To observe submicrometer spin structures, a "Veeco Dimension 3100" magnetic force microscope (MFM) has been used. A MFM is a variety of near field microcope derived from the atomic force microscopy (AFM) technique [37] [38]. The working principle of this technique relies on the detection of the interaction between a magnetic tip and the stray field arising from the magnetization distribution of the sample. As seen in figure 2.5, a magnetic tip is placed on a cantilever and it is following the surface at a constant distance in order to avoid change of the Van der Waals force with the surface. The tip is oscillating. The detection of the variation of the oscillation frequency is a direct measure of the gradient of the magnetic force acting on the tip. Depending on the tip magnetization direction, the flow over magnetic domains of opposite magnetizations will lead to an increase or decrease of the oscillation frequency. MFM has a high resolution below 20 nm and is able to detect only few atomic layers of ferromagnetic materials. However, since it relies on the tip-sample interaction, ferrimagnetic materials are particularly difficult to detect due to their reduced magnetization. Therefore, for ferrimagnetic materials possessing small magnetic moment, other imaging techniques will be necessary for observation of small magnetic pattern. Furthermore, the MFM does only give access to the second derivative of the stray field and the interpretation is sometimes difficult. Indeed, one MFM constrast can be given by different magnetic configuration. Therfore, MFM is often combined with macroscopic measurements, micromagnetic calculations or other imaging techniques.

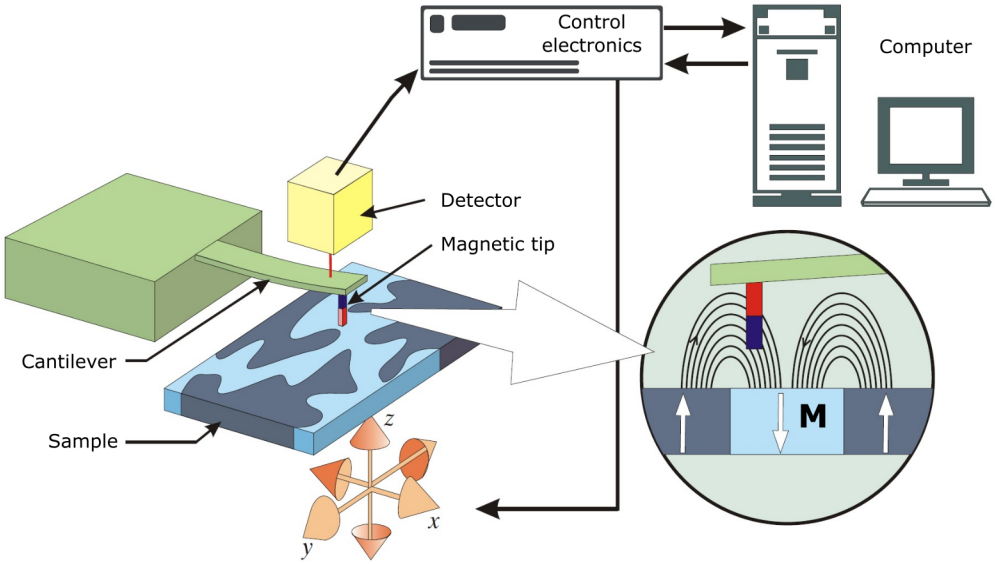

Figure 2.5.: Working principle of MFM extracted from [36].

2.3.5. Scanning electron microscopy with polarization analysis

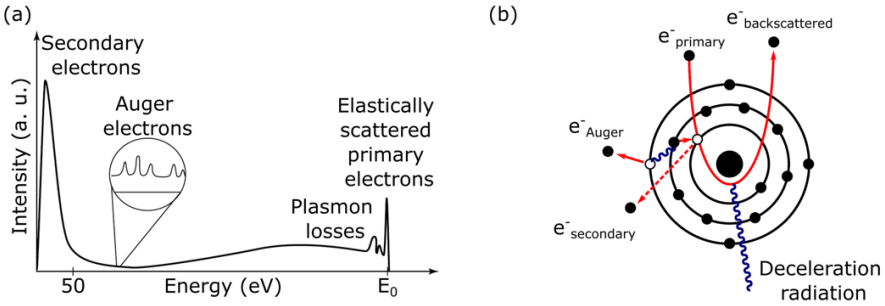

Figure 2.6.: (a) Energy spectrum of backscattered electrons using a primary electron beam of energy E_0 from a metal surface. (b) Sketch of the Auger electron nucleation process. Figure adapted from [39].

The first SEMPA was realized by K. Koike *et al.* in 1984 [40] based on ideas of T. H. DiStefano [41] and J. Unguris *et al.* [42]. This is a laboratory-based 2-dimensional magnetic imaging technique capable of simultaneously vizualising both IP components of surface spin structures with a high spatial resolution [43] that can go down to 3 nm [44]. This is a powerfull surface-sensitive technique to observe IP magnetic domains [40] [45] and domain walls of ferromagnetic OOP-magnetized spin structures [46] [47]. This technique is based on the polarization analysis of the secondary electrons emitted from the sample when hitting it with a focused

unpolarized primary electon beam that is scanning its surface. Due to sub-nm spin decay lengths in metals, SEMPA is a surface-sensitive technique which can only probe the topmost atomic layers of a sample.

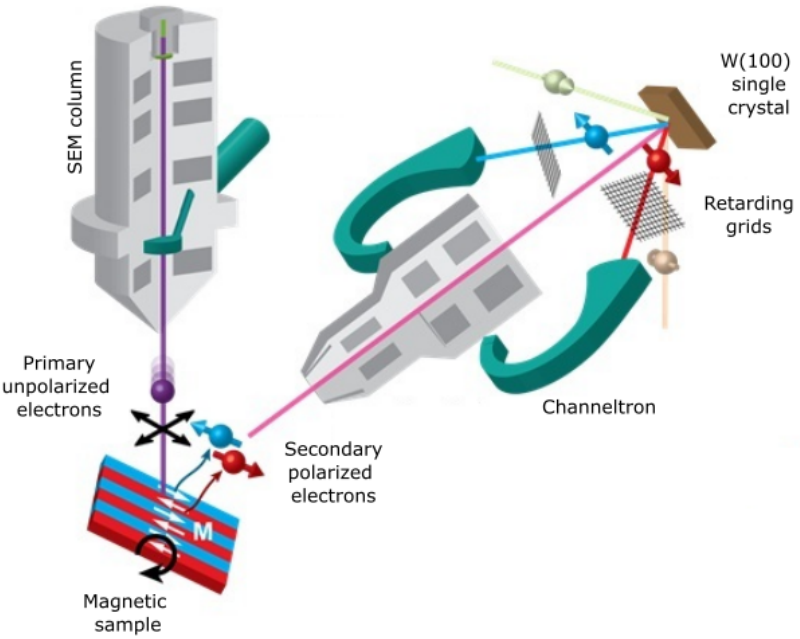

Figure 2.7.: Sketch of the SEMPA setup. Unpolarized electrons from the SEM column are scattered at a magnetic material. Polarized secondary electrons are emitted from the sample, directed onto a W(100) single crystal and redirected to electron detectors. Adapted from **??**

Concerning our experiment [48], the SEMPA is a commercial UHV instrument from "Scienta Omicron" where an ultrafine primary electron beam is created using a SEM column. The primary electrons of energy E_0 are sent to the sample and scatter with the upper atomic layers of the materials. As seen in figure 2.6 a, different scatter events are presents in the energy spectrum of emitted electrons. Firstly, electrons can be scattered elastically showing a sharp peak at the high energy E_0. Next to this energy, others are scattered inelastically through low plasmon losses. Primary electrons can also eject electrons from inner shells (secondary electrons), where the vacancy will be filled up with a higher energy level electron. For an energy conservation of the system, the shell jump of the electron can be accompanied by a photon emission corresponding to the difference of energy levels between the old and new state of the electron. The energy of the emitted photon can be transferred to another electron with higher energy that will itself be ejected from the atom and called an Auger electron as seen in figure 2.6 b. Finally, cascade scattering

processes of backscattered primary electrons, inner shell electrons ejected and Auger electrons induce an energy loss before these eletrons are leaving the material. This will provoke a high intensity energy peak located of few eV where these electrons are called secondary electrons. In the secondary electrons regime, below 30 eV, there is a strong unbalance of the spin-up/spin-down density of state in itinerant ferromagnet which results in a sizable polarization of the secondary electrons emitted from the sample. Therefore, by analysing the spin direction of these electrons, it is possible to determine the local probed magnetization. The electrons emitted from the sample are then collected, accelerated to 104 eV and sent onto a W(100) single crystal. Here, they are scattered with different probabilities in different directions depending on their spin orientation as shown in the sketch of figure 2.7. This is based on the low-energy electron diffraction (LEED) technique where the electrons diffracted in the four (2,0) LEED beams are collected and analyzed. Afterwards, inelastically scattered electrons and secondary electrons from the W(100) crystal are repelled by retarding grids. At the end, electrons are going in different channeltron electron to be counted electronically.

Since SEMPA is based on the analysis of the secondary electrons ejected from the sample, it only gives informations on the surface magnetization of the sample, which could cause misinterpretations. Therefore, careful attention has to be given in the analysis. To complement this, a transmission imaging technique allowing to observe magnetic configurations through the whole thickness such as STXM can be useful.

2.3.6. Scanning transmission X-ray microscopy

STXM is a high-resolution microscopy technique in transmission that allows to observe magnetic patterns using a synchrotron radiation source. During this thesis, we performed STXM imaging using the "MAXYMUS" beamline at the Helmholtz-Zentrum Berlin [49] and the "PolLux" one at the Paul Scherrer Institut [50]. In this type of synchrotron facilities, electrons are accelerated at relativistic speeds and guided in a ring in a circular way using bending magnets. To produce soft X-rays, one uses Tesla-range magnetic fields called undulators. These are formed from a periodic assembly of permanent magnets which constrain the electrons to move on a undulating path. The multiple change of trajectory in this form induces the electrons to emit circularly polarized electromagnetic radiation in the X-ray range. Undulators can be tuned to emit predominantly electrons of the desired energy by changing the amplitude of oscillation of the electrons. This can be done by adjusting the gap between the two set of magnets where the electrons are oscillating. To select the energy more precisely and get monochromatic X-rays, a plane-grating monochromator is used followed by a pinhole as seen in figure 2.8. In order to focus the beam diverging out of the pinhole on the sample, a Fresnel zone plate is used which consists in concentric rings that alternate between transparent and opaque to the X-rays beam. The X-ray radiation adds up coherently through the transparent rings by means of diffraction and is focused few mm away where the sample is placed. Just before the sample, a

second pinhole called an order sorting aperture (OSA) is centrally mounted to remove unwanted diffraction orders from the zone plate. The beam goes then through the sample and the transmitted intensity is detected by photon detector. To scan the sample and get a 2-dimensional observation of magnetic structures, the sample itself is moved perpendicularly to the beam direction.

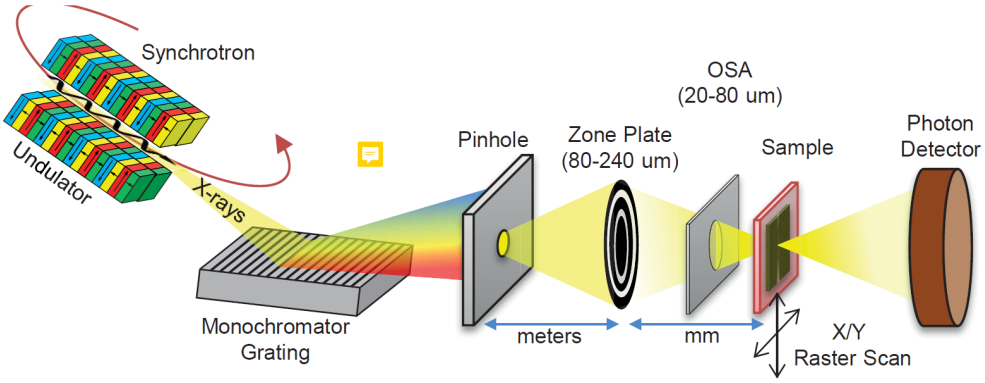

Figure 2.8.: Sketch of the working principle of a STXM extracted from [49].

For 3d ferromagnetic elements such as Fe or Co at the L3 absorption edge, the absorption cross sections of circularly polarized X-rays depend on the direction of the crossed magnetization with respect to the photon k-vector [51] [52]. This is principally due to the spin splitting of the 3d band in TM. This phenomenon is called X-ray magnetic circular dichroism (XMCD) allowing us to differenciate up and down domains by analyzing the intensity of the light transmitted. STXM can also be used to determine the local direction of the magnetization of uniformly magnetized samples by comparing the intensities using the two helicities of circularly polarized X-rays.

To allow the transmission of X-rays through the sample in STXM, the magnetic films are deposited on substrates consisting of ultrathin windows of 100 nm thick silicon nitrate called membranes.

3. State of the art

In this chapter, we present some important findings regarding magnetic skyrmions over the last decades. Also, a critique discussion on current or possibly future applications will be present. As a note, this chapter has no aim of presenting an overall overview on the topic but will only give us a comprehensive vision on the subject in advance of the presentation of our results. This will then highlight our contribution and open the discussion on further perspectives.

3.1. Magnetic skyrmions

3.1.1. The emergence of magnetic skyrmions

Magnetic skyrmions have been theoretically predicted [53] using the work of T. Skyrme in the field of particle physics describing a particle-like solution of interacting mesons [54] [55]. In 2009, S. Mühlbauer *et al.* performed the first observation of magnetic skyrmions [56] where they have observed a skyrmion lattice in MnSi crystals in the reciprocal-space using neutron scattering techniques at low temperatures. Since then, magnetic skyrmions have also been observed by direct imaging including laboratory-based techniques such as Lorentz transmission electron microscopy [57] [58] or Kerr microscopy [59] [60] making the observation of magnetic skyrmions more accessible.

3.1.2. Observation at room temperature

While magnetic skyrmions were only observed in B20 materials at cryogenic temperatures [56] [57] [61] [62] [63], recent studies confirmed their stabilization at room temperature or above in different type of materials such as metallic materials [64] or insulators [1] [65]. This breakthrough emanates from the idea of inducing a DMI owing to a large SOC material at the interface: an interfacial DMI. This makes the presence of magnetic skyrmions at room temperature accessible in numerous systems.

3.1.3. Current-driven dynamics via SOT

More than their meta-stable character, the behaviors of magnetic skyrmion under current application is particularly interesting. S. Woo *et al.* reported the first study on the dynamics of magnetic skyrmions via short current pulses in multilayer stacks

[1] Not studied in this thesis, the use of magnetic skyrmions in insulators can be really interesting due to the low damping of the material inducing a high velocity of these particle-like spin textures via SOT. Also, the absence of ohmic losses in insulators, especially present in metallic-based materials, is a real benefit for low consumption applications.

such as $[Pt/CoFeB/MgO]_{15}$ [64]. They engineer their material in a way that a thin ferromagnetic layer is sandwiched between a heavy metal and an insulator. The heavy metal has two functions: inducing a sizable interfacial DMI and creating a vertical spin current that will initiate the dynamics of skyrmions via SOT as described theoretically in the section 1.4.4. Concerning the MgO layer, it separates the ferromagnetic layer and the heavy metal in the multirepetition system allowing to keep a strong DMI arising from the other interface while avoiding ohmic losses [66] [67]. Finally, they show that skyrmions move in a deterministic manner reaching a speed that could exceed 100 $m.s^{-1}$.

J. Sampaio *et al.* predicted that magnetic skyrmions are not moving collinearly with the applied current direction but at an angle originating from the topological charge of the quasiparticle [68] which was confirmed experimentally few years later in different works [24] [25]. To suppress this unwanted effect, non-trivial spin textures with zero topological charge have been proposed such as ferrimagnetic skyrmions [69] or skyrmionium [70].

3.1.4. Ferrimagnetic skyrmion and skyrmionium

S. Woo *et al.* performed the first experience on the dynamics of ferrimagnetic skyrmions in $[Pt/GdFeCo/MgO]_{20}$ ferrimagnet [69]. The skyrmions nucleated in these materials reach the speed of 50 $m.s^{-1}$ with a reduced skyrmion Hall angle of about 20° due to a reduced effective topological charge in uncompensated ferrimagnetic materials. In this case, the multirepetition of the [Pt/GdFeCo/MgO] makes the nucleation of magnetic skyrmions easier due to the stray field coupling while a sizable DMI induced their homochiral character. However, this makes their stabilization at the magnetization compensation temperature in this material impossible due to the absence of coupling between each ferrimagnetic layer. Their study is nevertheless a first step to get quasiparticles with zero skyrmion Hall angle at high velocity which we will also explore with another ferrimagnetic material in the chapter 5 of this thesis. In GdFeCo single magnetic layer materials, Y. Hirata **et al.** shows the vanishing skyrmion Hall effect at the angular momentum compensation temperature of pinned chiral spin textures [71].

Another way of extinguishing the skyrmion Hall effect is the possibility of using skyrmionium, quasi-particle described in the section 1.3.4. Especially, X. Liang *et al.* shows that skyrmionium in ferrimagnet should display robust dynamics compared to ferromagnetic or ferrimagnetic skyrmions following micromagnetic simulations [72]. During this thesis, we performed the first observation of ferrimagnetic skyrmionium [73] in GdFeCo-based ferrimagnet where the results will be presented in the chapter 4.

3.1.5. Writing, deleting and reading topological spin textures

A last point to look over is the control of the nucleation, annihilation and detection of these spin textures which we will review below.

- Writing

Several approaches have been proposed to carry out the nucleation of magnetic spin textures like by using current [74] [68] [75], local magnetic field [76] [77] or laser pulses [78] [79]. More preciesely, J. Sampaio *et al.* have proposed to nucleate locally a magnetic skyrmion using spin-polarized current [68]. Explanation possible: Their micromagnetic simulations show that the torques exert on a trivial magnetization state in confined geometry via the spin polarized current will perturbated the system and switch the magnetization in a skyrmion-like form making the reproducible nucleation of magnetic skyrmion possible. Also, S. Zhang *et al.* have suggested another method by using the local magnetic field gradient arising from a magnetic tip such as the ones using in MFM. Here, they observed the nucleation of a skyrmion lattice which is the lower-energetic state in their system reached after the relaxation of the system due to the perturbation coming from the magnetic tip [76]. This writing approach has also been observed during this thesis where the results will be presented in the appendix C. In our case, we observed the nucleation of multiple magnetic skyrmions from a multidomain state after scanning the surface with a magnetic tip.

- Deleting

The annihilation process has been made in evidence by the work of N. Romming *et al.* where they show that magnetic skyrmions can be annihilated by the injection of higher-energy electrons through local voltage [80]. Also during our experiment, we observed that injection of high current density into a wire leads to the annihilation of magnetic skyrmions. This will be described more precisely in the section **??**. Other methods have been proposed with the use of spin waves [81] or electric fields [82].

- Reading

The presence of magnetic skyrmions leads to an additional contribution in the Hall response through the topological Hall effect. Therefore, it is possible to read magnetic skyrmions electrically as seen experimentally by A. Neubauer *et al.* in the *A* phase of MnSi crystals [23]. Also, C. Hanneken *et el.* have shown the feasability of the electrical detection of magnetic skyrmions by measuring the tunnelling non-collinear magnetoresistance in a PdFe/Ir(111) sample [83].

3.1.6. Conclusion

The stabilization of particle-like spin textures at room temperature has been observed in numerous systems. Furthermore, the deterministic dynamics of magnetic skyrmions, especially efficient via SOT, has been demonstrated experimentally as well as the reproducible creation or annihilation of skyrmions and their robust detection. This all together opens the path of future skyrmion-based spintronic devices.

3.2. Skyrmion-based spintronic devices

3.2.1. Racetrack memory

A racetrack memory is an experimental non-volatile memory that has been proprosed by IBM based on magnetic domains where the information stands in the direction of their magnetization [84]. Much smaller and theoretically faster than magnetic domains, magnetic skyrmions can also be implemented in such devices [85] [86]. In this type of memory, the information is encoded by the presence or the absence of a magnetic skyrmion where their manipulation is electrically completed such as seen in figure 3.1.

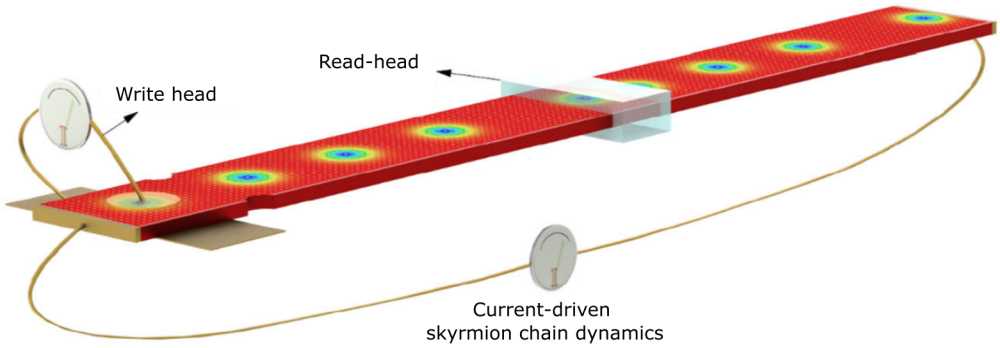

Figure 3.1.: Illustration of a design for a skyrmion-based racetrack memory extracted from [87]. Data are encoded by a chain of magnetic skyrmions along the nanostripe. Spin-polarized current pulses are used to drive the collective motion of the skyrmion chain along the wire while the writing (or deleting) and the reading processes are completed electrically.

However, magnetic skyrmions tends to have a homogeneous distribution over time due to the skyrmion-skyrmion interaction [88] [89] leading to the loss of the stored information [12]. To overcome this, M. Hoffmann *et al.* have proposed a racetrack memory where the information is encoded in two type of magnetic spin textures such as skyrmions and antiskyrmions making the use of racetrack memories based on skyrmions possible [90]. With the possibility of stabilizing multiples spin textures, one can then imagine a bit of multiple value increasing considerably the infomation stored.

3.2.2. Logic gates

X. Zhang *et al.* performed micromagnetic simulations that reproduced the "OR" and "AND" logic gates using magnetic skyrmions in input [91]. The general ideas are that magnetic skyrmions can be manipulated electrically, deformed and merged together. In figure 3.2, magnetic skyrmions are deformed into magnetic domains when they are

directed towards wires narrower than their size. In the case of the "OR" gate in figure 3.2.a, two small paths merged into a small wire. If a magnetic skyrmion or two are present in the entry, it will lead to a magnetic domain accross the whole wire width. Conversely, in order to get a magnetic domain accross the whole width in a larger wire as seen in figure 3.2.b, it is mandatory to have two magnetic skyrmions in input. They designed their structures in a way that it is necessary of having a magnetic domain covering the whole wire width to get a magnetic skyrmion in output. This all conduct the two different geometries (small and big wires) to represent two different logic gates based on magnetic skyrmions.

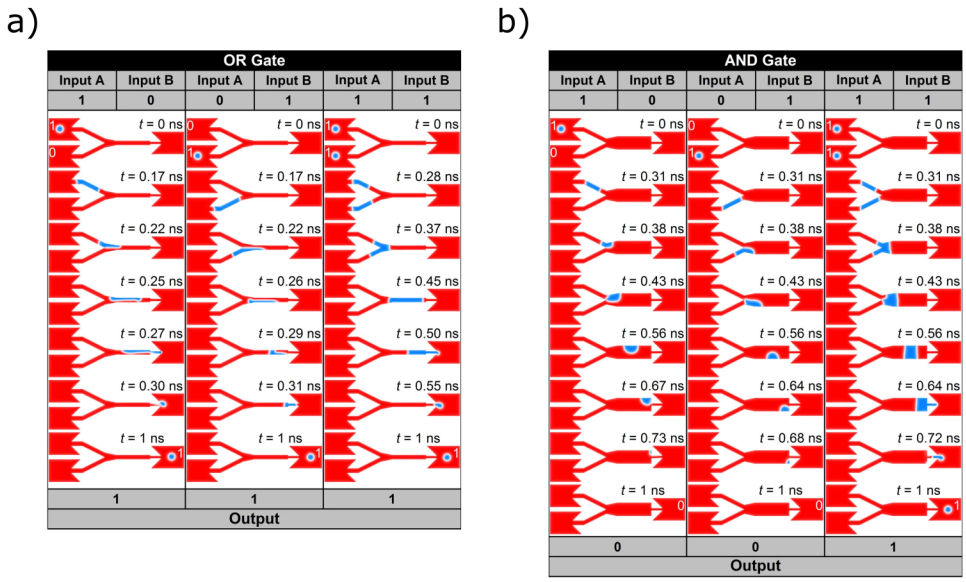

Figure 3.2.: Schematic working principle of a (a) "OR" and a (b) "AND" logic gates based on magnetic skyrmions extracted from [91].

3.2.3. Conclusion

Here, we presented the two mains applications of skyrmions-based devices, namely the racetrack memory and the logic gates. Howewer, many other applications have been proposed such as radio-frequency devices [92] [93], magnonic crystals [94] or reshufflers [60].

Part II.

Experimental results

4. Direct observation of pure Néel-type spin structures in GdFeCo-based ferrimagnet

4.1. Introduction

As discussed in part I, chiral spin textures are particularly interesting for the next generation of spintronic devices. They have already been seen in ferrimagnetic materials where their interesting properties such as a reduced skyrmion Hall angle have been observed [69] [71]. This type of spin textures can be moved electrically via SOT that act efficiently on Néel-type spin textures [85] [95]. Therefore, this first study that is presented in this thesis focuses on the nucleation of homochiral Néel-type spin textures in GdFeCo-based ferrimagnetic material. Since the chirality of these spin textures is often difficult to ascertain due to the narrowness of DW, we propose to use SEMPA, i.e. a high resolution imaging technique, to observe DW in ferrimagnet for the first time.

4.2. Thin film engineering

As seen in section 1.3.1, the nucleation of Néel-type spin textures in thin magnetic film is facilitated by a strong interfacial DMI. Thus, the engineered material is sandwiched betwenn two HM, Ir and Pt, such as $Si//Ta(5)/Ir(5)/Fe(0.3)/GdFeCo(8)/Pt(5)$ with the thickness of each individual layer given in nanometers in parentheses. The top Pt layer is also used as a capping layer to avoid the oxydation of the thin films. In these films, an ultrathin Fe(0.3) dusting layer was inserted between Ir and the ferrimagnetic layer to enhance the interfacial DMI, which was calculated to be negative[1] at the Ir/Fe interface [62]. At the other interface, the DMI at the Co/Pt or Fe/Pt interfaces is expected to be particularly strong and negative [5] [96] [97] while no information from our knowledge is present for the interfacial DMI with Gd atoms which is however supposed to be much smaller than with Co or Fe atoms. The Ta buffer layer is here to induce a crystallographic ordering of the Ir layer in the 111 plane that will itself enhance the interfacial DMI [62]. The GdFeCo ferrimagnetic alloy possesses a strong perpendicular magnetic anisotropy (PMA) closed to the compensation magnetization temperature due to a lower magnetization making them less sensitive to external

[1] As a note, there are also estimations of a positive value of the DMI at Ir/Fe interfaces [5]. Therefore, one has to be careful with assumptions concerning the sign of the interfacial DMI at this interface.

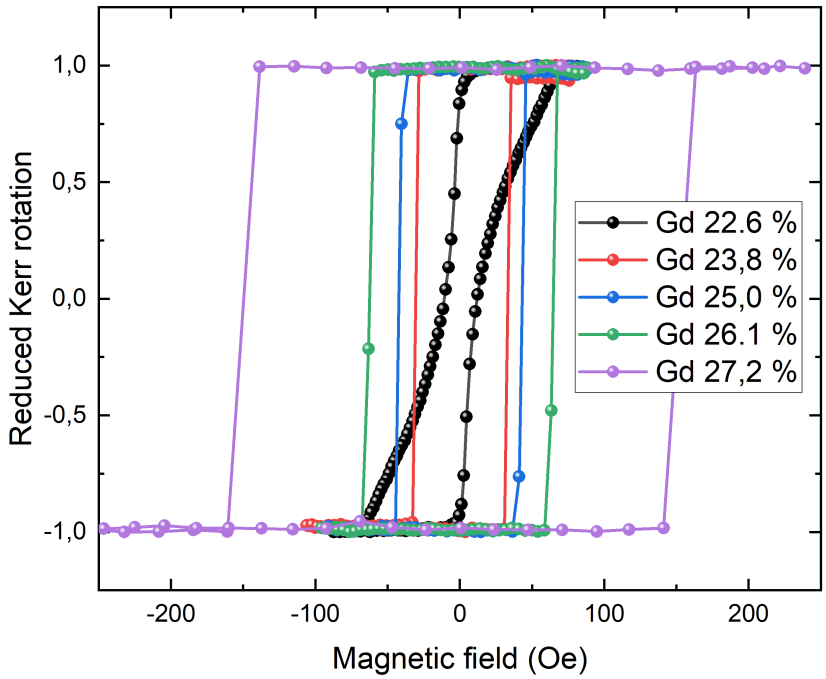

Figure 4.1.: Kerr rotation on $Si//Ta(5)/Ir(5)/Fe(0.3)/Gd_xFeCo_{1-x}(8)/Pt(5)$ as a function of the Gd content x measured with MOKE

magnetic fields while being less subject to the stray fields [97]. In contrary, stray fields are strong for ferrimagnets further away from the compensation temperature favoring an IP anisotropy where the transition between OOP and IP anisotropies is called the spin reorientation transition (SRT) particularly favorable for the stabilization of non-collinear spin textures. In figure 4.1, one can observe hysteresis loops of these magnetic thin films for different stoichiometry of the ferrimagnetic alloy using MOKE laser where only the ratio between RE atoms with TM ones changes. The technique allows to detect the dominant sublattice where the sign has been put by convention showing TM dominant sublattice for positive response at positive magnetic field. Therefore, one can conclude that all the thin films presented here are TM dominant. Also, the increase of the coercive field H_c by rising the presence of Gd atoms means that the ferrimagnetic alloys is closer to the magnetization compensation temperature which makes sense for TM dominant alloys. Far away from the magnetization compensation temperature, for a Gd content of $Gd_{\%} = 22.6\%$ (black loop in figure 4.1), the SRT starts to be visible where no sharp switching is present and where spin textures start to nucleate close to zero magnetic field. To image spin textures, SEMPA has been used which is a surface sensitive technique unable of visualizing through 5 nm of Pt

capping layer. Therefore, one has to milled the capping layer down to 1.5 nm before imaging such as:
— Sample 1: $Si//Ta(5)/Ir(5)/Fe(0.3)/Gd_{26.1}Fe_{65.5}Co_{8.3}(8)/Pt(1.5)$

4.3. Stabilization of spin textures

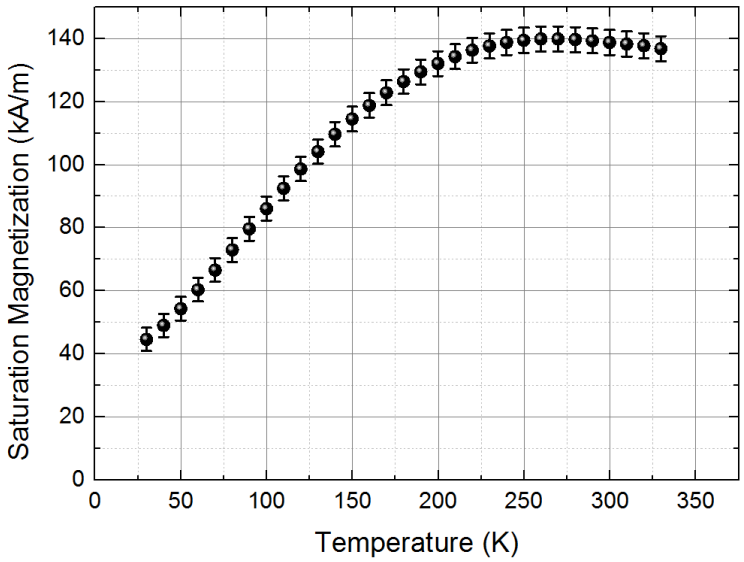

Figure 4.2.: Saturation magnetization as a function of the temperature measured with SQUID for sample 1.

The aim of depositing thicker capping layer than necessary is the used of Ar ion milling to reduce the capping layer that will introduce defect centers in the material making the nucleation process of spin textures much more easier even for samples possessing strong OOP anisotropy. In order to analyze the DW of spin textures, the easiest solution is to image not too closed from the magnetization compensation temperature where the anisotropy is small enough leading to large DW width following equation 1.41. The milled sample displays a TM dominant character in the whole temperature range since the saturation magnetization value is going down by cooling the sample without reaching the zero net magnetization. In figure 4.2, one can observe the saturation magnetization temperature being higher in the high temperature regime meaning that the sample is strongly TM dominant at high temperatures while being closer to the compensation magnetization temperature at lower temperatures. The spin textures stabilized at room temperature (RT) possess DW that should be large enough to be detected while allowing to go down in temperature to image magnetic spin textures with different sample parameters. In figure 4.3.a, one can see hysteresis loops of milled and unmilled sample where the nucleation field has been reduced at

RT. The nucleation field represents the field necessary to nucleate a domain where its reduction is due to locally reduced anisotropies arising from the nucleation sites introduced previously. The nucleation process is made with the help of a damped oscillating IP magnetic field where micrometer-sized up-oriented spin textures have been nucleated randomly as seen in figure 4.3.b.

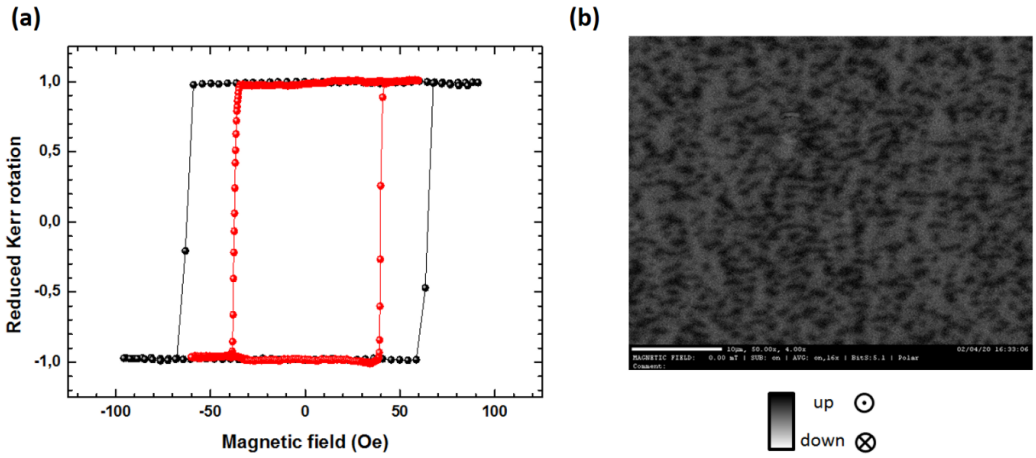

Figure 4.3.: (a) Hysteresis loops performed with a MOKE laser on $Si//Ta(5)/Ir(5)/Fe(0.3)/Gd_{26.1}Fe_{65.5}Co_{8.3}(8)/Pt(5\,or\,1.5)$ before (black) and after (red) milling of 3.5 nm of the Pt capping layer. (b) Kerr microscopy image of OOP spin textures after the nucleation process of the milled sample at RT and zero magnetic field. Scale bar in (b): 10 µm.

4.4. SEMPA imaging at room temperature

After nucleating the OOP spin textures, SEMPA (see section 2.3.5) is used to localize the DW as well as detecting the spin distribution inside them. This will then make possible to determine the DW width as well as the chiral character.

4.4.1. Domain wall width

The milled ferrimagnetic sample is loaded in the SEMPA chamber after the nucleation process where the direction and the magnitude of the IP magnetizations, respectively M_x and M_y, are imaged under zero magnetic field as seen in figures 4.4.a-b. Here, contrast in the DW can be observed, where the in-plane magnetization is expected in DW of OOP spin textures, with a brighter contrast present for the left (top) of each domain indicating a left (up) tendency for the local direction of the magnetization. Conversely, dark contrast is seen at the right (bottom) edges of the domains, as

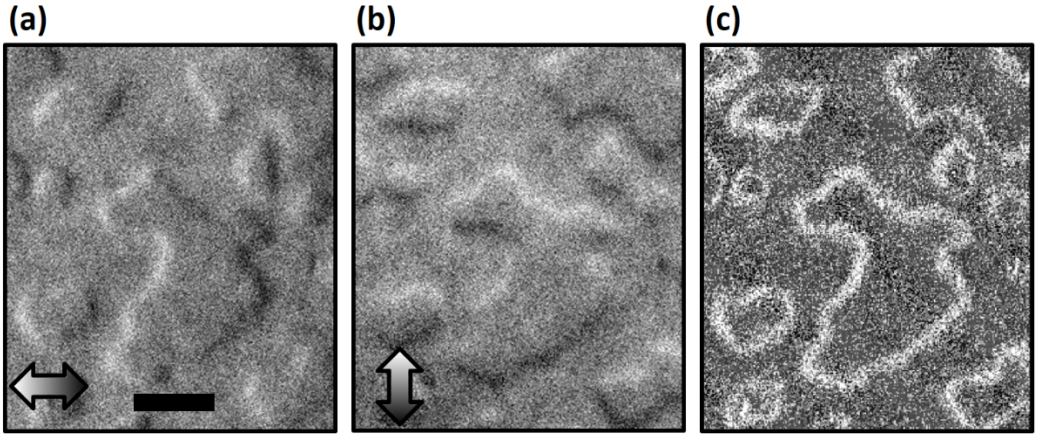

Figure 4.4.: Determination of the average DW width of spin textures imaged in sample 1 taken with SEMPA at RT. (a) Horizontal and (b) vertical in-plane components of the magnetization. The direction of magnetization is indicated by the grayscale contrast as displayed on the double arrows. Scale bar in (a): 1 µm. (c) Reconstruction of the absolute in-plane magnetization intensity. The white contrast indicates a saturation in-plane magnetization.

shown in the double arrows in figures 4.4.a-b. In figure 4.4.c, the absolute in-plane magnetization image has been generated using the following equation at each local position:

$$|\mathbf{M}|_{IP} = \sqrt{M_x^2 + M_y^2} \tag{4.1}$$

where the brighter contrast indicates the in-plane saturation magnetization. This contrast clearly indicates the position of the DW where in-plane components are then present. To determine the position of the skeleton of the DW, i.e. the line at the center of the DW, one first binarizes the image leading to a binary image where the white contrast indicates the DW while the dark areas show pure OOP spin textures as seen in figure 4.5.b. To end up with the skeleton of the DW, a shrink function is applied to the binarized DW as display in figure 4.5.c. The skeleton is cut into several parts where each part is fitted with a polynomial function. The advantage of fitting the skeleton with mathematical functions is the possibility of extracting analytically the local tangente (or its perpendicular) at each point of the skeleton. This make then possible to establish the DW intensity profile shown in figure 4.6 by averaging the measured local DW profile at each position of the skeleton.
However, the imaged DW profile needs to be carefully analyzed in order to obtain the true profile, principally due to the broadening of the features due to the finite size of the beam profile. The experimental profile can be approximated as the convolution of the theoretical DW profile with the electron beam distribution as follows:

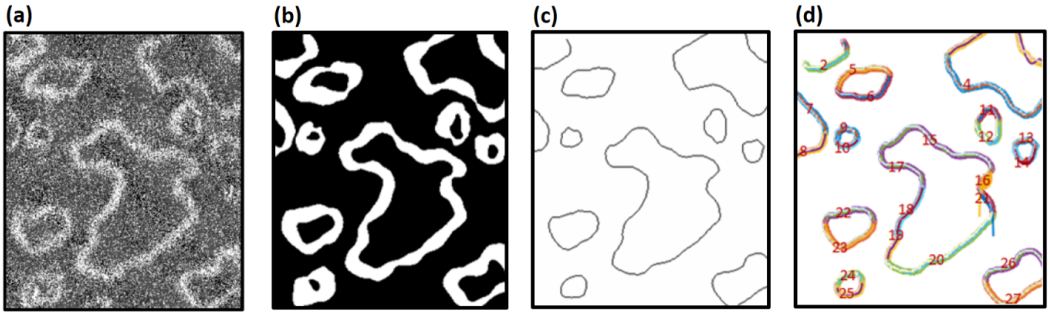

Figure 4.5.: Method to fit the skeleton using polynomial functions. (a) IP intensity image taken with SEMPA at RT of our GdFeCo-based ferrimagnetic alloy. (b) Binarization of the image (a). (c) Skeleton of the image (b). (d) Decomposition of the skeleton into several parts allowing a fit of each section of the skeleton with a polynomial function.

$$\mathbf{DW}_{profile} = cosh^{-1}(\frac{x}{\Delta}) \bigotimes e^{-\frac{x^2}{2\sigma^2}} \tag{4.2}$$

where the hyperbolic function represents the real DW profile and the Gaussian function describes the electron beam distribution.

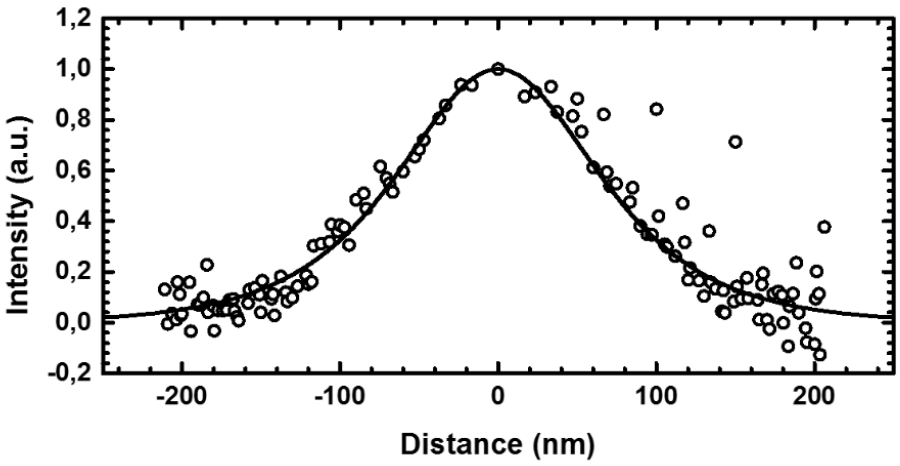

Figure 4.6.: Distribution of the average DW intensity profile for all the spin textures present in figure 4.5.a (unfilled circles) and its fit from equation 4.3 (black line). The position 0 represents the position of the skeleton.

The Gaussian function representing the electron beam distribution is determined using an edge of a particle in the SEMPA topography sum image calculated from the addition of the four electrons detectors at each position of the sample. The edge of the defect is assumed to be perfectly sharp modeled as a Heaviside step function to provide an

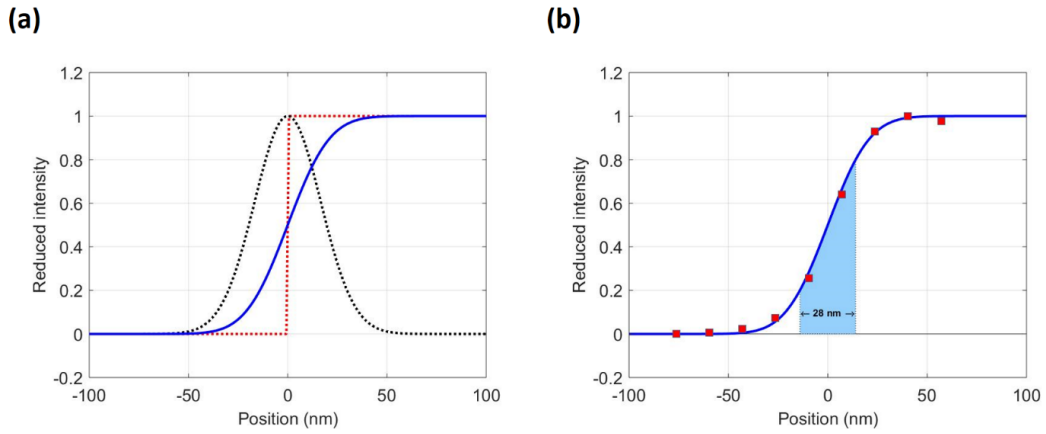

Figure 4.7.: (a) Simulated reduced edge profile of a perfect sharp defect imaged with SEMPA (blue) calculated from the convolution between a Heaviside step function (red) with a Gaussian function (black) following equation 4.3 using $\sigma = 17nm$. (b) Real reduced edge profile measured across a defect on a SEMPA image (red squares) with its best fitting edge profile function (blue). The light blue region represents the variation of the intensity between 20 % and 80 % showing the microscope resolution

upper limit on the resolution. Since the microscope may not be perfectly aligned and the measured electron beam has a finite size, we model the profile of the imaging as a Gaussian function. Finally, the measured edge defect profile is defined as:

$$Edge_{profile} \propto H(x) \bigotimes e^{-\frac{x^2}{2\sigma^2}} \tag{4.3}$$

where $H(x)$ represents the Heaviside step function and the Gaussian function represents the spread in the features arising from the imaging technique. In figure 4.7.a, the simulated reduced $Edge_{profile}$ (blue) is displayed for a particular $\sigma = 17\,nm$. In figure 4.7.a, the red square represent the real measured DW profile of a sharp particle where the fit using the "least squares regression" method is drawn with a blue line. For this particular image, one finds out that $\sigma = 17\,nm$ leading to the determination of the DW width. The spatial resolution is the interval corresponding to a variation of the intensity between 20% and 80% of a sharp edge [44]. We finally found that the resolution is about 28 nm at RT as seen in figure 4.7.b.
After determining the influence of the microscope on the imaging through the determination of σ, one can use the imaged DW profile and fit it with the $\mathbf{DW}_{profile}$ function in equation 4.3. This leads to the determination of the Bloch parameter Δ inducing a DW width $\delta_{real} = \pi\,\Delta\, = 275 \pm 5\,nm$.

4.4.2. Determination of the chirality

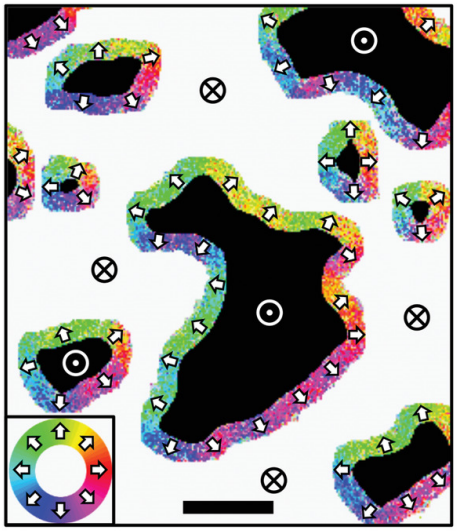

Figure 4.8.: The direction of the in-plane magnetization in the DW is displayed, as defined by the color wheel in the bottom left corner of the image. Scale bar: 1 µm.

After having defined the DW width, analysis of the spin distribution within the DW can be process. For that, one has extracted the magnitude and the direction of the in-plane magnetization M_x and M_y at each position of the DW displayed in figure 4.4.a-b which makes possible the deduction of the angle that corresponds to the direction of the in-plane magnetization inside the wall compared to the local tangent. Figure 4.8 displays the direction of the in-plane magnetization in the DW by way of the color wheel shown in the inset. Qualitatively, one can see that all the magnetic structures present the same chirality, namely they are homochiral clockwise Néel-type spin textures. For a precise analysis, comparison between the spin direction of each position inside the DW with the direction of the local tangent of the DW is plotted in figure 4.9. The histogram indicates that the magnetization direction in the DW structures forms a distribution centered around $-90°$. We conclude that our material exhibits a pure clockwise Néel-type homochiral character, which can be explained by the negative sign expected of the interfacial DMI especially at typical Fe/Pt and Co/Pt interfaces when the Pt layer is on top of the Fe or Co layer.

4.5. DMI as source of chirality

To ascertain that this chiral character is not a local effect at the surface but is indeed supported through the whole thickness of the film, asymmetric bubble expansion has been performed [98]. This technique relies on the asymmetric expansion of DW under

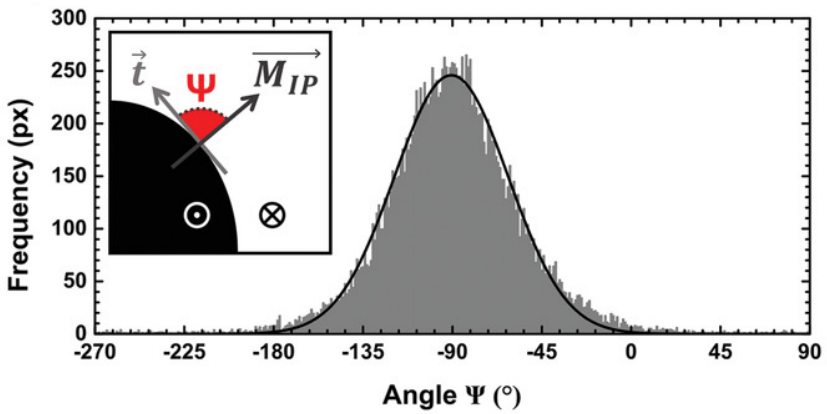

Figure 4.9.: Distribution of the direction of the in-plane magnetization in the DW with respect to the local tangent at RT: angle Ψ (see inset where a clockwise angle is defined as negative following the usual convention). A Gaussian fit indicates a central value around $-90°$.

IP magnetic field due to a symmetry breaking of the DW energy profile along the in-plane field direction. This means that a DW moves faster in the case of an alignment with the magnetic field than an antialignment. Conversely, magnetic spin textures with no preferential direction of the magnetization inside the DW through the whole thickness show symmetric bubble expension due to an identical DW energy profile at each position of the DW.
A magnetic bubble is stabilized using an OOP magnetic field of $H_z = 35\,Oe$ just below the depinning magnetic field where DW starts to expand. In figure 4.10, one can observe bubble expansion under different left IP magnetic field pulse from $100\,Oe$ to $600\,Oe$. It is clearly visible that the magnetic bubble expands faster on the left side that any other side meaning a left tendency of the IP magnetization inside the DW on the left of the magnetic bubble. Conversely, the right side of the magnetic bubble expanded slower than any other part of the spin texture meaning that the right part of the DW is antiparallel to the magnetic field direction. This confirms that the spin configuration of the DW is clockwise Néel through the whole thickness of the ferrimagnetic material meaning that the stabilization of the spin textures is due to a chiral interaction, namely the interfacial DMI.

4.6. Determination of the exchange stiffness and the DMI

- Exchange stiffness

Following equation 1.41, the DW width Δ in the intermediate thickness range depends on different material parameters, namely the exchange stiffness A, the effective anisotropy K_{eff}, the uniaxial anisotropy K_u, the saturation magnetization

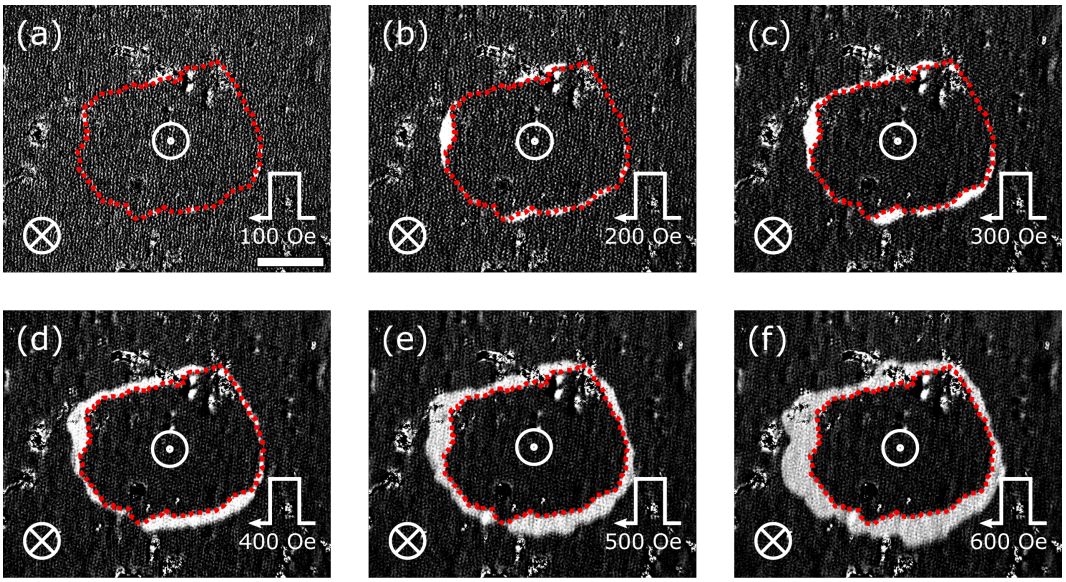

Figure 4.10.: Asymmetric expansion of up-magnetized bubble (white areas) using a constant OOP magnetic field of $H_z = +35\,Oe$ while applying one left IP magnetic field pulse of different strength. Red dots indicate the outline of the up-magnetized bubble stabilized without IP magnetic field. Scale bar in (a): 20 µm.

M_s, the thickness of the magnetic materials d and the angle ψ such as $\Delta = f(A, K_{eff}, K_u, M_s, d, \psi)$. The thickness of the ferrimagnetic material has been chosen and verify using X-ray reflectometry (XRR) as seen in Appendix D while the angle ψ has already been determined experimentally being equal to $-90°$. Also, one can easily measure the saturation magnetization as well as the effective anisotropy K_{eff} using SQUID where the latest is defined as the difference in the areas of the IP and out-of plane hysteresis loops equal to $K_u - \mu_0 M_s^2$. Therefore, one can deduct the exchange stiffness A through the measurement of the DW wifth Δ measured using SEMPA imaging. For this system, one has extract numerically the value of the exchange stiffness being equal to:

$$A = 8.0 \pm 0.5 pJ.m^{-1} \tag{4.4}$$

which is comparable to other GdFeCo ferrimagetic alloys.

- DMI

The strength of the total DMI is not easy to determine experimentally which is mostly done by Brillouin light scattering [99] [99] [100] [101]. However, from equation 1.43, one can determine the value of the DMI threshold D_{thr}, minimum value leading to a pure Néel-type homochirality character. This is possible here through the sureness of

having pure clockwise Néel spin textures. This leads to a total DMI threshold value of:

$$D_{thr} = 0,025 \pm 0,002\, mJ.m^{-2} \tag{4.5}$$

The DMI threshold value DMI_{thr} to force pure Néel homochirality is two order of magnitude smaller than the value arising at the Fe/Pt or Co/Pt interfaces. This is principally due to a reduced saturation magnetization in ferrimagnetic materials. Therefore, Néel-type spin textures in ferrimagnetic materials arising from interfacial DMI are relatively easy to access. This value is in the same order of magnitude than bulk DMI present naturally in ferrimagnetic material due to an asymmetric distribution of the elemental content leading. This bulk DMI is different in geometry than the ones present in crystals (see section 1.2.4) leading to Néel chirality.

4.7. Study in temperature

One crucial point for the use of magnetic skyrmions in spintronic devices is the conservation of the homochiral character of the DW over a large temperature range. Since a stray field favors Bloch-type DW, the observation of pure Néel-type DW observed at RT where the saturation magnetization is high allow to expect the stabilization of pure Néel-type spin textures at all other temperatures where the saturation magnetization is lower (see figure 4.2). To assess this, the previous analysis has been carried out from 26 to 315 K where the pure Néel character effectively remains for this temperature range. Next, we analyze the DW width for these temperatures, with the different values reported in Figure 3b. We find that the DW are narrower when the temperature is decreased due to the increase of the effective anisotropy that is confirmed by SQUID. The results can be analyzed with the help of measurements of the thermal variation of K_eff and M_s at different temperatures. As expected for the CoFe transition metal dominant ferrimagnet, lower temperatures lead to a reduction in the saturation magnetization since the rare earth sublattice magnetization increases faster than the transition metal one. On the other hand, K_{eff} increases when the temperature decreases. Since the chiral character is kept over the whole temperature range where $\psi = 90°$, equation 1.41 can be used to extract the thermal variation of the exchange stiffness of the ferrimagnetic alloy over the whole temperature range. The exchange stiffness is found to be mostly constant, with a slight increase when the temperature increases, as shown in figure 4.11.
This dependence of the exchange stiffness on temperature is different than in ferromagnetic materials where:

$$\frac{A(T)}{A(0)} \propto \left(\frac{M(T)}{M(0)}\right)^{\gamma} \tag{4.6}$$

where γ is around 2 [102] [103]. Considering that in ferrimagnets the magnon spectrum consists of acoustic and optical branches, Nakamura et al. have shown that the temperature dependence of A(T) is rather weak up to a certain high temperature [104]. This is due to the competing effects of thermal-acoustic and optical magnons.

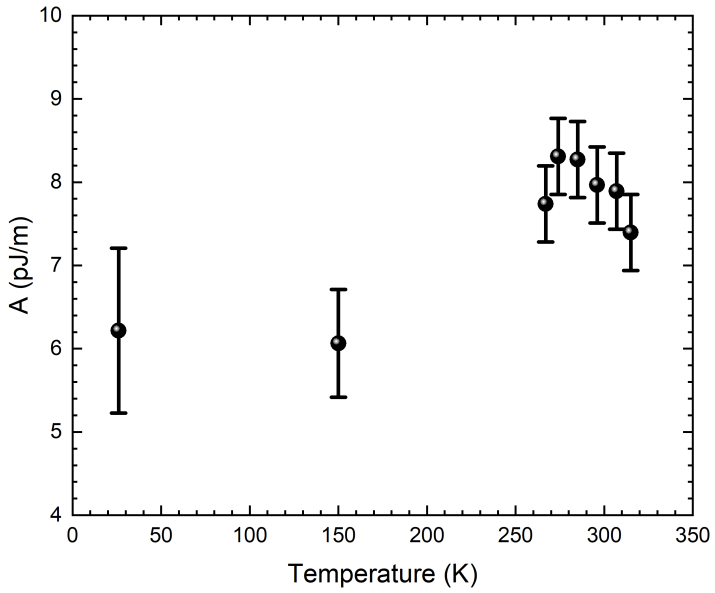

Figure 4.11.: (a) Measurements of the DW width and (b) determination of the exchange stiffness of the ferrimagnetic multilayer.

4.8. Ferrimagnetic skyrmionium

As explained in section 4.3, an IP magnetic field is used to nucleate spin textures that start to propagate at random positions. Remarkably, using an IP oscillating magnetic field with a certain damping ratio allows for the nucleation of a spin texture inside another spin texture that has been nucleated previously. In figure 4.12.a-b, one can observe a small 160 nm diameter skyrmion stabilized in a larger skyrmion bubble, forming a ferrimagnetic skyrmionium as described in section 1.3.4. We here apply the topology definition that identifies skyrmions from the topology of the spin structure independent of their size.

4.9. Conclusion

In this chapter, the imaging of the internal spin structure of DW in ferrimagnetic alloys through a residual Pt capping layer using SEMPA has been done for the first time. This approach is a new path to characterize chiral spin textures in ferrimagnetic multilayers. In the studied GdFeCo-based ferrimagnet, we find that the DW spin textures exhibit a pure Néel-type homochirality that is preserved over a large temperature range, even far away from the compensation temperature. This makes GdFeCo a potentially attractive material for skyrmion-based spintronic technologies.

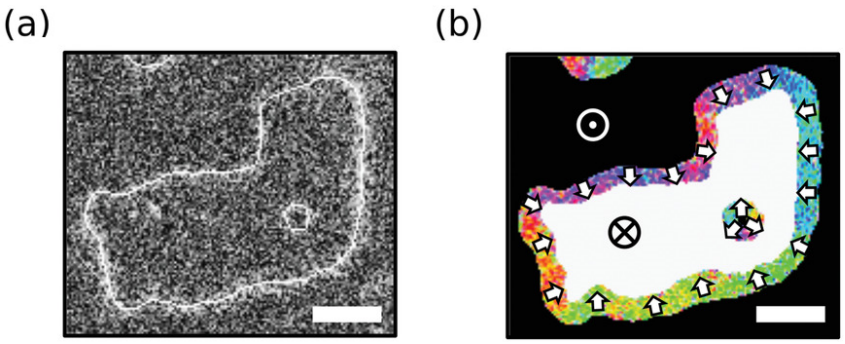

Figure 4.12.: Determination of the magnetization direction inside the DW of a ferrimagnetic skyrmionium. (a) Absolute in-plane magnetization intensity with the DW skeleton displayed in white and (b) direction of the in-plane magnetization in the DW of a ferrimagnetic skyrmionium at 320 K. Scale bars in (c) and (d): 500 nm.

The corrected values of the DW width obtained from the high resolution imaging allow then to extract the exchange stiffness in this material. Finally, the first direct observation of pure Néel-type skyrmionium in ferrimagnetic materials has been reported which has the advantage of possessing zero net topological charge at all temperatures. This makes the material potentially highly useful for skyrmionic devices where the skyrmion Hall angle could be avoided.

5. Current-induced dynamics of magnetic skyrmions in ferrimagnets

Using ferrimagnetic materials for future skyrmion-based technologies implies the control of skyrmions dynamics in a deterministic manner. To do that, SOT have been proposed and realized in different studies [64] [22] where a reduced skyrmion Hall angle has been observed in GdFeCo ferrimagnet of circa 30° [69]. However, the multirepetition of ferrimagnetic layers makes impossible to perform dynamics at reduced magnetization where the coupling between each layer is lost. Furthermore, 5nm-thick ferrimagnetic layer is a too thick to make the SOT perfectly efficient since the reported values of spin diffusion length do not exceed few nm for most of the TM materials [105]. Also, displacing thicker material is obviously more difficult that thinner one since it possesses more magnetic moments. Therefore, this chapter will focus on other solutions that one can imagine to avoid these problems and open new paths of reflexion on the dynamics of magnetic skyrmions.

5.1. Imaging techniques for skyrmions dynamics

Due to their small size, magnetic skyrmions should be observed with high resolution imaging techniques such as SEMPA, MFM or STXM. As seen in the previous chapters, SEMPA is a powerfull imaging technique but is limited in a sense that it allows to image through small capping layer (maximum of 1 or 2 nm for most of the HM) making the material engineering more complicated. Also and probably the most challenging issue, the time needed to image ferrimagnetic alloys using SEMPA is too long (about 20 hours per image) implying carbonization of the sample to start and makes multi-imaging at the same position impossible. Concerning the MFM, the nucleation and deformation of magnetic skyrmions is possible with the magnetic tip used in the technique (see Appendix C) which makes this technique not reliable for skyrmion imaging [77]. For all these reasons, fast imaging and not perturbing technique is favored such as STXM which will be used in the rest of the chapter.

5.2. GdFeCo: single layer of ferrimagnetic materials

5.2.1. Samples engineering

Several considerations has to be taken into account for the development of ferrimagnetic materials used for skyrmion displacement. Let's review here the main important ones.

- Choice of material

Here, one wants to continue with GdFeCo-based ferrimagnet since the material has been well studied where remarkable properties has been found such as the all-optical switching of the magnetization using laser pulses [106] [107], the fast DW motion [108] or the reduced skyrmion Hall angle [69]. Also, in order to make possible the imaging closed to the compensation magnetization temperature, single GdFeCo-based ferrimagnetic alloy has been developped.

- Choice of interfaces

The choice of interfaces is particlarly difficult since the interfaces play a role in different phenomenons. One studies here the displacement of spin textures using SOT. Therefore, it is important to choose two interfaces that will act efficently and together on spin textures. One of the most known one is Ta and Pt. Indeed, Ta interface possesses a negative spin Hall angle while Pt got a positive one [109] [110]. By way of symmetry, the Ta being on the other side of the material, both SOT should act together.

Secondly, following R. Tomasello *et al.*, SOT are particlarly efficient on Néel-type spin textures [85]. Therefore, interfaces with a strong interfacial DMI should be used to generate this type of spin textures. In the previous discussed case, Pt possesses a strong and positive DMI for Co and Fe atoms [5] [96] [97] while no information have been seen so far in the litterature concerning the DMI with RE elements. Regarding the Ta, it generates a small and positive DMI. The DMI at the Ta interface is negligible compared to the high DMI value with Pt elements and finally, a resulting positive DMI should be present leading to an anticlockwise chirality of the spin textures.

- Buffer layer of Pt layer

A. Belabbes *et al.* have calculated that the DMI strength at the Pt/Co and Pt/Fe interfaces are especially strong and depend on the crystallographic ordering of the Pt layer where an enhancement have been calculated for Pt(111) [5]. Therefore, Pt is grown on Ta where Pt grows on dense plan on top of it. Also, an ultrathin layer of pure Co is inserted between the Pt and the ferrimagnetic layer to get a strong DMI avoiding RE elements at the interface.

- Thickness of the ferrimagnetic layer

The thickness of the ferrimagnetic layer should be as small as possible in order to make the SOT more efficient. However, this thickness is limited by the imaging techniques used, i.e. the STXM. This is an element sensitive technique able to image from 1 nm thick of pure Co [26]. However, the Co layer here possesses a crystalline structure implying an identical environnment for all the Co atoms. This has for consequence of having an energy absorption peak strongly localised. Therefore, after tuning the

photon energy of the X-ray beam to the peak, most of the atoms of the desired element should interact with the photons. This is not the case for GdFeCo-based ferrimagnetic alloys where the environment of an atom is mainly random making the absorption edge peak relatively large and smaller. Therefore, thicker GdFeCo layer than the Co one used in the mentionned reference should be used. It is rather difficult to estimate excatly which thickness it should be since synchrotron shifts are not easy to obtain. From that, one has decided to deposite GdFeCo-based ferrimagnet of several thicknesses from 3 to 5 nm.

- Enhancement of the OOP anisotropy

GdFeCo possess a small volume anisotropy leading in a difficult way of having OOP anisotropy below 5 nm of the GdFeCo layer. To artificially enhance the OOP anisotropy, an ultrathin Cu layer can be added at the interface with the ferrimagnetic material. Cu has a large spin diffusion length [111] and therefore should not have a sizable influence on the spin current. Thus, the Cu layer should not affect the SOT efficiency.

- Composition

To make the imaging as easy as possible, small anisotropy sample has been developed to obtain spin textures at zero magnetic field. This is probably the safest way of imaging thin samples in the lowest thickness limit. One has chosen the samples to be TM dominant to make possible to go closer to the magnetization compensation temperature by cooling down, equipment available usually in STXM beamline stations. Also, this means a reinforcement of the presence of Fe atoms, element that will be used to observe magnetic patterns.

- Capping layer

A small Pt capping layer of 1 nm has been used to protect the oxydation of the Ta layer which is known to be oxydable down to 5 nm.

Sample type: $Si/Si_3N_4//Ta/Pt/Co/GdFeCo/Cu/Ta/Pt$

5.2.2. Samples properties

Bunch of samples have been prepared closed to the SRT for different thicknesses with the following compositions:
— Sample 2: $Si/Si_3N_4//Ta_5/Pt_5/Co_{0.3}/[Gd_{28.3}FeCo]_3/Cu_1/Ta_5/Pt_1$
— Sample 3: $Si/Si_3N_4//Ta_5/Pt_5/Co_{0.3}/[Gd_{26.9}FeCo]_4/Cu_1/Ta_5/Pt_1$
— Sample 4: $Si/Si_3N_4//Ta_5/Pt_5/Co_{0.3}/[Gd_{24.5}FeCo]_5/Cu_1/Ta_5/Pt_1$

In figure 5.3, one can observe their hysteresis loop in OOP geometry. Once again, the sense of these loops indicates a TM dominant behaviors by looking at the

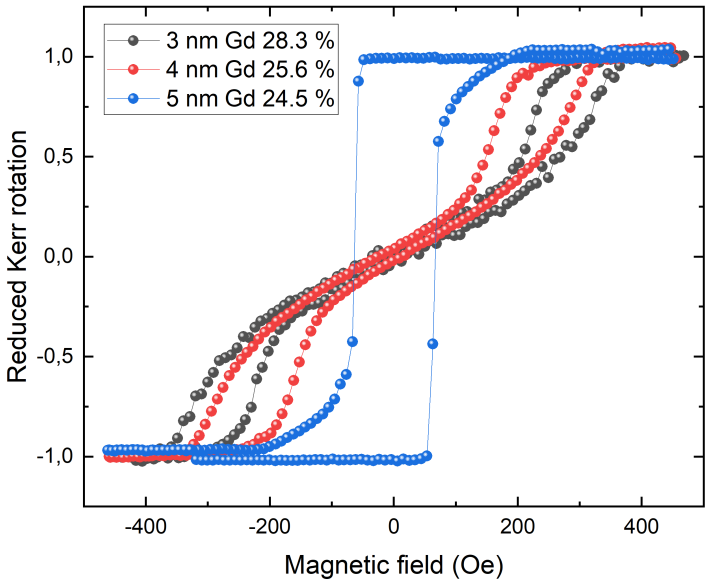

Figure 5.1.: Kerr rotation measured with MOKE on samples 2, 3 and 4 at RT.

second harmonic signal which was compared to a pure TM reference sample with OOP geometry as explained in section 2.3.2. The sample stoechiometry is relatively different for each sample. This can be explained by a gradient of composition along the thickness in ferrimagnetic alloys, resulting in an accumulation of Gd atoms at the Cu edge where a dead layer is supposed to be here. This is especially important for really thin samples as the ones studied here. To compensate this effect for ultrathin samples, an addition of RE atoms is then necessary to obtain the desired composition in the alloy.

5.2.3. STXM imaging of single layer of ferrimagnet

To perform current-induced dynamics of magnetic spin textures, samples has been patterned into wires with different widths where a gold pad is present on each side of the wire to allow current pulses injection (see Appendix E). L_3-edge of the cobalt has been used to image the magnetic pattern of the sample. We first start with the sample 4, thicker sample with XMCD imaging which should be easier than samples 2 and 3 due to an enhancement of the presence of the Co atoms. After saturation of the sample, a magnetic field of 10 mT has been applied where the presence of spin textures has been made obvious from the hysteresis loop in figure 5.1. As seen in figure 5.2.a, magnetic spin textures are present such as domain stripes and magnetic bubbles of

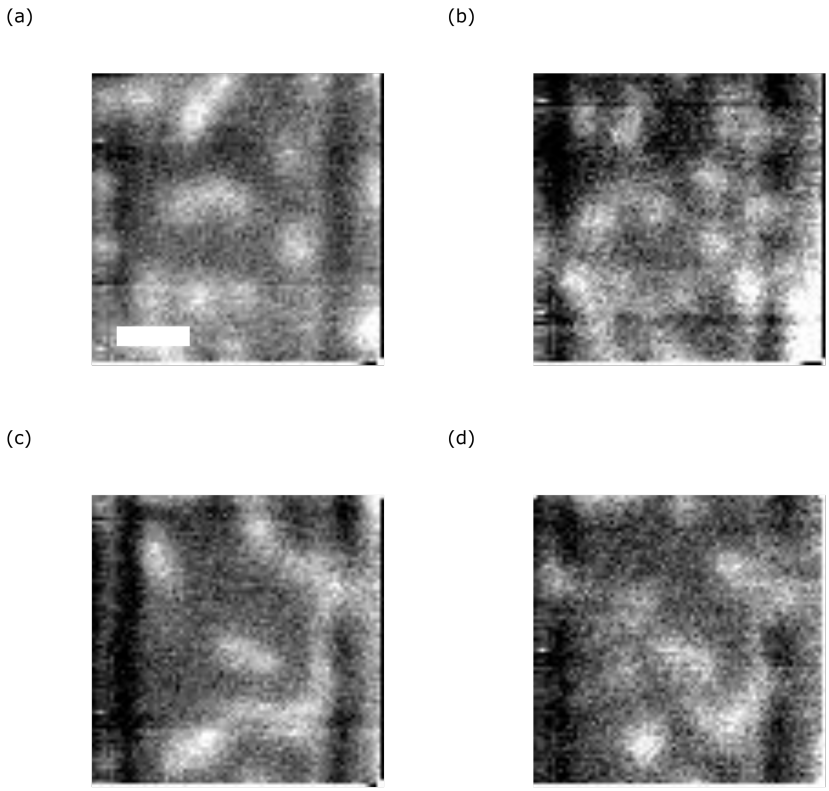

Figure 5.2.: STXM imaging of the 5 µm width patterned wire of sample 4. Sample has been saturated before reaching a state where magnetic bubbles are present at 10 mT where image (a) has been taken. Afterwards, 1 pulse of $4.10^{11} A.m^{-2}$ for a duration of 10 ns has been applied to get image (b), then image (c) and finally image (d). Scale bar in (a): 500nm.

circa 200 nm width. One current pulse of 10 ns between each image has been applied to get the figure 5.2.b-d modifying the magnetic structures. This modification seems to be randomly distributed, probably originating from the heat arising from the current pulse. Unfortunately, the contrast is really bad even if the dwell time was as large as 50 ms per pixel for an image of 2x2 µm² and 100*100 pixels. This results in a total acquisition time for a XMCD image of circa 15 min. This is definitely too long to perform current-induced dynamics of spin textures, experiment needing hundred to thousands of images. Also, samples 2 and 3 have been tried displaying a contrast worst than the sample 4. Therefore, one has to find another approach if STXM is used.

5.3. CoDy: multirepetition layers of ferrimagnetic materials

Another method would be to use multirepetition of ferrimagnetic layers instead of single one. As seen earlier, this will then make impossible the total annihilation of the skyrmion Hall angle since the coupling between each individual ferrimagnetic layer should be lost at the angular momentum compensation (generally closed to the magnetization compensation temperature) 1.5. However, one can imagine another type of materials to improve the skyrmion dynamics. To do that, one could use material with larger volume anisotropy making possible to get a thinner OOP magnetic material leading to more efficient dynamics via SOT.

5.3.1. Samples engineering

- Choice of material

Dy is a RE element that possesses a strong volume anisotropya helping for the OOP anisotropy. Here, one has proposed to study the dynamics behaviors of CoDy-based ferrimagnet. Indeed, K. Chen *et al.* have already seen magnetic skyrmions in thick $DyCo_3$ ferrimagnetic material [112].

- Choice of interfaces

The two interfaces that will act efficently and together on Co atoms via SOT are the Ta and Pt as seen in section 5.2.1. Also, this couple generates a sizable interfacial DMI favoring Néel-type spin textures.

- Thickness of the ferrimagnetic layer

The thickness of the ferrimagnetic layer should be as small as possible in order to make the SOT more efficient. Contrary to single magnetic materials, this will not limit the imaging technique since one can get enough materials by increasing the number of repetitions of the multilayer stack.

- Composition

With the use of multirepetition stacks, samples should be quite far from the magnetization compensation temperature closed to the SRT where the anisotropy is as small as possible. Indeed, skyrmions are here stabilized with the help of the stray field which plays a major role when the other energies are smaller.

Sample type: $Si/Si_3N_4//[Ta/CoDy/Pt]_N$

5.3.2. Samples properties

In this section, one has prepared one sample for the study of skyrmion dynamics using STXM with the following composition:

— Sample 5: $Si/Si_3N_4//[Ta_3/(Co_{79.1}Dy_{20.9})_{2.5}/Pt_3]_9$

In figure 5.3, one can observe the hysteresis loop in OOP geometry of the sample 5 on membrane before and after the patterning process. This hysteresis loops are a bit different from the ones acquired on the films (see Appendix A). One can confirm that the sample is TM dominant by looking at the second harmonic signal as explained previously. As seen in the sample 5 composition, strongly unbalanced stoechiometry is present for Co elements due to the large magnetic moment carrying by Dy elements. To make the coupling between each ferrimagnetic layer through stray field possible, the monolayer $Si/Si_3N_4//[Ta_3/(Co_{79.1}Dy_{20.9})_{2.5}/Pt_3]$ has been prepared with a small OOP anisotropy closed to the SRT where the relevant multilayer is the sample 5.

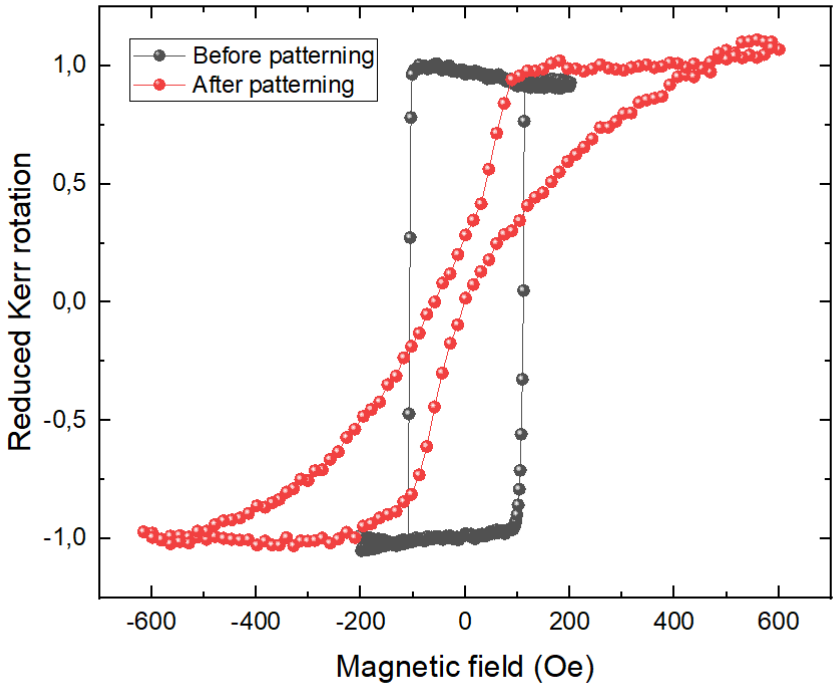

Figure 5.3.: Kerr rotation measured with MOKE on sample 5 before and after patterning at RT.

As seen in Appendix B, the patterning process involves a baking process which is in-

evitable to get a dry resist, necessary step to well patterned a sample. However, newly deposited ferrimagnetic samples are especially sensitive to heat as seen in Appendix A. Here, one supposes that the elements of the ferrimagnetic material have still not reached their equilibrium where the process can be accelerated with heat. Therefore, the first deposited material was more OOP than desired to take into account the post-process in prevision of the patterning. At the end, one has obtained a sample where the hysteresis loop indicates regions with supposed different magnetic patterns such as skyrmions or stripes accessible with reasonable magnetic flux density.

5.3.3. STXM imaging of multirepetition layers of ferrimagnet

Sample 5 has been patterned into wires where two gold contacts have been deposited at each extremity of them using for the two EBL steps positive resists as seen in Appendix E. Wires have been imaged using STXM at the L_3-edge of the cobalt due to the amount of this element in this material. Good contrast has been observed even for single helicity imaging (no XMCD contrast) with small dwell time which makes possible to acquire a reasonable amount of data for current-induced skyrmion dynamics statistics.

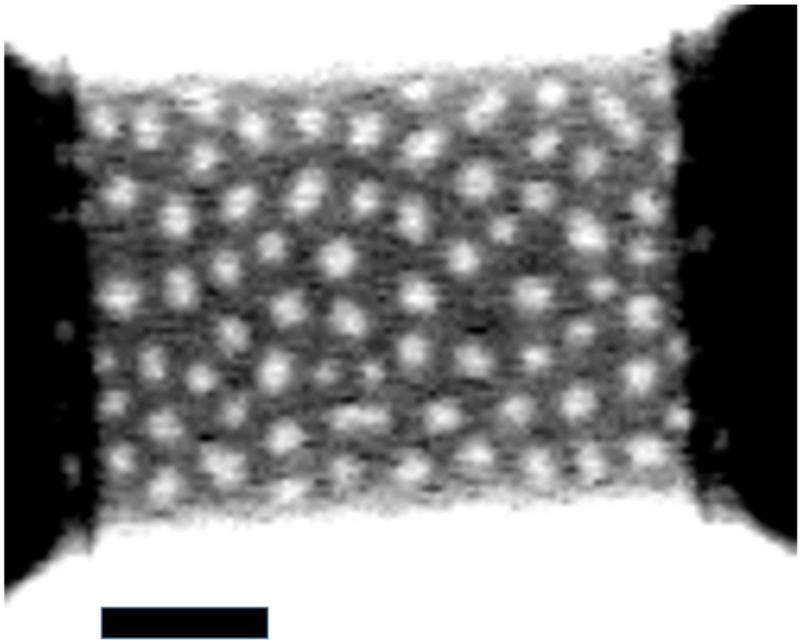

Figure 5.4.: STXM image of sample 5 at 320 K and 10 mT. Scale bar: 1 µm.

In figure 5.4, an exemple of a STXM image of sample 5 at 320 K and 10 mT is displayed making in evidence well-defined individual spin textures of circa 200 nm diameter into the wire. White contrast indicates domains pointing up (directed to the reader) while

dark contrasts are pointing in the opposite direction. The spin textures are uniformly distributed in the wire. Therefore, one can expect homogeneous magnetic properties in the material. On the side of the wire, one can observe gold contacts in black deposited directly on the wire.

5.3.4. Deterministic dynamics of magnetic skyrmion via SOT

The setup in synchrotron facility allows to send current pulses down to few ns as well as controling the temperature and magnetic fields in OOP geometry. Here, one has acquired images with high density of spin textures such as in figure 5.4. Afterwards, one applied a 10 ns length electrical pulse, acquired one other STXM image and repeat the process to get a video. One can therefore track the spin textures using the *trackpy* package to observe how the spin textures are responding to the current pulses for different current densities [113].

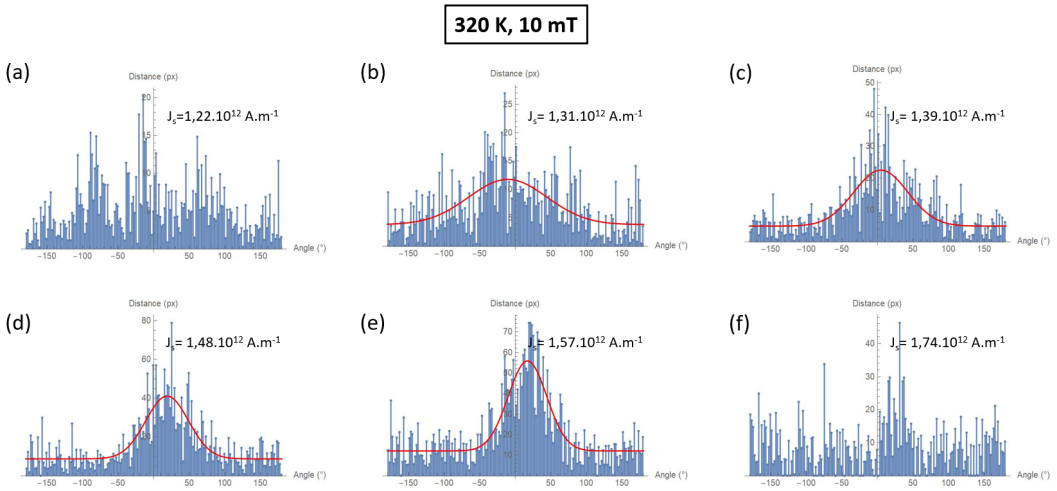

Figure 5.5.: Distribution of the traveled distance of all magnetic skyrmions in sample 5 regarding the skyrmion Hall angle at 320 K and 10 mT for different current densities. 1 px = 40 nm.

In figure 5.5, one has plotted the total distance traveled by all tracked spin texures as a function of the skyrmion Hall angle at 320 K and 10 mT. This angle is defined between the direction of propagation of the spin textures and the direction of the applied current, supposed linear with the wire. Here, choosing the total distance makes sense since it counts with more importance the textures that are moving further than the pinned ones. Current densities between $1.22 * 10^{12} A.m^2$ and $1.74 * 10^{12} A.m^2$ have been especially observed. Below these values, spin textures are not moving at all and above it, they are moving arbitrarily making in evidence brownian motion coming from thermal activation. To study deterministics dynamics, one has prefered to study below the thermal regimé where thermal activation are especially strong to avoid

noises as much as possible in the signal and to facilitate the tracking. Gaussian fitting curves have been used to the different histograms in order to determine a particular direction of propagation of the circular spin textures (skyrmion Hall angle) as well as determining its standard deviation. In figure 5.4a,f, it seems that there is no particlar direction of propagation for $1.22*10^{12} A.m^2$ as well as for $1.74*10^{12} A.m^2$. These cases represent the extremes limits of the flow regime, namely the "creep" and "thermal" regimes respectively. In the flow regime, fitting curves have been displayed in red as seen in figure 5.4b-e. One can observe that these gaussians seem to be narrower and higher when the current density is increasing meaning a more precise angle defined with less dispersion. One can can conclude that there is a deterministic motion of the spin textures leading to the certitude of having one unique chiality for the circular spin textures. Therefore, these circular spin textures can be defined as magnetic skyrmions.

The detected skyrmion Hall angle depends clearly on the value of the current density and seems to increased while increasing the current density. So, in figure 5.6, one has plotted the skyrmion Hall angle of sample 5 regarding the applied current density at 300 K and 320 K for different magnetic fields.

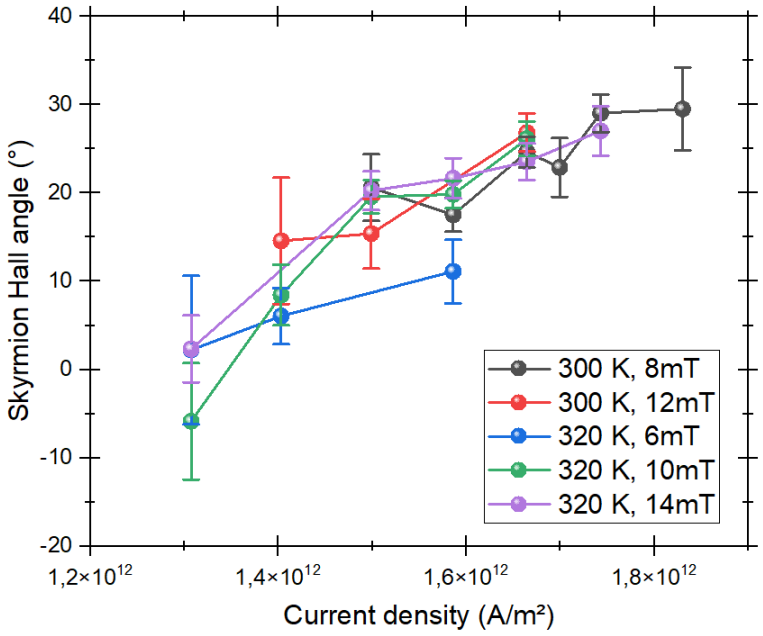

Figure 5.6.: Skyrmion Hall angle of sample 5 regarding the applied current density at 300 K and 320 K for different magnetic fields.

For all the cases, the skyrmion Hall angle started around 0 and tends to a limit value of circa 25°. This is a reduced value compared to other magnetic skyrmions observed in ferromagnetic materials [24] [25]. This kind of behavior is representative from

materials with a large amount of pinning site [114].

5.3.5. Skyrmions velocities

For the different temperatures and magnetic fields studied in the previous section, one has determined the skyrmion velocity at different current densities. To do that, one has analyzed the magnetic skyrmions detected closed to the skyrmion Hall angle ($\Theta_{SHa} \pm \sigma$). Indeed, these skyrmions are representatives from the flow motion. Pinned skyrmions have also been excluded from the analysis.

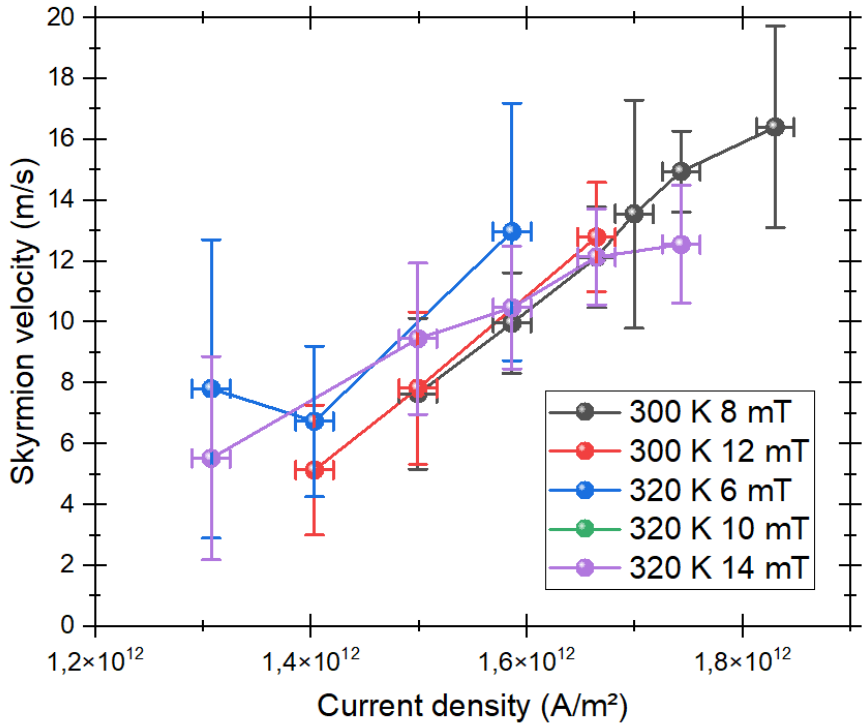

Figure 5.7.: Skyrmion velocity of sample 5 regarding the applied current density at 300 K and 320 K for different magnetic fields.

In figure 5.7, the skyrmion velocity seems to be linear with the applied current. The maximum skyrmion velocity has been obtained for a current density of $1.8310^{12} \pm 0.0210^{12}\, A.m^{-2}$ which is: $16.4 \pm 3.3\, m.s^{-1}$.

5.4. Conclusion

In this chapter, one has studied skyrmions in multirepetition of CoDy-based ferrimagnet. This is the first time that ferrimagnetic skyrmions have been observed in thin films in this type of materials. Here, it was possible to observe a collective motion

of magnetic skyrmions leading to a precised skyrmion Hall angle for different current densities. This angle started closed to 0° for small current densities and ended to a reduced value compared to ferromagnetic materials closed to 25° at higher current density. Also, the skyrmion velocity was measured and was linear with the applied current in the flow regime. In this material, skyrmion velocities up to $16.4 \pm 3.3 m.s^{-1}$ was measured.

6. General conclusion and outlook

In this thesis, we first focus on the imaging of chiral spin textures in GdFeCo-based ferrimagnet using SEMPA which allows the measurement of the IP direction of the magnetization. We here image the direction of the magnetization inside the DW of numerous spin textures including a ferrimagnetic skyrmionium. Our measurement shows that all the spin textures present in our material display a pure right-hand Néel-type character from a large temperature range due to a strong enough DMI. This is an essential step for the implementation of small spin textures such as magnetic skyrmions in spintronic devices since the stabilization of the chiral character leads to a homogeneity in the dynamics via SOT especially efficient for Néel-type particles. Moreover, it is important to highligh that this was the first imaging reported of the DW in ferrimagnetic materials using this technique. This makes this technique suitable for the study of spin textures in ferrimagnetic materials in laboratory. Also, the high spatial resolution of SEMPA allows us to measure the DW width with a high precision. We then conclude than the measured DW were relatively large compared to other materials. This is in agreement with the small anisotropy measured in our material. The measurement of the DW width alongside with the chiral character and other magnetic parameters, we deduct the exchange stiffness, parameter which is not easy to determine. Our conclusion points out that SEMPA is a technique that can be used to determine the chiral character of spin textures with a small capping layer that does not exceed 1 to 2 nm. Also, if the DW width is large enough, one can measure them and deduct a value of the exchange stiffness.
Secondly, we investigate the current-induced motion of magnetic skyrmions via SOT in CoDy-based ferrimagnet. Here, we detect a general motion of the spin textures in a precise direction which is not collinear with the applied current. This means that all the spin textures have the same chirality which arises from a sizable DMI. The spin textures diplayed a skyrmion Hall angle that is smaller than previous studies. This skyrmion Hall angle increases with the current density till it reaches its limit. Unfortunately, the speed of these skyrmions is slow probably arising from a large amount of pinning sites in our material. The speed measured increases linearly with the current density which is in accordance with the theory.

Part III.

Appendices

A. Effects of time and heat on ferrimagnetic materials

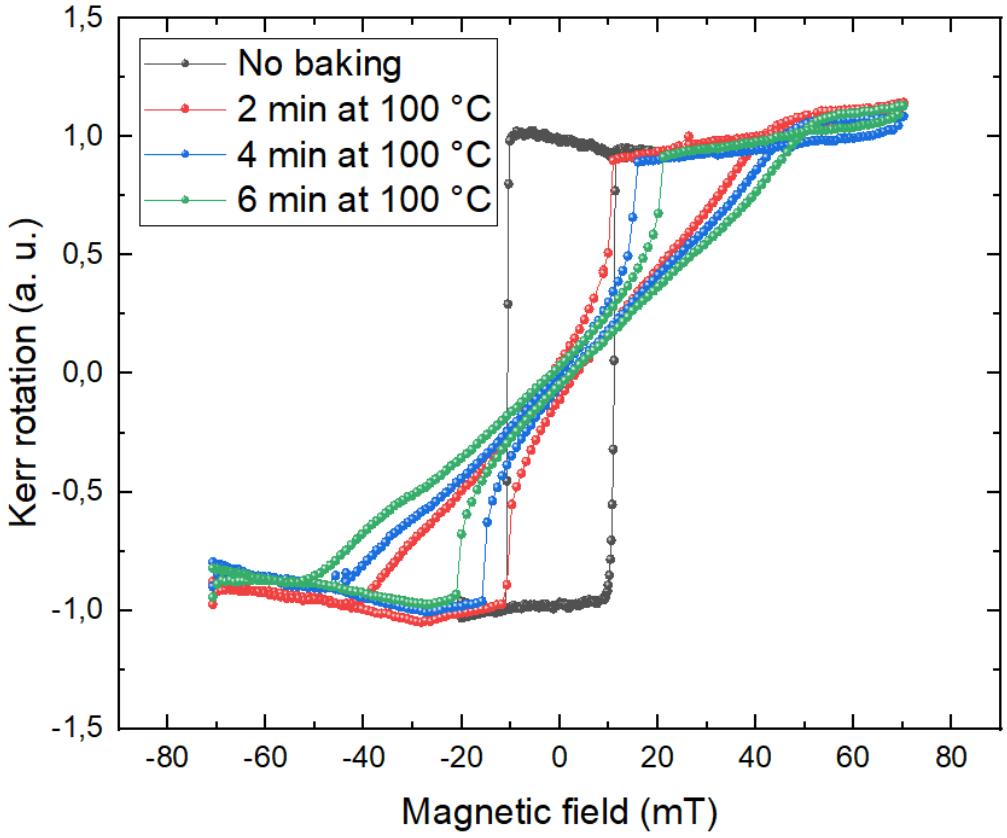

Figure A.1.: Hysteresis loop of ferrimagnetic material $Si/Si_3N_4//[Ta_3/(Co_{79.1}Dy_{20.9})_{2.5}/Pt_3]_9$ measured on the films for different baking time at 100 °C.

In ferrimagnetic materials, there is a gradient of stoechiometry in the thickness of the material. Right after the deposition of the material using PVD, the migration of RE elements has still not been accomplished. This migration takes time and can be accelerated using baking processes. This could be an issue for patterned samples since baking processes are involved to dry the MMA and PMMA resists. Therefore, it could be interesting to bake the samples on film to see how the magnetic behaviors

are impacted by the heat. In figure A.1, one has plotted hysteresis loops of the ferrimagnetic material $Si/Si_3N_4//[Ta_3/(Co_{79.1}Dy_{20.9})_{2.5}/Pt_3]_9$ studied in chapter 5 for different baking time at 100 °C: 2', 4' and 6'. Here, one can see after 2' of baking a semblance of stabilisation where "butterfly" hysteresis loop is then present showing the presence of magnetic spin textures easily stabilized using magnetic fields. In order to overcome the problem of migration and to dry enough the resist to be used in EBL processes, one has chosen for all the receipts to bake the resists for 5' as seen in Appendix B.

B. EBL recipies

- Sample cleaning:
  - Ultrasonic cleaning[1] with acetone for 60”
  - Ultrasonic cleaning with isopropanol for 60”
  - Ultrasonic cleaning with distilled water for 60”
  - Drying sample using a N_2 gun
  - Baking: $T = 100\ °C$ for 120” to desorb water

- Resist coating:
  - MMA (8.5) MAA EL6: 0.1 ml
  - spin-coating
    - pre-spin: 500 rpm for 2”
    - spin: 3000 rpm for 60”
  - Baking: $T = 100\ °C$ for 300” to dry softly the MMA resist
  - Sample cooling down for 120” at air

  - PMMA 950k A4: 0.1 ml
  - spin-coating
    - pre-spin: 500 rpm for 2”
    - spin: 3000 rpm for 45”
  - Baking: $T = 100\ °C$ for 300” to dry softly the PMMA resist
  - Sample cooling down for 120” at air

- Exposure parameters of the electron beam lithography:
  - EHT voltage: 10kV
  - Aperture: 30 µm for wires and 60 µm for Au contact pads
  - Working distance: 9 mm
  - Dose: 160 $\mu C.cm^{-2}$

[1] Ultrasonic cleaning is not used on membranes

- Development:
  - Resist developer for 30" (MIBK (3/4) + Isopropanol (1/4))
  - Development break: isopropanol for 30"
  - Drying sample using a N_2 gun

- Materials deposition on patterned geometries

- Resist removal:
  - Sample is placed in acetone for 12 h
  - The resist is removed using a pipette.
  - Ultrasonic cleaning with isopropanol for 60"
  - Ultrasonic cleaning with distilled water for 60"
  - Drying sample using a N_2 gun

C. Skyrmion nucleation by magnetic field gradient

A $Si/SiO_2//[Ta(3)/Co_{76}Dy_{24}(1.7)/Pt(3)]_9$ sample possessing a TM dominant sublattice can stabilize OOP magnetic skyrmion at different magnetic fields as seen in the hysteresis loop in figure C.1.

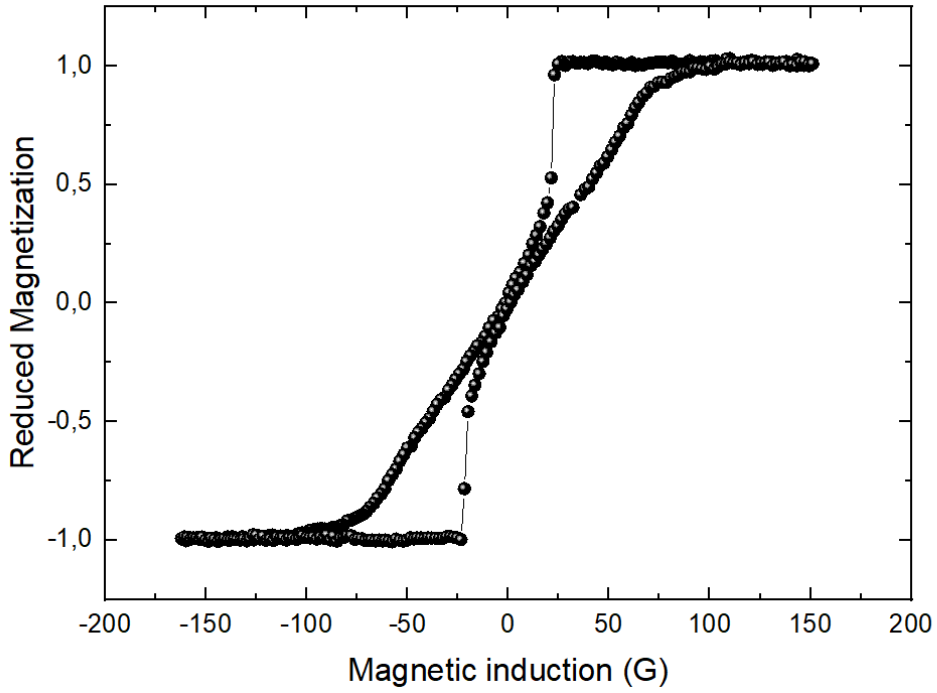

Figure C.1.: Hysteresis loop of $Si/SiO_2//[Ta(3)/Co_{76}Dy_{24}(1.7)/Pt(3)]_9$ ferrimagnetic sample.

Here, one can see that magnetic domains should be stabilized at 0 magnetic field. To verify that, AFM/MFM has been performed on the sample after demagnetization of the sample. In figure C.2a, one can observe the topographic image where the RMS roughness is egal to 0.15 nm showing a relatively smooth surface. In figure C.2b, the image represents the MFM image where the contrast displays the two opposite direction of the OOP magnetization in the vertical direction **z**. Here, one can see magnetic domains in labyrinth. To know the size of these domains, one has perform a FFT (fast Fourier transform) that gives us the periodicity of

the magnetic domains which is egual to 746 nm. After scanning a first time the sample, one has scanned the sample a second time at the same position to see if the magnetic tip has affected the domains configuration. In figure C.2c, the image represents the second MFM scan over the same position. Here, magnetic domains have been replaced by small magnetic bubbles of circa 230 nm diameter. This shows that the magnetic field gradient arising from the magnetic tip disturbs the initial magnetic configuration where other metastable states can then be stabilized.

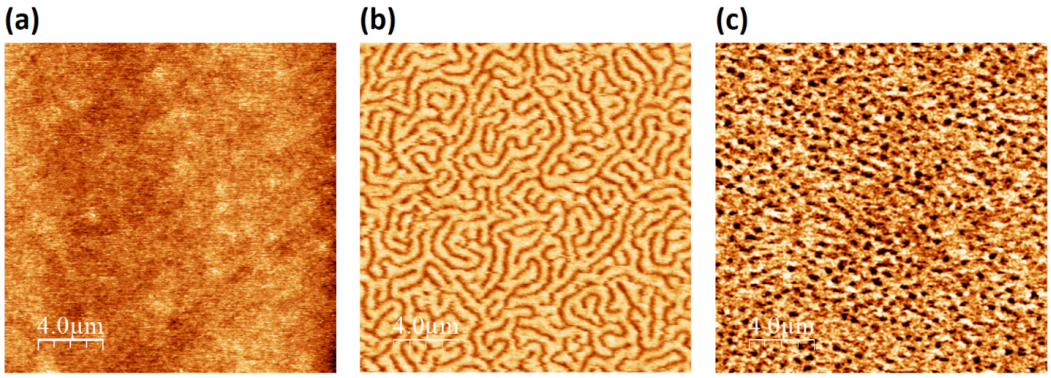

Figure C.2.: AFM/MFM imaging of $Si/SiO_2//[Ta(3)/Co_{76}Dy_{24}(1.7)/Pt(3)]_9$. (a) AFM image with its (b) MFM counterpart. (c) Second MFM scan over the same position. Scale bar: 4µm.

D. X-ray reflectometry

To access interface and surface quality of the investigated sample $Si//Ta(5)/Ir(5)/Fe(0.3)/Gd_xFeCo_{1-x}(8)/Pt(1.5)$, XRR measurement has been performed. The data is shown in figure D.1a. The large range of oscillations up to 10 degrees is an indicator of the presence of smooth interfaces. To quantitatively investigate the interface quality, a X-ray reflectivity fitting software, namely GenX, has been used [115]. The layer thicknesses, received from the fit, are in good agreement with the expected values from the sputter rates as seen in figure D.1b. Interface roughness is at most 10 percent of the corresponding layer thickness, with the exclusion of the top Pt layer, which has been milled, and therefore displays a roughness of similar magnitude as the layer thickness which is in agreement with AFM measurements (see Appendix C).

(a)

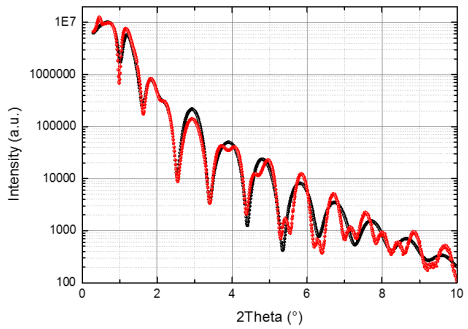

(b)

Layer	Real deposition (nm)	GenX fit (nm)	Roughness (nm)
Ta	5.0	5.4	0.5
Ir	5.0	5.0	0.2
Fe	0.3	0.5	0.1
GdFeCo	8.0	8.0	0.8
Pt	1.5	0.5	0.4

Figure D.1.: (a) X-ray reflectivity as a function of the 2Θ angle on $Si//Ta(5)/Ir(5)/Fe(0.3)/Gd_xFeCo_{1-x}(8)/Pt(1.5)$ after milling (red) and its fitting curve using GenX (black). (b) Comparison between the real deposition and the fitting of each layer using GenX.

E. Pattern design for current-induced dynamics of spin textures

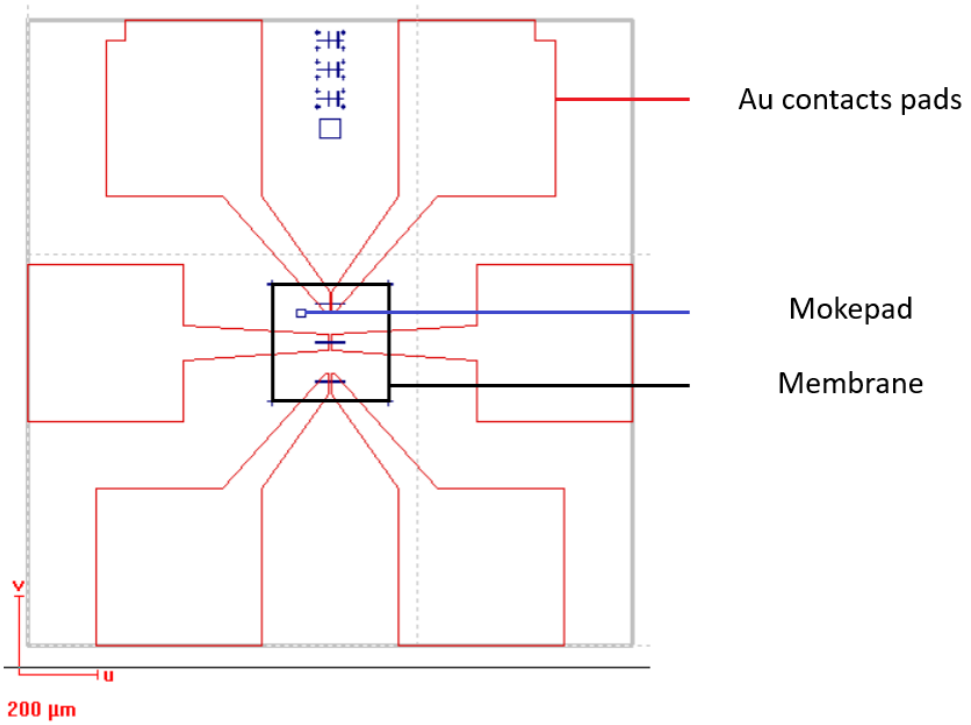

Figure E.1.: Design used on membranes for current-induced dynamics of magnetic spin textures. Au pads are deposited on top of the wire using EBL.

To deposit the multilayer stacks, one has used a process involving a positive resist as explained in Appendix B in order to limitate backing processes that have influences on the magnetic configurations especially in ferrimagnetic materials (see Appendix A). In figure E.1, one can see the membrane surrounded by the black line. Here, three wires have been patterned with different sizes in order to change the resistance of the wire. Indeed, in RF circuit, a resistance closed to 50 Ω is necessary to avoid signal reflections due to impedance mismatch. Since the resistance of the wire is in inverse proportion to the width of the wire, changing the width of the wire can help to be closer to the desired wire resistance. To give an order of magnetude of theses sizes, there were chosen to be 3, 5 and 10 µm or 5, 10 and

20 µm depending on the multilayer stack thickness and the nature of the material itself.

On the membrane, a large square pad of side 20 µm have been designed to check the material growth and their magnetic configurations with the help of Kerr microscopy and AFM/MFM. After patterning the wires, two Au pads of side 200 µm have been patterned in a second EBL step at each extremity of the wire, on top of them. These Au contacts are generally 5 µm away from each other to keep the resistance of the wire closed to 50 Ω since the wire resistance is directly proportional to the distance between the gold contacts. Since Au does not attach well to Si-based substrate, a sub-layer of Cr has been introduced to facilitate this adhesion. Therefore, the contacts are made as following: $Si/Si_3N_4//Cr(5nm)/Au(30nm)$. After deposition of the contacts, wires are electrically attached to a board using Al wire bonding. Here, one has prefered wedge bonding over ball bonding to get a small attached area.

Bibliography

[1] D.-H. Kim, M. Haruta, H.-W. Ko, G. Go, H.-J. Park, T. Nishimura, D.-Y. Kim, T. Okuno, Y. Hirata, Y. Futakawa, H. Yoshikawa, W. Ham, S. Kim, H. Kurata, A. Tsukamoto, Y. Shiota, T. Moriyama, S.-B. Choe, K.-J. Lee, and T. Ono, "Bulk dzyaloshinskii–moriya interaction in amorphous ferrimagnetic alloys," *Nature Materials*, vol. 18, pp. 685–690, Jul 2019.

[2] L. Caretta, E. Rosenberg, F. Büttner, T. Fakhrul, P. Gargiani, M. Valvidares, Z. Chen, P. Reddy, D. A. Muller, C. A. Ross, and G. S. D. Beach, "Interfacial dzyaloshinskii-moriya interaction arising from rare-earth orbital magnetism in insulating magnetic oxides," *Nature Communications*, vol. 11, p. 1090, Feb 2020.

[3] Z. Ye, Z. Chen, Z. Chen, W. Jia, T. Gao, L. Liu, H. Zheng, Q. Zeng, Q. Wang, N. Wang, B. Xiang, T. Lin, M. Qiu, S. Li, J. Shi, Z. Hou, K. Ando, and H. An, "Spin-orbit torque and interfacial dzyaloshinskii–moriya interaction in heavy metal/ferrimagnetic insulator deposited by magnetron sputtering," *Advanced Electronic Materials*, vol. 8, no. 1, p. 2100590, 2022.

[4] K.-W. Kim, K.-W. Moon, N. Kerber, J. Nothhelfer, and K. Everschor-Sitte, "Asymmetric skyrmion hall effect in systems with a hybrid dzyaloshinskii-moriya interaction," *Phys. Rev. B*, vol. 97, p. 224427, Jun 2018.

[5] A. Belabbes, G. Bihlmayer, F. Bechstedt, S. Blügel, and A. Manchon, "Hund's rule-driven dzyaloshinskii-moriya interaction at $3d{-}5d$ interfaces," *Phys. Rev. Lett.*, vol. 117, p. 247202, Dec 2016.

[6] G. Chen, A. T. N'Diaye, S. P. Kang, H. Y. Kwon, C. Won, Y. Wu, Z. Q. Qiu, and A. K. Schmid, "Unlocking bloch-type chirality in ultrathin magnets through uniaxial strain," *Nature Communications*, vol. 6, p. 6598, Mar 2015.

[7] A. Hubert and R. Schäfer, *Domain Theory*, pp. 99–335.
Berlin, Heidelberg: Springer Berlin Heidelberg, 1998.

[8] B. Lilley, "Lxxi. energies and widths of domain boundaries in ferromagnetics," *The London, Edinburgh, and Dublin Philosophical Magazine and Journal of Science*, vol. 41, no. 319, pp. 792–813, 1950.

[9] I. Lemesh, F. Büttner, and G. S. D. Beach, "Accurate model of the stripe domain phase of perpendicularly magnetized multilayers," *Phys. Rev. B*, vol. 95, p. 174423, May 2017.

[10] N. Nagaosa and Y. Tokura, "Topological properties and dynamics of magnetic skyrmions," *Nature Nanotechnology*, vol. 8, pp. 899–911, Dec 2013.

[11] J. H. Han, pp. 1–177.
Springer Cham, 2017.

[12] B. Göbel, I. Mertig, and O. A. Tretiakov, "Beyond skyrmions: Review and perspectives of alternative magnetic quasiparticles," *Physics Reports*, vol. 895, pp. 1–28, 2021.
Beyond skyrmions: Review and perspectives of alternative magnetic quasiparticles.

[13] "18 - on the theory of the dispersion of magnetic permeability in ferromagnetic bodies," in *Collected Papers of L.D. Landau* (D. TER HAAR, ed.), pp. 101–114, Pergamon, 1965.

[14] T. L. Gilbert, "A lagrangian formulation of the gyromagnetic equation of the magnetization field," *Physical Review D*, vol. 100, p. 1243, 1955.

[15] J. Slonczewski, "Current-driven excitation of magnetic multilayers," *Journal of Magnetism and Magnetic Materials*, vol. 159, no. 1, pp. L1–L7, 1996.

[16] L. Berger, "Prediction of a domain-drag effect in uniaxial, non-compensated, ferromagnetic metals," *Journal of Physics and Chemistry of Solids*, vol. 35, no. 8, pp. 947–956, 1974.

[17] M. Kläui, C. A. F. Vaz, J. A. C. Bland, W. Wernsdorfer, G. Faini, E. Cambril, and L. J. Heyderman, "Domain wall motion induced by spin polarized currents in ferromagnetic ring structures," *Applied Physics Letters*, vol. 83, no. 1, pp. 105–107, 2003.

[18] S. Zhang and Z. Li, "Roles of nonequilibrium conduction electrons on the magnetization dynamics of ferromagnets," *Phys. Rev. Lett.*, vol. 93, p. 127204, Sep 2004.

[19] F. Piéchon and A. Thiaville, "Spin transfer torque in continuous textures: Semiclassical boltzmann approach," *Phys. Rev. B*, vol. 75, p. 174414, May 2007.

[20] Q. Shao, P. Li, L. Liu, H. Yang, S. Fukami, A. Razavi, H. Wu, K. Wang, F. Freimuth, Y. Mokrousov, M. D. Stiles, S. Emori, A. Hoffmann, J. Åkerman, K. Roy, J.-P. Wang, S.-H. Yang, K. Garello, and W. Zhang, "Roadmap of spin–orbit torques," *IEEE Transactions on Magnetics*, vol. 57, no. 7, pp. 1–39, 2021.

[21] A. Manchon, J. Železný, I. M. Miron, T. Jungwirth, J. Sinova, A. Thiaville, K. Garello, and P. Gambardella, "Current-induced spin-orbit torques in ferromagnetic and antiferromagnetic systems," *Rev. Mod. Phys.*, vol. 91, p. 035004, Sep 2019.

[22] C. Song, R. Zhang, L. Liao, Y. Zhou, X. Zhou, R. Chen, Y. You, X. Chen, and F. Pan, "Spin-orbit torques: Materials, mechanisms, performances, and potential applications," *Progress in Materials Science*, vol. 118, p. 100761, 2021.

[23] A. Neubauer, C. Pfleiderer, B. Binz, A. Rosch, R. Ritz, P. G. Niklowitz, and P. Böni, "Topological hall effect in the *a* phase of mnsi," *Phys. Rev. Lett.*, vol. 102, p. 186602, May 2009.

[24] W. Jiang, X. Zhang, G. Yu, W. Zhang, X. Wang, M. Benjamin Jungfleisch, J. E. Pearson, X. Cheng, O. Heinonen, K. L. Wang, Y. Zhou, A. Hoffmann, and S. G. E. te Velthuis, "Direct observation of the skyrmion hall effect," *Nature Physics*, vol. 13, pp. 162–169, Feb 2017.

[25] K. Litzius, I. Lemesh, B. Krüger, P. Bassirian, L. Caretta, K. Richter, F. Büttner, K. Sato, O. A. Tretiakov, J. Förster, R. M. Reeve, M. Weigand, I. Bykova, H. Stoll, G. Schütz, G. S. D. Beach, and M. Kläui, "Skyrmion hall effect revealed by direct time-resolved x-ray microscopy," *Nature Physics*, vol. 13, pp. 170–175, Feb 2017.

[26] M. Baumgartner, K. Garello, J. Mendil, C. O. Avci, E. Grimaldi, C. Murer, J. Feng, M. Gabureac, C. Stamm, Y. Acremann, S. Finizio, S. Wintz, J. Raabe, and P. Gambardella, "Spatially and time-resolved magnetization dynamics driven by spin–orbit torques," *Nature Nanotechnology*, vol. 12, pp. 980–986, Oct 2017.

[27] K.-J. Kim, S. K. Kim, Y. Hirata, S.-H. Oh, T. Tono, D.-H. Kim, T. Okuno, W. S. Ham, S. Kim, G. Go, Y. Tserkovnyak, A. Tsukamoto, T. Moriyama, K.-J. Lee, and T. Ono, "Fast domain wall motion in the vicinity of the angular momentum compensation temperature of ferrimagnets," *Nat Mater*, vol. 16, pp. 1187–1192, Sept. 2017.

[28] F. limited. https://farotex.com/technology.html.

[29] J. Clarke, "SQUIDs," *Scientific American*, vol. 271, pp. 46–53, Aug. 1994.

[30] R. C. Jaklevic, J. Lambe, A. H. Silver, and J. E. Mercereau, "Quantum interference effects in josephson tunneling," *Phys. Rev. Lett.*, vol. 12, pp. 159–160, Feb 1964.

[31] P. W. Anderson and J. M. Rowell, "Probable observation of the josephson superconducting tunneling effect," *Phys. Rev. Lett.*, vol. 10, pp. 230–232, Mar 1963.

[32] H. R. Hulme, "The faraday effect in ferromagnetics," *Proc. R. Soc. Lond. A*, vol. 135, pp. 237–257, Feb 1932.

[33] P. N. Argyres, "Theory of the faraday and kerr effects in ferromagnetics," *Phys. Rev.*, vol. 97, pp. 334–345, Jan 1955.

[34] K. Sato and Y. Togami, "Magneto-optical spectra of rf-sputtered amorphous gd-co and gd-fe films," *Journal of Magnetism and Magnetic Materials*, vol. 35, no. 1, pp. 181–182, 1983.

[35] I. V. Soldatov and R. Schäfer, "Selective sensitivity in kerr microscopy," *Review of Scientific Instruments*, vol. 88, no. 7, p. 073701, 2017.

[36] L. Abelmann, A. van den Bos, and C. Lodder, *Magnetic Force Microscopy — Towards Higher Resolution*, pp. 253–283.
Berlin, Heidelberg: Springer Berlin Heidelberg, 2005.

[37] D. Rugar, H. J. Mamin, P. Guethner, S. E. Lambert, J. E. Stern, I. McFadyen, and T. Yogi, "Magnetic force microscopy: General principles and application to longitudinal recording media," *Journal of Applied Physics*, vol. 68, no. 3, pp. 1169–1183, 1990.

[38] U. Hartmann, "Magnetic force microscopy," *Annual Review of Materials Science*, vol. 29, no. 1, pp. 53–87, 1999.

[39] H. P. Oepen and R. Frömter, *Scanning Electron Microscopy with Polarisation Analysis*.
John Wiley & Sons, Ltd, 2007.

[40] K. Koike and K. Hayakawa, "Scanning electron microscope observation of magnetic domains using spin-polarized secondary electrons," *Japanese Journal of Applied Physics*, vol. 23, pp. L187–L188, mar 1984.

[41] T. H. DiStefano, "Technology for detecting small magnetic domains and beam-addressed memory therewith," *IBM Tech. Disc. Bull.*, vol. 20, pp. 4212–4215, 1978.

[42] J. Unguris, D. T. Pierce, A. Galejs, and R. J. Celotta, "Spin and energy analyzed secondary electron emission from a ferromagnet," *Phys. Rev. Lett.*, vol. 49, pp. 72–76, Jul 1982.

[43] M. R. Scheinfein, J. Unguris, M. H. Kelley, D. T. Pierce, and R. J. Celotta, "Scanning electron microscopy with polarization analysis (sempa)," *Review of Scientific Instruments*, vol. 61, no. 10, pp. 2501–2527, 1990.

[44] K. Koike, "Spin-polarized scanning electron microscopy," *Microscopy*, vol. 62, pp. 177–191, 01 2013.

[45] P. Krautscheid, R. M. Reeve, M. Lauf, B. Krüger, and M. Kläui, "Domain wall spin structures in mesoscopic fe rings probed by high resolution SEMPA," *Journal of Physics D: Applied Physics*, vol. 49, p. 425004, sep 2016.

[46] E. C. Corredor, S. Kuhrau, F. Kloodt-Twesten, R. Frömter, and H. P. Oepen, "Sempa investigation of the dzyaloshinskii-moriya interaction in the single, ideally grown co/pt(111) interface," *Phys. Rev. B*, vol. 96, p. 060410, Aug 2017.

[47] F. Kloodt-Twesten, S. Kuhrau, H. P. Oepen, and R. Frömter, "Measuring the dzyaloshinskii-moriya interaction of the epitaxial co/ir(111) interface," *Phys. Rev. B*, vol. 100, p. 100402, Sep 2019.

[48] D. Schönke, A. Oelsner, P. Krautscheid, R. M. Reeve, and M. Kläui, "Development of a scanning electron microscopy with polarization analysis system for magnetic imaging with ns time resolution and phase-sensitive detection," *Review of Scientific Instruments*, vol. 89, no. 8, p. 083703, 2018.

[49] M. Weigand, *Realization of a new Magnetic Scanning X-ray Microscope and Investigation of Landau Structures under Pulsed Field Excitation.* Cuvillier Verlag, 2015.

[50] U. Flechsig, C. Quitmann, J. Raabe, M. Böge, R. Fink, and H. Ade, "The pollux microspectroscopy beam line at the swiss light source," *AIP Conference Proceedings*, vol. 879, no. 1, pp. 505–508, 2007.

[51] J. L. Erskine and E. A. Stern, "Calculation of the M_{23} magneto-optical absorption spectrum of ferromagnetic nickel," *Phys. Rev. B*, vol. 12, pp. 5016–5024, Dec 1975.

[52] G. Schütz, W. Wagner, W. Wilhelm, P. Kienle, R. Zeller, R. Frahm, and G. Materlik, "Absorption of circularly polarized x rays in iron," *Phys. Rev. Lett.*, vol. 58, pp. 737–740, Feb 1987.

[53] A. Bogdanov and A. Hubert, "Thermodynamically stable magnetic vortex states in magnetic crystals," *Journal of Magnetism and Magnetic Materials*, vol. 138, no. 3, pp. 255–269, 1994.

[54] T. H. R. Skyrme and B. F. J. Schonland, "A non-linear field theory," *Proceedings of the Royal Society of London. Series A. Mathematical and Physical Sciences*, vol. 260, no. 1300, pp. 127–138, 1961.

[55] T. Skyrme, "A unified field theory of mesons and baryons," *Nuclear Physics*, vol. 31, pp. 556–569, 1962.

[56] S. Mühlbauer, B. Binz, F. Jonietz, C. Pfleiderer, A. Rosch, A. Neubauer, R. Georgii, and P. Böni, "Skyrmion lattice in a chiral magnet," *Science*, vol. 323, no. 5916, pp. 915–919, 2009.

[57] X. Z. Yu, Y. Onose, N. Kanazawa, J. H. Park, J. H. Han, Y. Matsui, N. Nagaosa, and Y. Tokura, "Real-space observation of a two-dimensional skyrmion crystal," *Nature*, vol. 465, pp. 901–904, Jun 2010.

[58] S. Seki, X. Z. Yu, S. Ishiwata, and Y. Tokura, "Observation of skyrmions in a multiferroic material," *Science*, vol. 336, no. 6078, pp. 198–201, 2012.

[59] I. V. Soldatov, W. Jiang, S. G. E. te Velthuis, A. Hoffmann, and R. Schäfer, "Size analysis of sub-resolution objects by kerr microscopy," *Applied Physics Letters*, vol. 112, no. 26, p. 262404, 2018.

[60] J. Zázvorka, F. Jakobs, D. Heinze, N. Keil, S. Kromin, S. Jaiswal, K. Litzius, G. Jakob, P. Virnau, D. Pinna, K. Everschor-Sitte, L. Rózsa, A. Donges, U. Nowak, and M. Kläui, "Thermal skyrmion diffusion used in a reshuffler device," *Nature Nanotechnology*, vol. 14, pp. 658–661, Jul 2019.

[61] W. Münzer, A. Neubauer, T. Adams, S. Mühlbauer, C. Franz, F. Jonietz, R. Georgii, P. Böni, B. Pedersen, M. Schmidt, A. Rosch, and C. Pfleiderer, "Skyrmion lattice in the doped semiconductor $\mathrm{fe}_{1-x}\mathrm{co}_x\mathrm{Si}$," *Phys. Rev. B*, vol. 81, p. 041203, Jan 2010.

[62] S. Heinze, K. von Bergmann, M. Menzel, J. Brede, A. Kubetzka, R. Wiesendanger, G. Bihlmayer, and S. Blügel, "Spontaneous atomic-scale magnetic skyrmion lattice in two dimensions," *Nature Physics*, vol. 7, pp. 713–718, Sep 2011.

[63] T. Schulz, R. Ritz, A. Bauer, M. Halder, M. Wagner, C. Franz, C. Pfleiderer, K. Everschor, M. Garst, and A. Rosch, "Emergent electrodynamics of skyrmions in a chiral magnet," *Nature Physics*, vol. 8, pp. 301–304, Apr 2012.

[64] S. Woo, K. Litzius, B. Krüger, M.-Y. Im, L. Caretta, K. Richter, M. Mann, A. Krone, R. M. Reeve, M. Weigand, P. Agrawal, I. Lemesh, M.-A. Mawass, P. Fischer, M. Kläui, and G. S. D. Beach, "Observation of room-temperature magnetic skyrmions and their current-driven dynamics in ultrathin metallic ferromagnets," *Nature Materials*, vol. 15, pp. 501–506, May 2016.

[65] Q. Shao, Y. Liu, G. Yu, S. K. Kim, X. Che, C. Tang, Q. L. He, Y. Tserkovnyak, J. Shi, and K. L. Wang, "Topological hall effect at above room temperature in heterostructures composed of a magnetic insulator and a heavy metal," *Nature Electronics*, vol. 2, pp. 182–186, May 2019.

[66] J. Torrejon, J. Kim, J. Sinha, S. Mitani, M. Hayashi, M. Yamanouchi, and H. Ohno, "Interface control of the magnetic chirality in cofeb/mgo heterostructures with heavy-metal underlayers," *Nature Communications*, vol. 5, p. 4655, Aug 2014.

[67] R. Lo Conte, E. Martinez, A. Hrabec, A. Lamperti, T. Schulz, L. Nasi, L. Lazzarini, R. Mantovan, F. Maccherozzi, S. S. Dhesi, B. Ocker, C. H. Marrows, T. A. Moore, and M. Kläui, "Role of b diffusion in the interfacial dzyaloshinskii-moriya interaction in Ta/$co_{20}Fe_{60}b_{20}$/MgO nanowires," *Phys. Rev. B*, vol. 91, p. 014433, Jan 2015.

[68] J. Sampaio, V. Cros, S. Rohart, A. Thiaville, and A. Fert, "Nucleation, stability and current-induced motion of isolated magnetic skyrmions in nanostructures," *Nature Nanotechnology*, vol. 8, pp. 839–844, Nov 2013.

[69] S. Woo, K. M. Song, X. Zhang, Y. Zhou, M. Ezawa, X. Liu, S. Finizio, J. Raabe, N. J. Lee, S.-I. Kim, S.-Y. Park, Y. Kim, J.-Y. Kim, D. Lee, O. Lee, J. W. Choi, B.-C. Min, H. C. Koo, and J. Chang, "Current-driven dynamics and inhibition of the skyrmion hall effect of ferrimagnetic skyrmions in gdfeco films," *Nature Communications*, vol. 9, p. 959, Mar 2018.

[70] A. G. Kolesnikov, M. E. Stebliy, A. S. Samardak, and A. V. Ognev, "Skyrmionium – high velocity without the skyrmion hall effect," *Scientific Reports*, vol. 8, p. 16966, Nov 2018.

[71] Y. Hirata, D.-H. Kim, S. K. Kim, D.-K. Lee, S.-H. Oh, D.-Y. Kim, T. Nishimura, T. Okuno, Y. Futakawa, H. Yoshikawa, A. Tsukamoto, Y. Tserkovnyak, Y. Shiota, T. Moriyama, S.-B. Choe, K.-J. Lee, and T. Ono, "Vanishing

skyrmion hall effect at the angular momentum compensation temperature of a ferrimagnet," *Nature Nanotechnology*, vol. 14, pp. 232–236, Mar 2019.

[72] X. Liang, X. Zhang, L. Shen, J. Xia, M. Ezawa, X. Liu, and Y. Zhou, "Dynamics of ferrimagnetic skyrmionium driven by spin-orbit torque," *Phys. Rev. B*, vol. 104, p. 174421, Nov 2021.

[73] B. Seng, D. Schönke, J. Yeste, R. M. Reeve, N. Kerber, D. Lacour, J.-L. Bello, N. Bergeard, F. Kammerbauer, M. Bhukta, T. Ferté, C. Boeglin, F. Radu, R. Abrudan, T. Kachel, S. Mangin, M. Hehn, and M. Kläui, "Direct imaging of chiral domain walls and néel-type skyrmionium in ferrimagnetic alloys," *Advanced Functional Materials*, vol. 31, no. 33, p. 2102307, 2021.

[74] J. Iwasaki, M. Mochizuki, and N. Nagaosa, "Current-induced skyrmion dynamics in constricted geometries," *Nature Nanotechnology*, vol. 8, pp. 742–747, Oct 2013.

[75] B. Göbel, A. F. Schäffer, J. Berakdar, I. Mertig, and S. S. P. Parkin, "Electrical writing, deleting, reading, and moving of magnetic skyrmioniums in a racetrack device," *Scientific Reports*, vol. 9, p. 12119, Aug 2019.

[76] S. Zhang, J. Zhang, Q. Zhang, C. Barton, V. Neu, Y. Zhao, Z. Hou, Y. Wen, C. Gong, O. Kazakova, W. Wang, Y. Peng, D. A. Garanin, E. M. Chudnovsky, and X. Zhang, "Direct writing of room temperature and zero field skyrmion lattices by a scanning local magnetic field," *Applied Physics Letters*, vol. 112, no. 13, p. 132405, 2018.

[77] A. Casiraghi, H. Corte-León, M. Vafaee, F. Garcia-Sanchez, G. Durin, M. Pasquale, G. Jakob, M. Kläui, and O. Kazakova, "Individual skyrmion manipulation by local magnetic field gradients," *Communications Physics*, vol. 2, p. 145, Nov 2019.

[78] G. Berruto, I. Madan, Y. Murooka, G. M. Vanacore, E. Pomarico, J. Rajeswari, R. Lamb, P. Huang, A. J. Kruchkov, Y. Togawa, T. LaGrange, D. McGrouther, H. M. Rønnow, and F. Carbone, "Laser-induced skyrmion writing and erasing in an ultrafast cryo-lorentz transmission electron microscope," *Phys. Rev. Lett.*, vol. 120, p. 117201, Mar 2018.

[79] S.-G. Je, P. Vallobra, T. Srivastava, J.-C. Rojas-Sánchez, T. H. Pham, M. Hehn, G. Malinowski, C. Baraduc, S. Auffret, G. Gaudin, S. Mangin, H. Béa, and O. Boulle, "Creation of magnetic skyrmion bubble lattices by ultrafast laser in ultrathin films," *Nano Letters*, vol. 18, pp. 7362–7371, Nov 2018.

[80] N. Romming, C. Hanneken, M. Menzel, J. E. Bickel, B. Wolter, K. von Bergmann, A. Kubetzka, and R. Wiesendanger, "Writing and deleting single magnetic skyrmions," *Science*, vol. 341, no. 6146, pp. 636–639, 2013.

[81] Y. Liu, G. Yin, J. Zang, J. Shi, and R. K. Lake, "Skyrmion creation and annihilation by spin waves," *Applied Physics Letters*, vol. 107, no. 15, p. 152411, 2015.

[82] P.-J. Hsu, A. Kubetzka, A. Finco, N. Romming, K. von Bergmann, and R. Wiesendanger, "Electric-field-driven switching of individual magnetic skyrmions," *Nature Nanotechnology*, vol. 12, pp. 123–126, Feb 2017.

[83] C. Hanneken, F. Otte, A. Kubetzka, B. Dupé, N. Romming, K. von Bergmann, R. Wiesendanger, and S. Heinze, "Electrical detection of magnetic skyrmions by tunnelling non-collinear magnetoresistance," *Nature Nanotechnology*, vol. 10, pp. 1039–1042, Dec 2015.

[84] S. S. P. Parkin, M. Hayashi, and L. Thomas, "Magnetic domain-wall racetrack memory," *Science*, vol. 320, no. 5873, pp. 190–194, 2008.

[85] R. Tomasello, E. Martinez, R. Zivieri, L. Torres, M. Carpentieri, and G. Finocchio, "A strategy for the design of skyrmion racetrack memories," *Scientific Reports*, vol. 4, p. 6784, Oct 2014.

[86] W. Kang, X. Chen, D. Zhu, X. Zhang, Y. Zhou, K. Qiu, Y. Zhang, and W. Zhao, "A comparative study on racetrack memories: Domain wall vs. skyrmion," in *2018 IEEE 7th Non-Volatile Memory Systems and Applications Symposium (NVMSA)*, pp. 7–12, 2018.

[87] S. Wang, J. Tang, W. Wang, L. Kong, M. Tian, and H. Du, "Electrical detection of magnetic skyrmions," *Journal of Low Temperature Physics*, vol. 197, pp. 321–336, Nov 2019.

[88] X. Zhang, G. P. Zhao, H. Fangohr, J. P. Liu, W. X. Xia, J. Xia, and F. J. Morvan, "Skyrmion-skyrmion and skyrmion-edge repulsions in skyrmion-based racetrack memory," *Scientific Reports*, vol. 5, p. 7643, Jan 2015.

[89] D. Capic, D. A. Garanin, and E. M. Chudnovsky, "Skyrmion–skyrmion interaction in a magnetic film," *Journal of Physics: Condensed Matter*, vol. 32, p. 415803, jul 2020.

[90] M. Hoffmann, G. P. Müller, C. Melcher, and S. Blügel, "Skyrmion-antiskyrmion racetrack memory in rank-one dmi materials," *Frontiers in Physics*, vol. 9, 2021.

[91] X. Zhang, M. Ezawa, and Y. Zhou, "Magnetic skyrmion logic gates: conversion, duplication and merging of skyrmions," *Scientific Reports*, vol. 5, p. 9400, Mar 2015.

[92] M. Carpentieri, R. Tomasello, R. Zivieri, and G. Finocchio, "Topological, non-topological and instanton droplets driven by spin-transfer torque in materials with perpendicular magnetic anisotropy and dzyaloshinskii–moriya interaction," *Scientific Reports*, vol. 5, p. 16184, Nov 2015.

[93] A. Fert, N. Reyren, and V. Cros, "Magnetic skyrmions: advances in physics and potential applications," *Nature Reviews Materials*, vol. 2, p. 17031, Jun 2017.

[94] F. Ma, Y. Zhou, H. B. Braun, and W. S. Lew, "Skyrmion-based dynamic magnonic crystal," *Nano Letters*, vol. 15, no. 6, pp. 4029–4036, 2015.

PMID: 25989181.

[95] W. Jiang, P. Upadhyaya, W. Zhang, G. Yu, M. B. Jungfleisch, F. Y. Fradin, J. E. Pearson, Y. Tserkovnyak, K. L. Wang, O. Heinonen, S. G. E. te Velthuis, and A. Hoffmann, "Blowing magnetic skyrmion bubbles," *Science*, vol. 349, no. 6245, pp. 283–286, 2015.

[96] C. Moreau-Luchaire, C. Moutafis, N. Reyren, J. Sampaio, C. A. F. Vaz, N. Van Horne, K. Bouzehouane, K. Garcia, C. Deranlot, P. Warnicke, P. Wohlhüter, J.-M. George, M. Weigand, J. Raabe, V. Cros, and A. Fert, "Additive interfacial chiral interaction in multilayers for stabilization of small individual skyrmions at room temperature," *Nature Nanotechnology*, vol. 11, pp. 444–448, May 2016.

[97] H. Yang, A. Thiaville, S. Rohart, A. Fert, and M. Chshiev, "Anatomy of dzyaloshinskii-moriya interaction at Co/Pt interfaces," *Phys. Rev. Lett.*, vol. 115, p. 267210, Dec 2015.

[98] R. Lavrijsen, D. M. F. Hartmann, A. van den Brink, Y. Yin, B. Barcones, R. A. Duine, M. A. Verheijen, H. J. M. Swagten, and B. Koopmans, "Asymmetric magnetic bubble expansion under in-plane field in pt/co/pt: Effect of interface engineering," *Phys. Rev. B*, vol. 91, p. 104414, Mar 2015.

[99] M. Belmeguenai, J.-P. Adam, Y. Roussigné, S. Eimer, T. Devolder, J.-V. Kim, S. M. Cherif, A. Stashkevich, and A. Thiaville, "Interfacial dzyaloshinskii-moriya interaction in perpendicularly magnetized pt/co/alo$_x$ ultrathin films measured by brillouin light spectroscopy," *Phys. Rev. B*, vol. 91, p. 180405, May 2015.

[100] J. Cho, N.-H. Kim, S. Lee, J.-S. Kim, R. Lavrijsen, A. Solignac, Y. Yin, D.-S. Han, N. J. J. van Hoof, H. J. M. Swagten, B. Koopmans, and C.-Y. You, "Thickness dependence of the interfacial dzyaloshinskii–moriya interaction in inversion symmetry broken systems," *Nature Communications*, vol. 6, p. 7635, Jul 2015.

[101] K. Di, V. L. Zhang, H. S. Lim, S. C. Ng, M. H. Kuok, J. Yu, J. Yoon, X. Qiu, and H. Yang, "Direct observation of the dzyaloshinskii-moriya interaction in a pt/co/ni film," *Phys. Rev. Lett.*, vol. 114, p. 047201, Jan 2015.

[102] U. Atxitia, D. Hinzke, O. Chubykalo-Fesenko, U. Nowak, H. Kachkachi, O. N. Mryasov, R. F. Evans, and R. W. Chantrell, "Multiscale modeling of magnetic materials: Temperature dependence of the exchange stiffness," *Phys. Rev. B*, vol. 82, p. 134440, Oct 2010.

[103] L. Rózsa, U. Atxitia, and U. Nowak, "Temperature scaling of the dzyaloshinsky-moriya interaction in the spin wave spectrum," *Phys. Rev. B*, vol. 96, p. 094436, Sep 2017.

[104] K. Tani and M. Takemura, "Frequency shift and damping constant of ferrimagnetic spin waves," *Physics Letters A*, vol. 26, no. 9, pp. 422–423, 1968.

[105] K.-H. Ko and G.-M. Choi, "Optical method of determining the spin diffusion length of ferromagnetic metals," *Journal of Magnetism and Magnetic Materials*, vol. 510, p. 166945, 2020.

[106] Y. Xu, M. Hehn, W. Zhao, X. Lin, G. Malinowski, and S. Mangin, "From single to multiple pulse all-optical switching in gdfeco thin films," *Phys. Rev. B*, vol. 100, p. 064424, Aug 2019.

[107] O. V. Borovkova, D. O. Ignatyeva, and V. I. Belotelov, "Layer-selective magnetization switching in the chirped photonic crystal with gdfeco," *Scientific Reports*, vol. 11, p. 2239, Jan 2021.

[108] L. Caretta, M. Mann, F. Büttner, K. Ueda, B. Pfau, C. M. Günther, P. Hessing, A. Churikova, C. Klose, M. Schneider, D. Engel, C. Marcus, D. Bono, K. Bagschik, S. Eisebitt, and G. S. D. Beach, "Fast current-driven domain walls and small skyrmions in a compensated ferrimagnet," *Nature Nanotechnology*, vol. 13, pp. 1154–1160, Dec 2018.

[109] M. Morota, Y. Niimi, K. Ohnishi, D. H. Wei, T. Tanaka, H. Kontani, T. Kimura, and Y. Otani, "Indication of intrinsic spin hall effect in $4d$ and $5d$ transition metals," *Phys. Rev. B*, vol. 83, p. 174405, May 2011.

[110] J. Sinova, S. O. Valenzuela, J. Wunderlich, C. H. Back, and T. Jungwirth, "Spin hall effects," *Rev. Mod. Phys.*, vol. 87, pp. 1213–1260, Oct 2015.

[111] S. Yakata, Y. Ando, T. Miyazaki, and S. Mizukami, "Temperature dependences of spin-diffusion lengths of cu and ru layers," *Japanese Journal of Applied Physics*, vol. 45, pp. 3892–3895, may 2006.

[112] K. Chen, D. Lott, A. Philippi-Kobs, M. Weigand, C. Luo, and F. Radu, "Observation of compact ferrimagnetic skyrmions in dyco3 film," *Nanoscale*, vol. 12, pp. 18137–18143, 2020.

[113] D. B. Allan, T. Caswell, N. C. Keim, and C. M. van der Wel, "trackpy: Trackpy v0.4.1," Apr 2018.

[114] C. Reichhardt and C. J. O. Reichhardt, "Noise fluctuations and drive dependence of the skyrmion hall effect in disordered systems," *New Journal of Physics*, vol. 18, p. 095005, sep 2016.

[115] M. Björck and G. Andersson, "*GenX*: an extensible X-ray reflectivity refinement program utilizing differential evolution," *Journal of Applied Crystallography*, vol. 40, pp. 1174–1178, Dec 2007.

List of Abbreviations

ABE	asymmetric bubble expension
AFM	atomic force microscopy
BLS	Brillouin light scattering
DMI	Dzyaloshinskii-Moriya interaction
DW	domain wall
EBL	electron beam lithography
FFT	fast Fourier transform
HM	heavy metal
IP	in-plane
LEED	low-energy electron diffraction
MAE	magnetic anisotropy energy
MFM	magnetic force microscopy
MOKE	magneto-optical Kerr effect
OSA	order sorting aperture
OOP	out-of-plane
PEM	photo-elastic modulator
PMA	perpendicular magnetic anisotropy
PVD	physical vapor deposition
RE	rare earth
RT	room temperature
SEMPA	scanning electron microscopy with polarization analysis
SHE	spin Hall effect
SOC	Spin-orbit coupling
SOT	spin-orbit torque
SQUID	superconducting quantum interference device
SRT	spin reorientation transition
STT	spin-transfer torque
STXM	scanning transmission X-ray microscopy
TM	transition metal
UHV	ultra high vacuum
XMCD	X-ray magnetic circular dichroism
XRR	X-ray reflectometry

List of Figures

List of Publications

- N. Kerber, D. Ksenzov, F. Freimuth, F. Capotondi, E. Pedersoli, I. Lopez-Quintas, B. Seng, J. Cramer, K. Litzius, D. Lacour, H. Zabel, Y. Mokrousov, M. Kläui and C. Gutt. Faster chiral versus collinear magnetic order recovery after optical excitation revealed by femtosecond XUV scattering. Nature Communications **11**, 6304 (2020).

- C. Song, N. Kerber, J. Rothörl, Y. Ge, K. Raab, B. Seng, M. A. Brems, F. Dittrich, R. M. Reeve, J. Wang, Q. Liu, P. Virnau and M. Kläui. Commensurability between Element Symmetry and the Number of Skyrmions Governing Skyrmion Diffusion in Confined Geometries. Advanced Functional Materials **31**, 2010739 (2021).

- B. Seng, D. Schönke, J. Yeste, R. M. Reeve, N. Kerber, D. Lacour, J.-L. Bello, N. Bergeard, F. Kammerbauer, M. Bhukta, T. Ferté, C. Boeglin, F. Radu, R. Abrudan, T. Kachel, S. Mangin, M. Hehn and M. Kläui. Direct Imaging of Chiral Domain Walls and Néel-Type Skyrmionium in Ferrimagnetic Alloys. Advanced Functional Materials **31**, 2102307 (2021).

- R. Gruber, J. Zázvorka, M. A. Brems, D. R. Rodrigues, T. Dohi, N. Kerber, B. Seng, M. Vafaee, K. Everschor-Sitte, P. Virnau and M. Kläui. Skyrmion pinning energetics in thin film systems. Nature Communications **13**, 3144 (2022).

- N. Zhou Hagström, M. Schneider, N. Kerber, A. Yaroslavtsev, E. Burgos Parra, M. Beg, M. Lang, C. M. Günther, B. Seng, F. Kammerbauer, H. Popescu, M. Pancaldi, K. Neeraj, D. Polley, R. Jangid, S. B. Hrkac, S. K. K. Patel, S. Ovcharenko, D. Turenne, D. Ksenzov, C. Boeglin, M. Baidakova, C. von Korff Schmising, M. Borchert, B. Vodungbo, K. Chen, C. Luo, F. Radu, L. Müller, M. Martínez Flórez, A. Philippi-Kobs, M. Riepp, W. Roseker, G. Grübel, R. Carley, J. Schlappa, B. E. Van Kuiken, R. Gort, L. Mercadier, N. Agarwal, L. Le Guyader, G. Mercurio, M. Teichmann, J. T. Delitz, A. Reich, C. Broers, D. Hickin, C. Deiter, J. Moore, D. Rompotis, J. Wang, D. Kane, S. Venkatesan, J. Meier, F. Pallas, T. Jezynski, M. Lederer, D. Boukhelef, J. Szuba, K. Wrona, S. Hauf, J. Zhu, M. Bergemann, E. Kamil, T. Kluyver, R. Rosca, M. Spirzewski, M. Kuster, M. Turcato, D. Lomidze, A. Samartsev, J. Engelke, M. Porro, S. Maffessanti, K. Hansen, F. Erdinger, P. Fischer, C. Fiorini, A. Castoldi, M. Manghisoni, C. B. Wunderer, E. E. Fullerton, O. G. Shpyrko, C. Gutt, C. Sanchez-Hanke, H. A. Dürr, E. Iacocca, H. T. Nembach, M. W. Keller, J. M. Shaw, T. J. Silva, R. Kukreja, H. Fangohr, S. Eisebitt, M. Kläui, N. Jaouen,

A. Scherz, S. Bonetti and E. Jal. Megahertz-rate ultrafast X-ray scattering and holographic imaging at the European XFEL. Journal of Synchrotron Radiation **29**, S1600577522008414 (2022).

Résumé étendu

En ces temps de préoccupations écologiques, l'impact de nos modes de vie sur notre environnement est essentiel à analyser. L'énergie étant la principale source d'émissions de gaz à effet de serre dans le monde, il est nécessaire de chercher des moyens pour réduire notre consommation.
Une des sources importantes de consommation d'énergie est le stockage des données, stockage augmentant chaque année de manière significative. Il a été proposé une nouvelle solution technologique permettant le stockage de ces données à moindre coût énergétique et de manières plus efficace en utilisant des skyrmions magnétiques en lieu et place des domaines magnétiques. Un skyrmion magnétique est une quasi-particule magnétique de taille pouvant être réduite à quelques atomes alors qu'un domaine magnétique est de l'ordre du micromètre. Il est donc possible d'imaginer un système de stockage de l'information reposant sur l'absence ou la présence de cette quasi-particule, représentant le "0" ou le "1" d'un bit de donnée. Ainsi, cette thèse se focalisera sur la nucléation et la manipulation de skyrmions magnétiques.

Ces quasi-particules ont tout d'abord été stabilisé dans des structures cristallines B20 et plus récemment dans divers matériaux à température ambiante, condition sine qua non à une utilisation par tous. Il a également été montré la possibilité de les nucléer, de les annihiler et même de les déplacer à l'aide de courants électriques. Néanmoins, le déplacement de ces structures magnétiques, à l'heure d'aujourd'hui, pose problème. Premièrement, ces structures semblent être particulièrement affectées par les défauts structurels de la matière, ce qu'on appelle le "pinning". En effet, les skyrmions magnétiques sont si petits qu'ils peuvent être piégés voir détruits au passage d'un défaut dans le matériau d'où ils proviennent. Deuxièmement, il est apparu que les skyrmions ne se déplaçaient pas de manières linéaires avec le courant appliqué mais possédaient une composante perpendiculaire les faisant dévier du chemin des électrons, effet connu sous le nom de "skyrmion Hall angle". Ceci peut être un problème dans la mesure où ils peuvent rencontrer la paroi d'une structure lithographiée provoquant la non-homogénéité de la dynamique et impliquer une possible perte de l'information stockée. Pour remédier au moins en partie à ces problèmes, l'utilisation d'un matériau ferrimagnétique a été proposé. Théoriquement, il est possible d'annihiler ce "skyrmion Hall angle" dans un matériau ferrimagnétique possédant une très faible aimantation à une température bien précise. Ainsi, les expériences menées dans cette thèse ont pour but de nucléer des skyrmions magnétiques dans des matériaux ferrimagnétiques tout en étudiant leur dynamique.

Dans cette thèse, il a tout d'abord été nécessaire de bien appréhender la problématique

des skyrmions. Pour ce faire, il a été important de décrire avec une certaine précision la théorie dans laquelle les skyrmions s'inscrivent, sans forcément être une revue complète du domaine mais permettant au lecteur de se situer dans le contexte. Ainsi, le chapitre 1 décrit les intéractions jouant un rôle majeur dans la formation de structures de spin et s'attarde sur la définition même de ces structures, leur limite voire leurs propriétés. En outre, il sera également question des effets théoriques des courants électriques sur les dites particules. Enfin, ce chapitre décrit également les propriétés de ces mêmes structures de spin mais dans les matériaux ferrimagnétiques, matériaux qui seront utilisés dans cette thèse.
Dans le chapitre 2, il a été décrit de manière succintes et non-exhaustives les différentes expériences qui ont été utilisés dans cette thèse pour l'étude des structures de spin. La déposition par pulvérisation cathodique a été décrite, technique prépondérante de cette thèse permettant l'obtention de films minces et homogènes. Pour pouvoir étudier la dynamique de skyrmions, la lithographie par faisceau d'électrons a été nécessaire et de ce fait est également décrite dans ce chapitre. Bien que ces deux techniques précédemment mentionnées ne représentent que quelques paragraphes, ils ont été particulièrement utilisé. Enfin, la plupart des techniques de magnétométrie ou d'imagerie utilisées pour la réalisation de cette thèse a été décrite dans cette fin de chapitre 2. Ici, il a été particulièrement décrit les techniques de "Microscopie électronique à balayage avec analyse de polarisation" et de "Microscopie à rayons X à balayage en transmission", techniques centrales d'où proviennent l'entièreté des résultats de cette thèse.
Le chapitre 3 se concentre sur l'état de l'art de ce que sont, au jour d'aujourd'hui, les différents avancements qui ont été trouvé dans la littérature sur les skyrmions magnétiques. Ainsi, il est retransmit dans ce manuscrit les premières découvertes que sont les stabilisations de skyrmions et en particulier à température ambiantes ainsi que leur observation dans les matériaux ferrimagnétiques. De plus, leur propriétés remarquables quand les skyrmions sont soumis à un courant électriques ont été relayé, que ce soit leur écriture, leur création et destruction ainsi que leur détection. Finalement, il a été listé les différents dispositifs technologiques pouvant être créés à l'aide de ces structures de spin.
Le chapitre 4 est le premier chapitre relatant les résultats obtenus durant cette thèse. Ici, il a été mis en évidence le caractère homochiral des structures de spin dans un matériau ferrimagnétique de type Ta/Ir/Fe/GdFeCo/Pt. Bien que ce matériau présentait un cycle "carré" hors du plan, la nucléation de structures de spin a été possible à l'aide de champs magnétiques dans le plan, forçant le système à se mettre dans un état métastable. Ces structures ont été cartographié à l'aide d'un microscope électronique à balayage avec analyse de polarisation où la configuration magnétique dans le plan a été révélé, indiquant le caractère homochiral des quasi-particules, de type purement Néel droite, sur toute la gamme de température étudiée soit de 26 K à 315 K. Ce type de chiralité donne une indication claire sur l'origine de l'intéraction la provoquant, soit une intéraction d'interface de type Dzyaloshinskii-Moriya. Également, la haute résolution de ce microscope autorise la mesure précise de la largeur des parois de domaines, région séparant deux domaines magnétiques

opposés en direction. Ainsi, à température ambiante, il a été mesuré des parois de domaines de 275 nm suivant la définition de Lilley, parois relativement large pouvant s'expliquer par une anisotropie réduite dans les matériaux ferrimagnétiques provenant d'une faible aimantation. Á l'aide de la nature de la chiralité (murs de domaines de type Néel droite) ainsi que de la mesure de la largeur des parois de domaines, il a pu être déduit la valeur de la constante d'échange, paramètre important dans la physique de la matière condensée mais souvent difficile à mesurer. Ainsi, pour ce matériau spécifique, une valeur de 8.0 pJ/m a été relevé. Cette mesure est en accord avec la littérature dans les matériaux ferrimagniques à base de GdFeCo. De manières plus étonnantes, il a été observé un skyrmionium ferrimagnétique dans ce matériau, structure de spin qui avait été prédit mais jamais observé directement. Celle-ci étant particulièrement intéressante de par la valeur de sa charge topologique, 0, permettant une annihilation de l'angle Hall des skyrmions.
Le chapitre 5 se focalise sur le deuxième résultat important de ce travail, soit la nucléation de skyrmions magnétiques dans un matériau ferrimagnétique à base de CoDy ainsi que de leur dynamique à l'aide de courant électriques. Ceci est particulièrement novateur puisqu'aucun skyrmion n'avait été mis à jour dans ce type de matériau dans des couches minces. Cette nucléation a été possible à l'aide de champs magnétiques et a même été révélé à l'aide du gradient de champ magnétique surgissant d'une pointe MFM à bas moment. Á l'aide d'un microscope à rayons X à balayage en transmission, technique d'imagerie en transmission à haute résolution, il a été possible d'observer les skyrmions magnétiques à différentes températures et à différents champs magnétiques. Dans cette expérience, les skyrmions sont inscrits sur une piste lithographiés de taille micrométriques et connectés électriquement à un circuit imprimé permettant l'application de pulses de courants. L'application de courant a révélé une dynamique déterministique des skyrmions avec un certain angle comparé à la direction du courant électriques, ce qui veut dire que les skyrmions se déplaçaient dans la même direction, révélant ainsi un angle de Hall du skyrmion. Cette angle a été mesuré pour différents courants mettant en évidence que l'angle de Hall du skyrmion commence aux alentours de 0 et finit à une valeur limite, ici entre 20° et 30°. Théoriquement, il a été montré que ce genre de caractères dynamique indiquerait la présence de site de défaut dans la matériau. De plus, cette étude s'est étendu sur la vitesse de ces skyrmions en fonction de la densité de courant injecté à différentes température où une certaine linéarité a été mis à jour. Ici, il s'agirait du deuxième type de matériau où ce genre de dynamique a été observé.